# Broadband, Volumetric Negative-Refractive-Index Media

by

Scott M. Rudolph

A dissertation submitted in partial fulfillment
of the requirements for the degree of
Doctor of Philosophy
(Electrical Engineering)
in The University of Michigan
2011

Doctoral Committee:

Associate Professor Anthony Grbic, Chair
Professor Eric Michielssen
Professor Kamal Sarabandi
Assistant Professor A. John Hart
Assistant Professor Mona Jarrahi
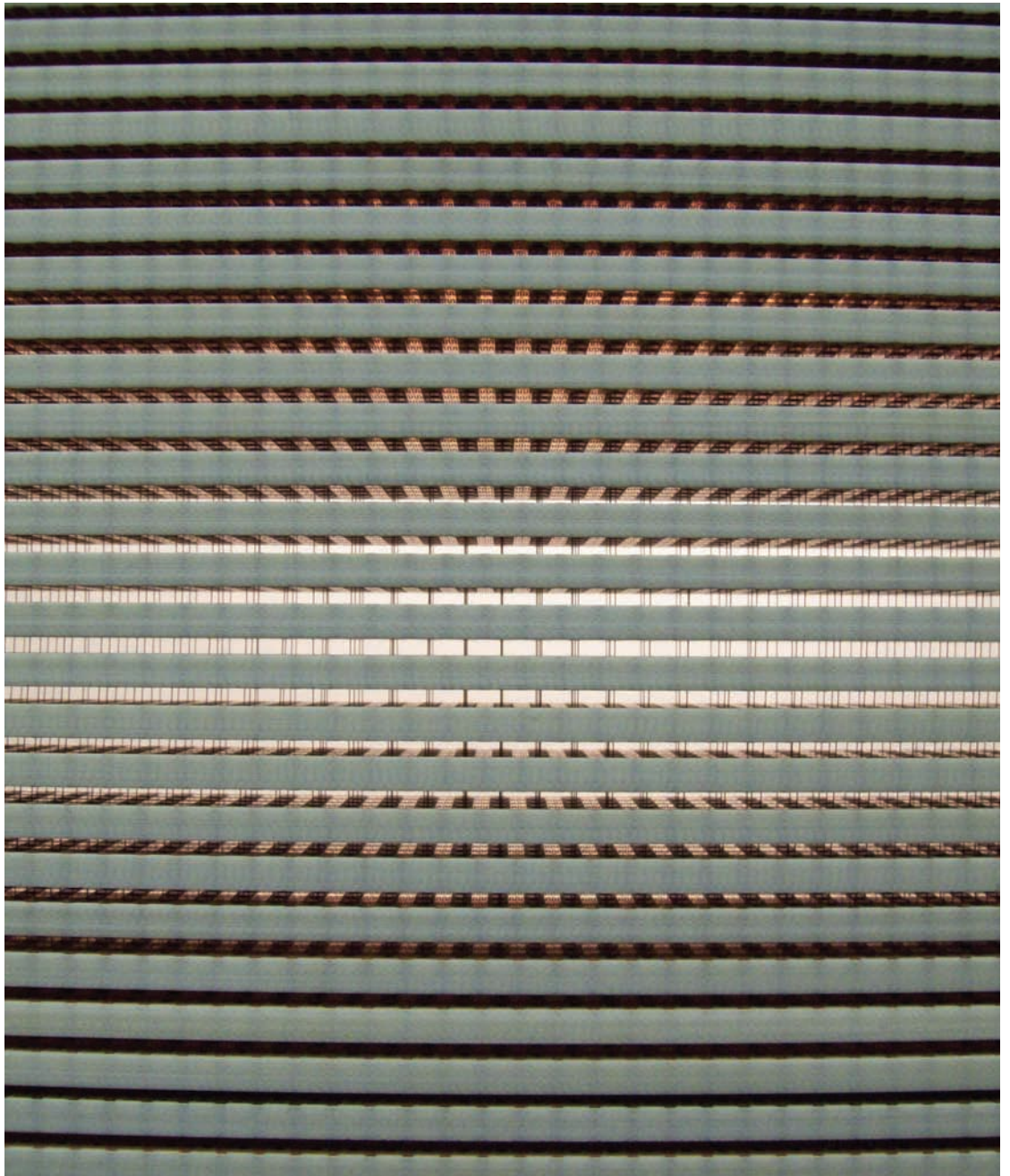
To my mother and father, who are responsible for the foundation on which my
education is built.

ACKNOWLEDGEMENTS

I am very grateful to my advisor, Tony. Your passion and good nature are a rare combination, for which I am extremely thankful. Your confidence in my ability encouraged me throughout these past five years, and your tireless effort provided me with every opportunity for success. The work that follows would not have been possible without your counsel and friendship.

I would like to thank my family for all their support. Mom, you taught me the dedication and responsibility that have served me well in all aspects of life. Dad, you inspired my enthusiasm for engineering with trips inside electrical generators and showed me the joy of working with my hands. More than this, you both have been a constant source of encouragement: celebrating my successes and lifting me up when I fell short. Kara, you gave me an example of academic success that set the tone for all my years at the University of Michigan. You also stick up for me in a way only big sisters can, and I am thankful for that.

To the past and present members of the Radlab and all the other friends I have made at the University of Michigan, I am grateful for your camaraderie. Whether it was ultimate in the diag, trips to the bar, late nights in the CAEN labs or simply discussions in the office, you made my time as a Ph.D. student genuinely enjoyable. I would like to specifically thank Carl Pfeiffer for his assistance with the measurements described in this thesis. It was a relief to know I could count on your work. I would also like to thank Mauro Ettore for his valuable editing.

Finally, I would like to thank my beautiful wife, Megan. Your dedication inspired

me to achieve greater things than I would have ever done on my own. The assurance of your love supported me through the hardest trials and enhanced my enjoyment of the happiest occasions. I love you, and I am thankful that we will spend the rest of our lives together.

TABLE OF CONTENTS

CHAPTER

LIST OF FIGURES

xiv

LIST OF TABLES

LIST OF APPENDICES

Appendix

ABSTRACT

Broadband, Volumetric Negative-Refractive-Index Media

by

Scott M. Rudolph

Chair: Anthony Grbic

Since their invention, negative-refractive-index (NRI) media have been plagued by three primary limitations: narrow bandwidth, high loss and polarization dependence. In this thesis, each of these problems is addressed. First, a new metamaterial topology that achieves negative permeability over a broad bandwidth is introduced. This structure is used to realize a broadband, volumetric NRI medium that is then thoroughly analyzed using multiconductor transmission line (MTL) theory. A homogenized, periodic form of MTL analysis is used to derive a simplified dispersion equation, as well as expressions for the Bloch impedance, permittivity and permeability for an infinite NRI medium.

The analytical methods are supported by both full-wave simulation and measured results. Two broadband NRI lenses are presented: one contained inside a waveguide and the other in free space. Both lenses exhibit super-resolving capabilities: the first at 2.45GHz and the second at 10.435GHz. The transmission and reflection coefficients of the free-space lens are measured using a quasioptical Gaussian beam telescope, and the material parameters of the lens are extracted for these measurements. This lens exhibits a negative index of refraction over a fractional bandwidth of 41.2%. The

low-loss performance of this metamaterial lens is experimentally verified. The lens exhibits 0.17dB of loss per unit cell and a figure of merit ($FOM = n'/n''$) of 31.4 at the operating frequency of 10.435GHz. These properties allow the recovery of evanescent spatial frequencies over a bandwidth of 7.4%. Additionally, the measured focal pattern at the image plane of the lens is accurately predicted using the material parameters obtained from the transmission measurements.

A polarization-independent NRI medium is also reported. The design of this structure uses stereolithography and electroplating to complete the requisite three-dimensional fabrication on a large scale (more than 400 unit cells). The NRI bandwidth of this medium is 24%. A NRI lens that operates at 1.54GHz is designed and fabricated using this isotropic topology. At this frequency, the lens produced a super-resolved focus independent of the type of source and its polarization.

CHAPTER I

Introduction

1.1 Background

When building a bridge, the designer does not consider the fact that the steel he is using is actually a collection of iron and carbon atoms. The doctor performing surgery has no need to analyze how the carbon and hydrogen bond together to form human tissue. Instead, both of these professionals treat the materials that they encounter as homogeneous media, each with their own specific properties. Microwave engineers also regard most natural materials as being homogeneous with electrical characteristics specific to each. Despite the fact that all materials consist of molecular and atomic structures, the simplifying assumptions of homogeneous material properties have yielded reliable results in the field of microwave engineering.

The discovery of the atom drastically changed mankind's perception of the objects that surround us. The materials that make up the natural world were no longer uniform regions of space as they were previously thought to be. Instead, any non-vacuous medium was found to consist of microscopic arrangements of particles. Scientist quickly learned that the nature of these particles and how they were arranged gave a particular medium unique material properties. In Fig. 1.1(a) for example, the depicted periodic structure of carbon atoms produces a diamond: the hardest natural mineral and a low-loss dielectric. However, a different periodic arrangement of the

carbon atoms yields graphite (Fig. 1.1(b)): a comparatively soft material and a good electrical conductor. This example demonstrates how the microscopic structure of a material gives rise to its physical and electrical properties.
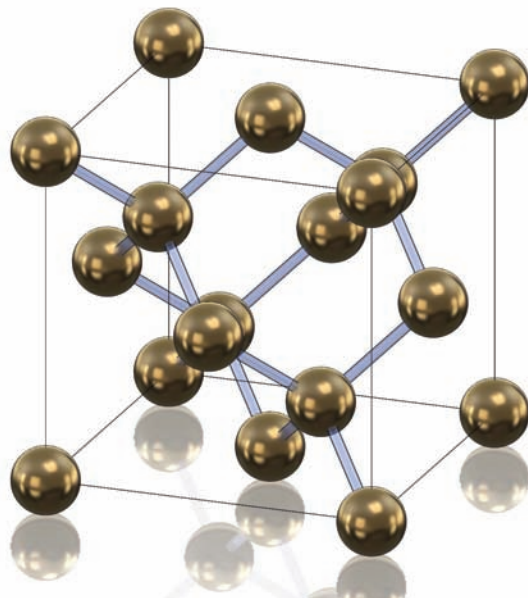
(a) One unit cell of a diamond crystal.
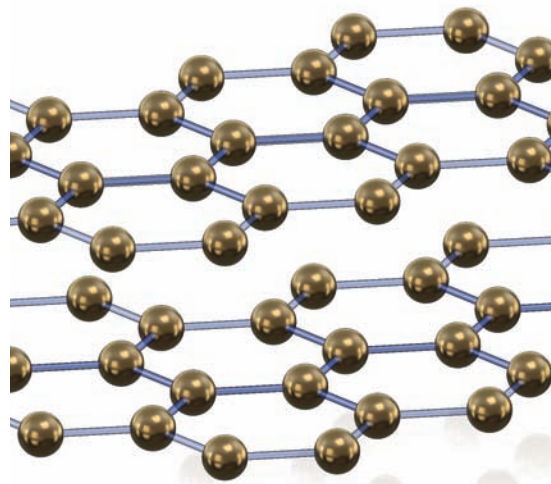
(b) Two layers of the graphite depicting the atomic structure of the material.

Figure 1.1: The atomic structures of two carbon allotropes. The spheres represent carbon atoms, and the rods indicate the bonds between the atoms.

Simply because modern science has demonstrated that materials have an atomic substructure is no reason to stop treating these materials as homogeneous objects. The fields of microwave engineering and optics both existed prior to the development of quantum theory and also predated the discovery of the atom. In these fields, treating materials as homogeneous media allows scientists and engineers to make simple, accurate predictions of the behavior of electromagnetic waves that interact with them. Without this simplified view, the design of most current microwave and optical components would be impractically complex.

However, at higher frequencies, such as gamma and x-rays, natural materials no longer behave as homogeneous media. Rather, they must be considered on the molecular level in order to accurately predict how electromagnetic waves interact with them

[1]. The reason for the difference is that the wavelength of these electromagnetic fields is comparable to or even smaller than the molecular or atomic structure of natural materials. In this case, the medium no longer appears homogeneous. Conversely, if the wavelength of an electromagnetic wave is much larger than the substructure of the medium through which it travels, the wave propagates through the material as though it were completely homogeneous. A consequence of this condition is that the substructure of a material need not be on the atomic or molecular scale to give the appearance of homogeneity at microwave or optical frequencies. Instead, the substructure must only be much smaller than the wavelength of interest.

This concept led to the development of effective medium theory [2]. Using this theory, engineers could combine different materials to achieve effective dielectric constants that were not readily available. Subsequently, metals were also used to achieve desired dielectric material parameters [3, 4, 5]. Fig. 1.2 shows an example of metallic spheres arranged in a periodic lattice used to focus microwaves like an optical lens [4]. The periodic arrangement of the metallic spheres in Fig. 1.2 has a similar appearance to the depiction of the diamond crystal in Fig. 1.1(a). This illustrates the similarities between artificial and natural materials. Both are periodic arrays of inclusions, whose electrical properties change depending on the type and arrangement of the inclusions. The most obvious difference between the two is their periodicity: the diamond crystal lattice is periodic over 0.357nm and behaves like a homogeneous medium for frequencies beyond the optical spectrum, while the array of metallic spheres has a periodicity of several millimeters and exhibits homogeneity for microwave frequencies and below.

The use of metallic inclusions allowed the natural limits of material parameters to be overcome. Artificial dielectrics with uncommon properties, such as media with an effective relative permittivity less than 1 [6] or even less than 0 [7], could be constructed using periodic arrays of wires. While these material parameters seem exotic, such media do exist naturally over limited frequency ranges. Metals exhibit this
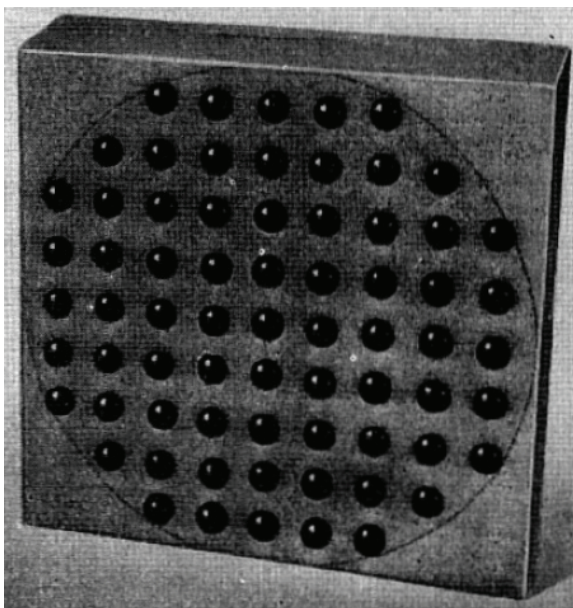
Figure 1.2: An array of metallic spheres used to create a conventional lens at microwave frequencies.

property at optical frequencies and ionized gases display similar performance in the microwave regime. Although the frequency range was still limited, these macroscopic inclusions allowed media to be designed to exhibit specific relative permittivity values less than 1 at nearly any frequency.

In the late 1990s, John Pendry developed an effective medium that broke the limits that nature seemed to set for material parameters. Using metallic inclusions known as split-ring resonators (SRRs), his research group was able to design effective media that exhibited a negative permeability [8]. Since a negative permeability had never been observed in natural materials (although certain natural materials have subsequently been made to exhibit negative permeability by biasing them with external magnetic fields [9, 10]), this structure represented the first medium to exhibit material parameters beyond those found in nature. Taking the Greek word "meta", which means "beyond", these scientists called their new media "metamaterials".

Metamaterials sparked great interest within the electromagnetic and optic communities since they provided the means to realize electromagnetic media that were

never before possible. Of particular interest were media that exhibited both negative permittivity and permeability for overlapping frequency ranges, which Victor Veselago investigated in the 1960s [11]. These media, he showed, would exhibit a negative index of refraction and a positive characteristic wave impedance, leading to phase propagation and power flow in antiparallel directions. This phenomenon was referred to as backward-wave propagation since the unusual phase progression made the waves appear to be propagating backwards through the medium. As a consequence of backward-wave propagation, Veselago demonstrated that flat slabs of negative-refractive-index (NRI) media could focus electromagnetic waves. If properly designed, these flat NRI lenses would also not reflect any energy, which is a shortcoming of all conventional lenses. After demonstrating that SRRs could be used to build NRI media, Pendry revisited Veselago's NRI lens and showed that it would also exhibit the remarkable property of super resolution by restoring a source's evanescent spectrum at the focus [12]. Around the same time, the first metamaterial that exhibited a negative index of refraction was realized [13], consisting of arrays of SRRs and wires.

This achievement ushered in an era of rapid development in the field of metamaterials. Exciting applications, such as the NRI lens and electromagnetic cloaking [14], fueled the popularity of metamaterials. The ability to design materials that exhibit tailored electrical properties gives unprecedented flexibility to scientists and engineers. However, despite the thrilling prospects offered by these media, there are key issues that must be addressed before the field of metamaterials can realize its full potential.

1.2 Motivation

Microwave engineers have been reluctant to incorporate NRI metamaterials into practical applications because of three primary limitations: narrow bandwidth, high

loss and polarization dependence. Because metamaterials give engineers unprecedented control over electromagnetic fields, making them practical represents a significant advance in the discipline of electromagnetism. In order to understand the problems that arise from these limitations and how we can solve them, we must first identify their causes. To do this, let us first consider the typical constitutive elements of NRI media.

Typical NRI media rely on separate inclusions to achieve negative permittivity and negative permeability. As mentioned in the previous section, metallic wire arrays are the most common way to achieve a negative effective permittivity. This is not surprising given that metals naturally exhibit negative permittivity below their plasma frequencies (the frequency at which $\epsilon = 0$), which typically occur in the optical spectrum. Wire arrays are used at microwave frequencies rather than solid metal blocks to lower the plasma frequency into the microwave regime. Unfortunately, materials that naturally exhibit negative permeability are not so readily available. This is because there is no magnetic analogue for an electrical conductor. As a result, the development of a negative effective permeability medium is more complex than an array of wires. Instead SRR arrays are the most common method of producing negative permeability.

SRR arrays produce negative effective permeability by using a resonance to enhance the antiparallel magnetic field produced by the Faraday currents induced in the ring [8]. In a closed ring, a time-varying magnetic flux induces Faraday currents, the amplitudes of which are limited primarily by the loop's inductance. These currents produce a magnetic field which opposes the incident magnetic field, reducing the magnetic flux density. In an array of subwavelength loops, the individual loops exhibit this same behavior, collectively giving the appearance of a diamagnetic medium (that is, a medium with a relative permeability less than 1). The inductance of the loops prevents the average induced magnetic field from overwhelming the incident field,

ensuring that the total magnetic flux density is always in the same direction as the incident magnetic field, and, consequently, the effective permeability of the medium remains positive.

Negative permeability can be achieved by canceling the inductance which limits the Faraday current. This is done by placing a capacitor (or a capacitive gap) in the loop. Since the impedance of the inductance is directly proportional to frequency while the impedance of the capacitance is inversely proportional to it, there must necessarily be a frequency where the magnitude of the capacitive reactance is equal to that of the inductive reactance. At this resonant frequency, the net reactance of the entire loop is zero, meaning the Faraday currents are limited only by the resistive losses in the loop. At frequencies just above the resonance, the high currents produce a magnetic field that is both antiparallel to and higher in amplitude than the incident magnetic field. Treating an array of these resonant loops as an effective medium gives rise to a negative permeability, since the magnetic field incident in a particular direction creates a magnetic flux density in the opposite direction.

Here the issue of loss in SRRs becomes apparent. When the loop's reactance is very small only the resistance of the metallic loop limits the current amplitude. At these frequencies, large currents flow in the loop, and the resistive loss ($I_{loop}^2 R$) is substantial. As the operating frequency is moved away from the resonance, the reactance of the loop begins to limit the current, reducing the resistive losses. Unfortunately, the diminishing current in the loop also reduces the anti-parallel magnetic field responsible for negative permeability, ultimately limiting the bandwidth over which negative permeability can be achieved. The first condition suggests that the operating frequency should be as far away from the resonant frequency as possible. However, the second condition does not permit the desired negative permeability values to be achieved at frequencies far above the resonance.

The typical SRR array can achieve negative permeability over a fractional band-

width of only about 10% [15, 16]. Such narrow bandwidth forces the operating point to be close to the resonant frequency of the split ring, where losses are high. Furthermore, in this frequency range the permeability changes rapidly, further reducing the bandwidth for applications that require a specific relative permeability value. The narrow bandwidth and high loss inherent in SRR arrays make it clear that a new method of realizing negative permeability media is needed.

The preceding discussion demonstrates how the reliance on SRR arrays as negative permeability media has led to the issues of narrow bandwidth and loss. The third issue, polarization dependence, is challenging not because of inherent physical limitations but because of fabrication difficulties. It is not difficult to conceive of a SRR/wire medium that is isotropic and polarization independent; a unit cell of such a design can be seen in Fig. 1.3. However, imagining how to construct this design is much more difficult. An "egg-crate" lattice of SRRs could be implemented using printed-circuit-board technology. In fact, such a design has been constructed for use in magnetic resonance imaging (MRI) [17]. Additionally, the three-dimensional wire grid has also been constructed before. The challenge lies in bringing these components together on a large scale (i.e. hundreds or thousands of unit cells). For instance, the junctions of the wire grid must be electrically connected to achieve isotropic behavior, but access to these junctions is limited since they are surrounded by layers of SRRs on all sides.

Yet even if this challenge could be overcome and a polarization-independent medium could be made, the medium would still exhibit the same bandwidth and loss issues as the polarization-dependent SRR/wire media discussed above. Some structures that exhibit isotropic, polarization-independent NRI over a broader bandwidth have been proposed [18, 19]. Unfortunately, these structures require three-dimensional interconnecting transmission lines, which present fabrication challenges still more daunting than those of the three-dimensional SRR/wire media. In order

8
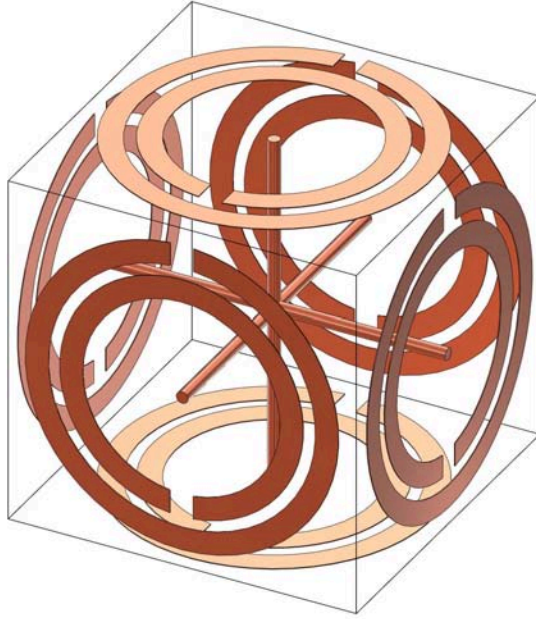
Figure 1.3: One unit cell of an isotropic, polarization-independent SRR/wire medium.

to completely address the issue of polarization dependence, a method of achieving isotropic NRI behavior over a broad bandwidth must be developed with large-scale fabrication in mind.

1.3   Thesis Outline

In this thesis, solutions to all three of the issues discussed in the previous section are presented. In Chapter II, the design of a broadband, low-loss NRI unit cell is introduced. To explain the operation of the structure, a circuit model is derived based on multiconductor-transmission-line (MTL) theory. Two types of MTL analysis are then applied to the structure: traditional and homogenized. The traditional MTL analysis allows for the rapid calculation of the dispersion diagrams and can also be used to calculate the scattering parameters (S-parameters) of finite slabs of the NRI metamaterial. The homogenized MTL analysis allows for the derivation of closed-form equations for the propagation constant, impedance, permittivity and permeability. These expressions provide intuition into the NRI medium's operation

and insight into how such a structure can be optimized.

Chapter III discusses the realization of broadband, polarization-dependent NRI lenses in experiment. Two designs for NRI lenses are presented: the first contained in a parallel plate waveguide and the second in free space. Both designs are realized through printed-circuit-board technology, making them simple to fabricate. The designs are tested through near-field focusing experiments, and both lenses exhibit resolution beyond the diffraction limit at their operating frequencies. For the free-space design, the normal-incidence S-parameters are also presented. The measured S-parameters allow the calculation of the material properties of the NRI lens which are reported in this chapter as well. The measured material parameters are used to predict the focusing abilities of the NRI lens with good agreement, demonstrating the validity of the effective medium theory for these metamaterials.

In Chapter IV, the design of a broadband, low-loss, polarization-independent NRI medium is introduced. The structure relies on a new, three-dimensional element to achieve negative permeability called the split-cube resonator (SCR). The SCRs achieve negative permeability over a much larger bandwidth than an array of SRRs. Using these elements, the fabrication of an isotropic NRI lens is presented in detail. Near-field measurements in free space demonstrate the isotropy of the lens by achieving super-resolved focusing with the same beamwidth independent of the orientation of the lens with respect to the source. Analytical derivations of the predicted field patterns corroborate the near-field focusing results for both electric and magnetic dipole sources.

Finally, Chapter V provides a summary of the work presented in this thesis. The notable achievements are outlined, and conclusions drawn from the research are briefly discussed. Several ideas for future research in NRI metamaterials are also presented. Some expand upon the work presented in the previous chapters, while others highlight directions not investigated in this thesis. A list of the publications resulting from the

contributions of this thesis is also given.

CHAPTER II

The Design of Broadband, Low-Loss, Volumetric NRI Media

2.1   The Development of Broadband Negative-Refractive-Index Media

Of all the issues affecting negative-refractive-index (NRI) metamaterials, the narrow bandwidth of split-ring resonator (SRR)/wire media represents the most significant limitation. Using SRR arrays to achieve negative permeability constrains the fractional NRI bandwidths of these media to approximately 10%. To make matters worse, the material parameters are dispersive throughout this frequency range. The SRR arrays exhibit a Lorentzian permeability response [8], and the permittivity of the wire arrays follows the Drude model [7]. Consequently, specific material parameters can only be maintained with reasonable tolerances over a fraction of the 10% bandwidth. To make NRI metamaterials practical, their bandwidth must be improved. When freed from this limitation, engineers can fully embrace the positive attributes of NRI media.

2.1.1 NRI Transmission-Line Media

Shortly after the introduction of SRR/wire arrays, a new class of NRI metamaterials was developed: NRI transmission lines [20, 21, 22, 23, 24]. Their invention provided a new perspective on NRI media. Rather than loading positive-refractive-index media with resonant inclusions like the SRR, the loading elements in NRI transmission lines are standard circuit components. To make a NRI transmission line, loading capacitors are placed periodically in series with a standard transmission line, and loading inductors are connected in parallel with the same periodicity. The circuit diagram depicting one unit cell of this configuration is shown in Fig. 2.1. In this topology, the negative series reactance of the loading capacitors overcomes the positive series reactance of the transmission-line inductor at low frequencies. By making the series reactance negative, the transmission line now appears to have negative permeability. Similarly, the negative shunt susceptance of the loading inductor overcomes the positive shunt susceptance of the transmission-line capacitance, which is equivalent to the transmission line exhibiting negative permittivity.
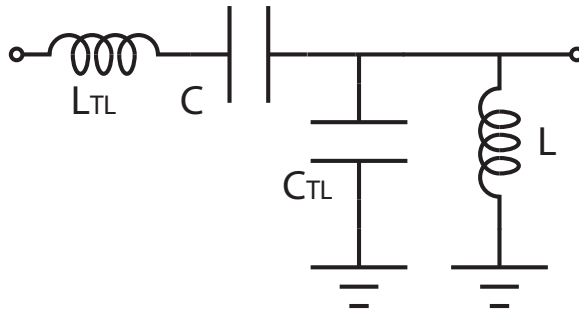
Figure 2.1: One unit cell of a NRI transmission line.

By exhibiting negative material parameters, the NRI transmission lines were similar to traditional SRR/wire media. However, the backward-wave bandwidth of the NRI transmission lines was substantially greater than that of the SRR/wire arrays. The reason for this was that the loading capacitor decreases the series reactance over all frequencies and gives the transmission-line medium a Drude permeability re-

sponse. This means that the effective permeability of a NRI transmission line does not depend on a narrowband resonance as is the case for SRR arrays. Consequently, negative permeability (as well as NRI) can be achieved over much broader bandwidths in transmission-line media.

Unfortunately, with propagation confined to circuit boards, the NRI transmission lines could not interface directly with free-space electromagnetic waves like SRR/wire media. For this reason, NRI transmission lines are referred to as "planar" metamaterials, while the SRR/wire arrays are described as "volumetric" metamaterials. Many of the envisioned applications of NRI media, such as free-space lenses, radomes and waveguide filters, require that the metamaterials interact with volumetric electromagnetic waves rather than voltages and currents on a transmission-line network. Consequently, planar NRI transmission lines could not be used as replacements for volumetric NRI media such as SRR/wire arrays, despite their superior backward-wave bandwidths.

Although NRI transmission lines cannot interface effectively with free-space waves, examining the reasons behind their broadband performance can help determine how volumetric NRI media can be improved. The wires in the SRR/wire array are the volumetric analogue of the inductors in the planar NRI transmission lines. Both cause their respective media to exhibit a Drude permittivity response, which provides negative permittivity with minimal dispersion. By designing the electric plasma frequency (where $\epsilon_r = 0$) to occur at or above the magnetic plasma frequency (where $\mu_r = 0$), the negative permittivity medium does not limit the NRI bandwidth at all. Instead, it is the negative permeability medium that is responsible for the bandwidth limitations of volumetric NRI metamaterials. Unfortunately, the series capacitors in NRI transmission lines do not have a volumetric analogue capable of achieving a Drude permeability response. Theoretically, the analogue should be a wire made of a magnetic conductor oriented in the direction of the magnetic field, but magnetic

conductors do not exist. Still, other characteristics of planar metamaterials can be used to improve the performance of volumetric NRI media.

In NRI transmission lines, the loading components are integrated into the host transmission line to form a traveling-wave structure. Traveling-wave structures, such as distributed amplifiers [25] and traveling-wave antennas [26], are known for their broadband operation. Each SRR, on the other hand, is an isolated LC resonator that does not interact significantly with its neighboring elements. Consequently, the effective permeability of SRR arrays changes rapidly with frequency, particularly close to the LC resonance. However, if the SRRs could be made into a traveling-wave structure, the medium would no longer be reliant on an isolated resonance to achieve negative permeability and would be less dispersive as a result.

2.1.2 Realization of Broadband, Volumetric Negative Permeability

2.1.2.1 The Transmission-Line Cage

To transform the isolated SRRs into a traveling-wave structure, researchers sought to increase the coupling between neighboring SRRs. First, inductive coupling was used in the form of magnetoinductive waves [27]. This did increase the bandwidth of the negative permeability response, however, the mutual inductance between the neighboring SRRs was insufficient to produce anything beyond a marginal improvement. The coupling between neighboring SRRs will be greatest if adjacent SRRs are electrically connected, forming a "transmission-line cage" [28, 29], as depicted in Fig. 2.2. The individual transmission-line cage unit cell appears as either a two-dimensional array of SRRs that are electrically connected in the horizontal directions (Fig. 2.3(a)) or a two-dimensional grid of two-wire NRI transmission lines (Fig. 2.3(b)), depending on the planes chosen for the unit-cell boundaries. Both perspectives indicate that the structure will exhibit broadband behavior. When viewed as Fig. 2.3(a), the perfect coupling between SRRs leads one to expect a wide-band

frequency response. Considering the structure as a grid of NRI transmission lines emphasizes the traveling-wave nature of the transmission-line cage, which suggests the structure should be minimally dispersive.
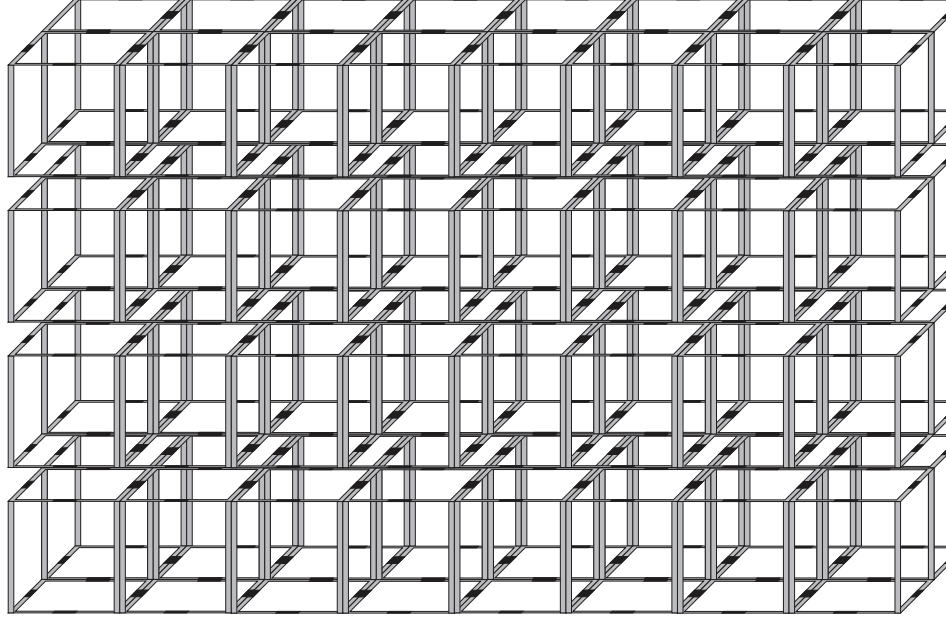
Figure 2.2: An array of electrically connected SRRs which forms the broadband negative permeability medium. The black rectangles represent chip capacitors used to tune the resonance of the transmission-line cage.

It should be noted that the structures in Figs. 2.2 and 2.3 only produce negative permeability for horizontally polarized magnetic fields. For this polarization, negative permeability is achieved by enhancing the Faraday currents induced in the transmission-line cage, similar to what happens in SRR arrays [8]. However, if the magnetic field is vertically polarized, the connections between adjacent rings cause the currents induced in one ring to cancel the currents induced by its neighbors. The induced currents would cancel in a similar fashion for horizontally polarized magnetic fields if the rings were electrically connected in the vertical direction. For this reason, the electrical connections are only made in the horizontal directions, while the vertical layers remain separated.

To observe the propagation characteristics of the transmission-line cage, the dis-

(a) SRR view of the transmission-line cage.

(b) Two-wire NRI transmission-line view of the transmission-line cage.
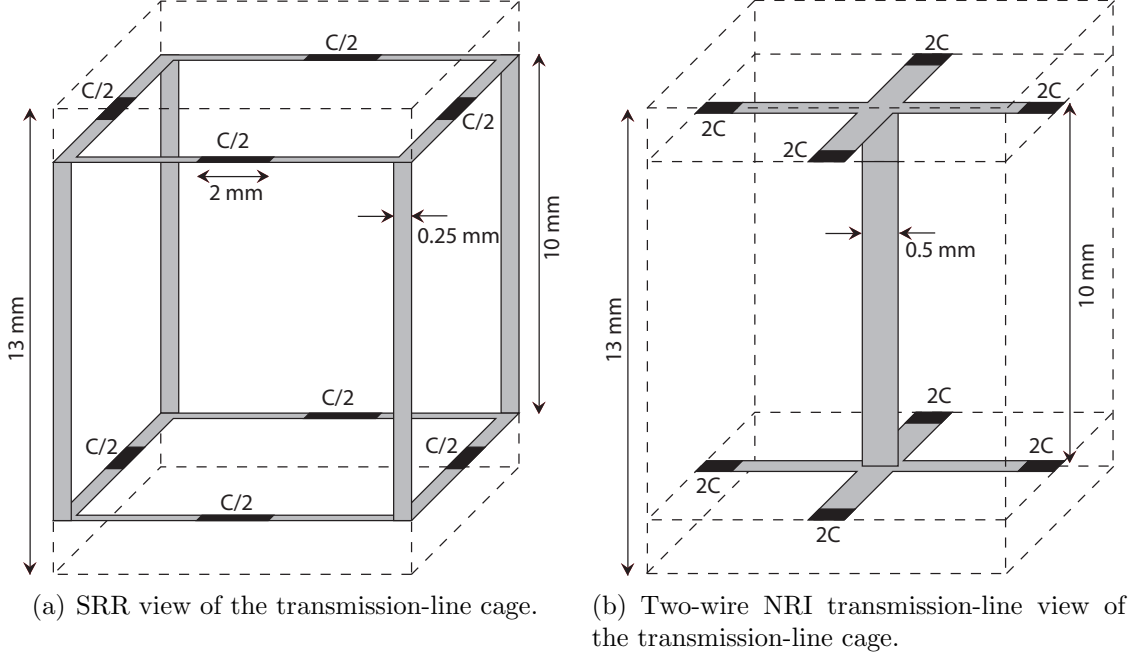
Figure 2.3: Two perspectives of the transmission-line cage unit cell. The

persion diagram for on-axis propagation in the horizontal direction was calculated through full-wave simulation and is plotted in Fig. 2.4 (for an explanation of dispersion diagrams, refer to Appendix A). The modes of interest are plotted with solid lines and correspond to the magnetic field polarized in the horizontal direction; the dotted lines denote modes in which the magnetic field is vertically polarized. Since the transmission-line cage exhibits positive permittivity over all frequencies for the modes of interest, the frequency range over which the medium exhibits negative permeability corresponds to a stopband in the dispersion diagram. The medium exhibits negative permeability from 1.71GHz to 3.22GHz: a fractional bandwidth of 61%. This bandwidth is approximately six times the typical bandwidth of SRR arrays [15, 16].

2.1.2.2 Contra-Directional Coupling

To better understand the performance of the transmission-line cage, the unit cell shown in Fig. 2.3 can be simplified without affecting the modes of interest. As mentioned earlier, the electric field is vertically polarized and the magnetic field is

17
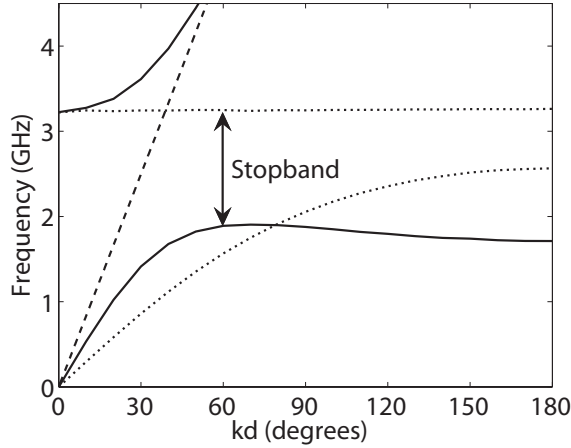
Figure 2.4: The dispersion diagram of the first four modes of the transmission-line cage. The solid lines correspond to modes with the electric field polarized vertically, while dotted lines show the modes with horizontal electric fields. The dashed line shows the light line.

polarized horizontally and orthogonal to the direction of propagation. For this polarization, the vertical periodicity can be modeled through image theory by placing perfect electrical conductors (PECs) on the top and bottom of the unit cell, as shown in stage II of Fig. 2.5. This is equivalent to placing the transmission-line cage in a parallel plate waveguide. To make the structure still simpler, image theory can be applied again to replace the bottom half of the unit cell with a PEC (stage III of Fig. 2.5). The structure can now be shifted by half a unit cell in each of the horizontal directions, as shown in stage IV of Fig. 2.5. After these transformations, the structure looks like a two-dimensional microstrip NRI transmission-line grid inside a parallel plate waveguide. Examining the dispersion characteristics of these two structures in isolation suggests that they contra-directionally couple to form the modes of interest in the dispersion diagram shown in Fig. 2.4. It should be noted that propagation within the parallel plate waveguide is equivalent to propagation in free space because the conductors that form the parallel plate waveguide arise from modeling the vertical periodicity of the volumetric medium with image theory. As a result, the contra-directional coupling between the NRI transmission-line grid and

18
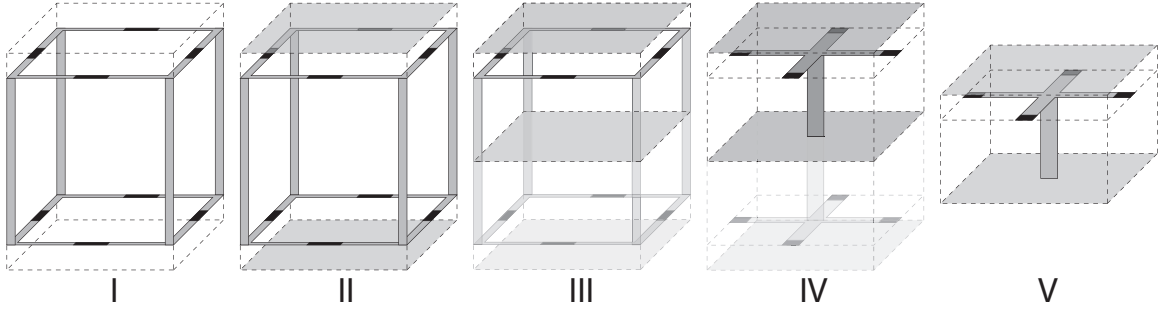
Figure 2.5: Transformation of the transmission-line cage unit cell into a microstrip NRI transmission line within a parallel plate waveguide. Stage I represents the initial connected-SRR form of the transmission-line cage. Stage II models the vertical periodicity with parallel conductors on the top and bottom of the unit cell. Stage III employs image theory again to replace the bottom half of the unit cell with a conducting plate. Stage IV shifts the unit cell half a cell in both horizontal directions to view the connected SRRs as a grid of NRI transmission lines. Stage V represents the unit cell as a NRI transmission-line grid contained in a parallel plate waveguide.

the parallel plate waveguide represents the interaction of the transmission-line cage with free-space waves.

The dispersion curves for the transmission-line cage are again shown in Fig. 2.6, accompanied by the those of both the isolated microstrip NRI transmission-line grid and the empty parallel plate waveguide. The microstrip NRI transmission-line grid was simulated using Agilent's Advanced Design System (ADS), a commercial microwave circuit simulator. It was modeled by lossless microstrip lines loaded with series capacitors and shunt inductors (representing the vertical metallic strips in the cage) with the same dimensions and component values as are shown in Fig. 2.3(b). The empty parallel plate waveguide's dispersion curve coincides with the light line, as is expected since it models free-space propagation. By examining Fig. 2.6, it is evident that the modes of the transmission-line cage arise from the interaction between the waves guided by the microstrip NRI transmission-line grid and the empty parallel plate waveguide. At lower frequencies, the forward-wave mode of the parallel plate waveguide is dominant because the NRI transmission line is still in cutoff. However,
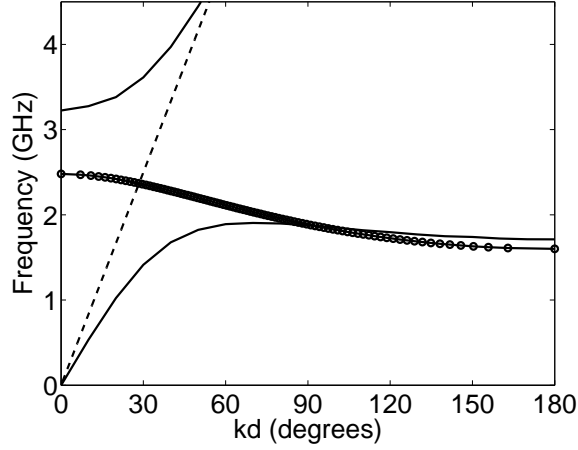
Figure 2.6: The dispersion curves of the isolated microstrip NRI transmission-line grid (solid line with circles) and the unloaded parallel plate waveguide (dashed). Coupling between these two structures forms the dispersion curve of the transmission-line cage (solid). The microstrip NRI transmission-line grid dispersion curve was generated using ADS.

when the two modes are present at the same frequency, contra-directional coupling occurs between the forward wave propagating within the parallel plate waveguide and the backward wave guided by the NRI transmission line. This contra-directional coupling produces a stopband which extends from 1.90GHz to 3.22GHz.

2.1.3 The Broadband NRI Medium

With the development of a metamaterial that exhibits negative permeability over a wide frequency range, achieving broadband NRI is relatively simple. As mentioned in Chapter I, the narrowband response of the SRRs was the limiting factor in the NRI bandwidth of SRR/wire arrays. The wire array used in these metamaterials did not constrain the bandwidth because it exhibited a Drude permittivity response. This meant the negative permittivity frequency range was limited only at high frequencies by the electric plasma frequency, which could be easily manipulated by changing the effective inductance of the wires. Since the transmission-line cage allows negative permeability to be achieved over a wide range of frequencies, adding appropriately sized wires to each unit cell should result in a NRI bandwidth equal to the negative

20
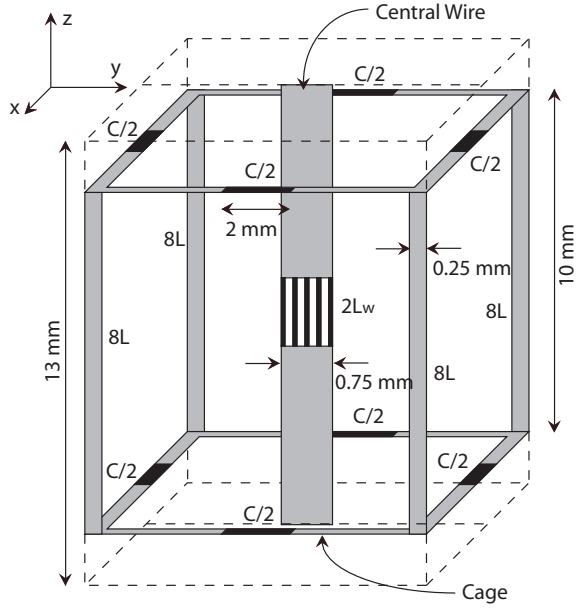
Figure 2.7: Unit cell of the broadband volumetric negative-refractive-index (NRI) medium. The central wire has a total inductance of $2 \cdot L_w$.

permeability bandwidth of the transmission-line cage.

Rather than simply adding wires, negative permittivity was achieved by adding an inductively loaded metallic strip to the center of the transmission-line cage unit cell, as shown in Fig. 2.7. The loading inductor allowed the inductance of the central strip to be manipulated directly, making it easier to tune the effective permittivity of the NRI medium. To verify that the wire/transmission-line cage medium did indeed exhibit a NRI, the dispersion diagram for on-axis propagation in the horizontal direction was calculated using full-wave eigenmode simulations (Fig. 2.8). NRI behavior was observed from 1.71GHz to 3.17GHz, which is nearly the same frequency range over which negative permeability was achieved in the transmission-line cage. The fractional NRI bandwidth of the structure was 60%: close to a six-fold increase over the typical SRR/wire fractional bandwidths.

21
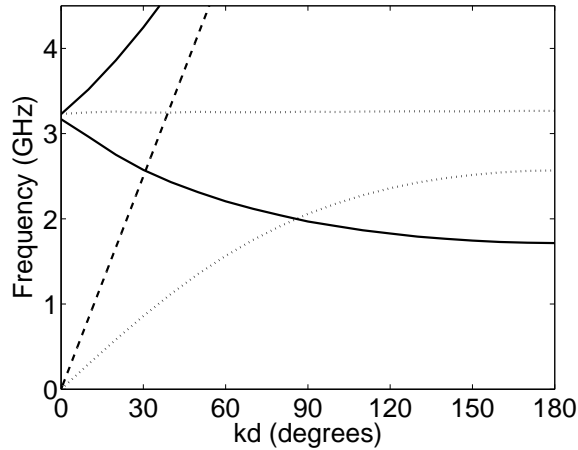
Figure 2.8: The dispersion diagram of the first four modes of the NRI metamaterial. The solid lines correspond to modes with the electric field polarized vertically, while dotted lines show the modes with horizontal electric fields. The dashed line shows the light line.

2.2 Analytical Modeling of the Broadband NRI Medium Using Multiconductor-Transmission-Line Theory

Wire/transmission-line cage metamaterials provided a means to achieve broadband volumetric NRI media, but no procedure existed to design them efficiently. Simple, accurate methods of designing planar NRI transmission-line media in one- and two-dimensions are well-established [30, 31]. SRR/wire media also have closed-form equations for the permeability of SRR arrays [8] and the permittivity of periodic wire media [7, 32]. Unfortunately, none of these design methods are applicable to wire/transmission-line cage media. The equations for NRI transmission lines apply only to planar transmission-line networks, so the vertical periodicity of the transmission-line cage medium precludes these formulae from predicting its performance. The expressions derived for SRR/wire media do not account for coupling between SRRs. Since the SRRs are electrically connected in the transmission-line cage, these equations also cannot be used. Even if the coupling between SRRs could be modeled, problems would arise concerning the permittivity of the medium because the permittivity expressions for wire arrays do not account for the electrical

22

effect of the SRRs. As a result of these issues, a new method is needed to model these broadband volumetric NRI media.
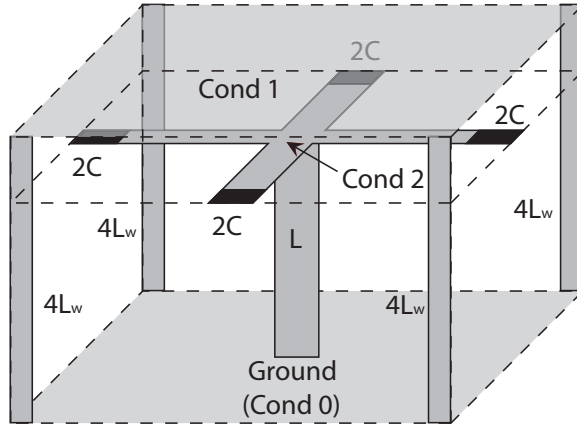
Figure 2.9: One unit cell of the MTL representation of the broadband NRI medium.

Fig. 2.5 shows that, for the polarization of interest, the broadband volumetric negative permeability medium can be represented as a NRI transmission-line grid inside of a parallel plate waveguide. In [33, 34], structures similar to stage V of Fig. 2.5 were modeled using multiconductor transmission-line (MTL) theory [35, 36]. For this analysis, the bottom conductor serves as the reference conductor for both the NRI microstrip transmission line as well as the parallel plate waveguide. By representing the parallel plate waveguide and the microstrip line as a MTL circuit, the coupling between the two conductors is inherently taken into account. Adding metallic strips from the parallel plate waveguide to ground, as shown in Fig. 2.9, introduces negative permittivity to the negative permeability medium. Representing the broadband NRI medium in this way shows that MTL analysis can be applied to this structure as well.

2.2.1 General Multiconductor Transmission Line Theory

Before analyzing the transmission-line cage, a brief introduction to MTL analysis will be provided. MTL theory is a more general version of standard transmission-line theory taught in undergraduate classes on electromagnetism. The generalization is
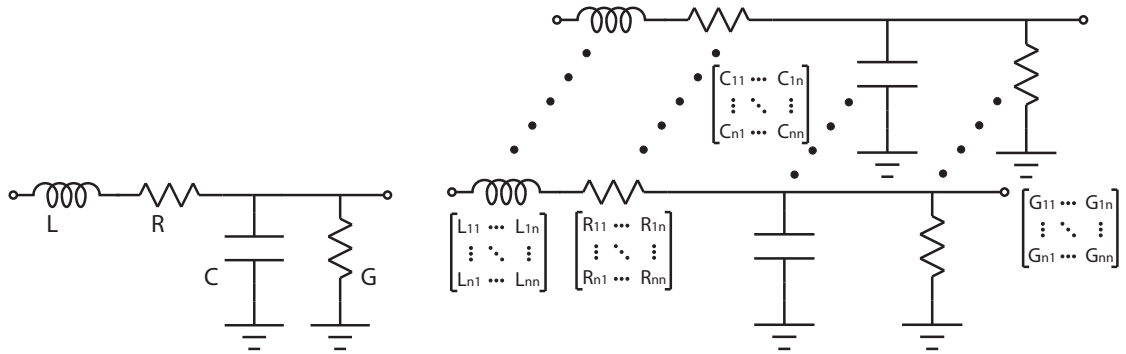
(a) The lumped-element circuit representation of a single transmission line.

(b) The lumped-element circuit representation of a multiconductor transmission line.

Figure 2.10: Lumped element representations of single and multiconductor transmission lines.

achieved through the use of vectors and matrices, which allows the voltage and current relationships for multiple conductors to be expressed in a single matrix equation.

To illustrate the similarities between MTL and traditional circuit theory, consider the familiar lumped-element circuit model for a single transmission line shown in Fig. 2.10(a). Propagation along this line is governed by the well known time-harmonic transmission-line equations (telegrapher's equations):

$$-\frac{d}{dx}V = ZI \tag{2.1a}$$

$$-\frac{d}{dx}I = YV. \tag{2.1b}$$

Here V and I are the voltage and current waves on the transmission line, respectively, and x is the propagation direction. Z is the series impedance of the transmission line (defined as $Z = j\omega L + R$ in terms of the circuit elements in Fig. 2.10(a)), and Y is its shunt admittance (defined as $Y = j\omega C + G$). These two equations govern the propagation of voltages and currents along any single transmission line.

Taking the derivative with respect to x of Eq. (2.1a) and substituting in Eq.

24

(2.1b) yields the one-dimensional Helmholtz equation:

$$\frac{d^2}{dx^2}V = ZYV. \tag{2.2}$$

The linear combination of the two solutions to Eq. (2.2) gives the voltage on the line as a function of position:

$$V(x) = e^{-\sqrt{ZY}x}V^+ + e^{\sqrt{ZY}x}V^- \tag{2.3}$$
$$= e^{-\gamma x}V^+ + e^{\gamma x}V^-,$$

where V^+ and V^- are the complex amplitudes of the forward- and backward-traveling waves, respectively. Eq. (2.3) also defines the propagation constant of the transmission line as

$$\gamma = \sqrt{ZY}, \tag{2.4}$$

which, in the lossless case, leads to the familiar

$$\gamma = j\omega\sqrt{LC}. \tag{2.5}$$

Substituting Eq. (2.3) into Eq. (2.1a) gives a similar expression for the current on the line as a function of position:

$$I(x) = \frac{\gamma}{Z}\left(e^{-\sqrt{ZY}x}V^+ - e^{\sqrt{ZY}x}V^-\right)$$
$$= \sqrt{\frac{Y}{Z}}\left(e^{-\sqrt{ZY}x}V^+ - e^{\sqrt{ZY}x}V^-\right) \tag{2.6}$$
$$= \frac{1}{Z_0}\left(e^{-\sqrt{ZY}x}V^+ - e^{\sqrt{ZY}x}V^-\right),$$

This expression defines the characteristic impedance of the transmission line as

$$Z_0 = \frac{\gamma}{Z} = \sqrt{\frac{Z}{Y}}, \tag{2.7}$$

or, in the lossless case,

$$Z_0 = \sqrt{\frac{L}{C}}. \tag{2.8}$$

MTL theory extends this same analysis to any number of parallel transmission lines. In the case of n transmission lines shown in Fig. 2.10(b) (plus a reference ground conductor), the voltages and currents on each line are represented by $n \times 1$ vectors, $\mathbf{V}$ and $\mathbf{I}$, with each element representing the voltage or current on a specific conductor. Consequently, $\mathbf{Z}$ and $\mathbf{Y}$ are $n \times n$ impedance and admittance matrices, respectively, defined as $\mathbf{Z} = j\omega\mathbf{L} + \mathbf{R}$ and $\mathbf{Y} = j\omega\mathbf{C} + \mathbf{G}$ in accordance with the circuit diagram in Fig. 2.10(b). The diagonal elements of these matrices describe how the voltage on each line affects the current on the same line. The off-diagonal elements represent the mutual coupling between each transmission line. Therefore, if the transmission lines in a circuit are uncoupled, the matrices representing that circuit would be diagonal. Generally, all of the matrix elements are assumed to be non-zero, so the multiconductor telegrapher's equations are

$$\frac{d}{dx}\begin{bmatrix} V_1 \\ \vdots \\ V_n \end{bmatrix} = \begin{bmatrix} Z_{11} & \cdots & Z_{1n} \\ \vdots & \ddots & \vdots \\ Z_{n1} & \cdots & Z_{nn} \end{bmatrix}\begin{bmatrix} I_1 \\ \vdots \\ I_n \end{bmatrix} \longrightarrow -\frac{d}{dx}\mathbf{V} = \mathbf{ZI} \tag{2.9a}$$

$$\frac{d}{dx}\begin{bmatrix} I_1 \\ \vdots \\ I_n \end{bmatrix} = \begin{bmatrix} Y_{11} & \cdots & Y_{1n} \\ \vdots & \ddots & \vdots \\ Y_{n1} & \cdots & Y_{nn} \end{bmatrix}\begin{bmatrix} V_1 \\ \vdots \\ V_n \end{bmatrix} \longrightarrow -\frac{d}{dx}\mathbf{I} = \mathbf{YV}. \tag{2.9b}$$

By eliminating $\mathbf{I}$ from Eqs. (2.9a) and (2.9b), the multiconductor telegraphers equations yield a one-dimensional Helmholtz equation, which describes propagation

in the $\hat{x}$ direction:

$$\frac{d^2}{dx^2}\mathbf{V} = \mathbf{ZYV}. \tag{2.10}$$

Solving this equation for $\mathbf{V}$ yields

$$\mathbf{V}(x) = e^{-\sqrt{\mathbf{ZY}}x}\mathbf{V}^+ + e^{\sqrt{\mathbf{ZY}}x}\mathbf{V}^- \tag{2.11}$$

$$= e^{-\sqrt{\mathbf{\Gamma}}x}\mathbf{V}^+ + e^{\sqrt{\mathbf{\Gamma}}x}\mathbf{V}^-,$$

where $\mathbf{V}^{\pm}$ represents the complex voltage waves traveling on each conductor in either the positive or negative $\hat{x}$ direction. Eq. (2.11) defines the propagation constant of the MTL transmission line as the matrix

$$\mathbf{\Gamma} = \sqrt{\mathbf{ZY}}. \tag{2.12}$$

For a brief discussion concerning $\mathbf{\Gamma}$ and the calculation of the exponential propagation matrix $e^{-\sqrt{\mathbf{\Gamma}}x}$, refer to Appendix B.

Inserting Eq. (2.11) into Eq. (2.9a) gives the expression for the currents on the transmission lines:

$$\mathbf{I}(x) = \mathbf{Z}^{-1}\mathbf{\Gamma}\left(\mathbf{e}^{-\sqrt{\mathbf{\Gamma}}x}\mathbf{V}^+ - \mathbf{e}^{\sqrt{\mathbf{\Gamma}}x}\mathbf{V}^-\right). \tag{2.13}$$

Comparing Eq. (2.13) to Eq. (2.6), it can be seen that the characteristic impedance matrix of the MTL system is defined by the relationship

$$\mathbf{Z_0}^{-1} = \mathbf{Z}^{-1}\mathbf{\Gamma} \longrightarrow \mathbf{Z_0} = \mathbf{\Gamma}^{-1}\mathbf{Z}. \tag{2.14}$$

It is interesting to note that the characteristic impedance matrix of the MTL circuit cannot be simplified to the familiar form of Eq. (2.8) because the matrices in Eq. (2.14) do not cancel in the same way as scalar variables do.

Using Eqs. (2.11) and (2.13), the relationship between the voltages and currents

at different positions along the transmission lines can be calculated using $2n \times 2n$ transfer matrices (ABCD matrices) [35]:

$$\begin{bmatrix} \mathbf{V}\,(l) \\ \mathbf{I}\,(l) \end{bmatrix} = \begin{bmatrix} \cosh\left(\mathbf{\Gamma}l\right) & -\sinh\left(\mathbf{\Gamma}l\right)\mathbf{Z_0} \\ -\mathbf{Y_0}\sinh\left(\mathbf{\Gamma}l\right) & \mathbf{Y_0}\cosh\left(\mathbf{\Gamma}l\right)\mathbf{Z_0} \end{bmatrix} \begin{bmatrix} \mathbf{V}\,(0) \\ \mathbf{I}\,(0) \end{bmatrix}$$
$$= \begin{bmatrix} \mathbf{A_{TL}} & \mathbf{B_{TL}} \\ \mathbf{C_{TL}} & \mathbf{D_{TL}} \end{bmatrix} \begin{bmatrix} \mathbf{V}\,(0) \\ \mathbf{I}\,(0) \end{bmatrix}, \tag{2.15}$$

where $\mathbf{Y_0} = \mathbf{Z_0}^{-1}$. The transfer matrix of a MTL system is particularly powerful since it contains both the propagation constant matrix ($\mathbf{\Gamma}$) and the characteristic impedance matrix ($\mathbf{Z_0}$) of the circuit. Once the transfer matrix of a MTL system has been obtained, the effects of arbitrary excitations and terminations can be propagated along the transmission lines.

2.2.2 Defining the Wire/Transmission-Line Cage Medium as a Multiconductor Transmission-Line Circuit

For the remainder of this chapter, the discussion will be limited to the specific case of the wire/transmission-line cage medium. Since this structure has two transmission lines that share a common ground conductor (the parallel plate waveguide and the NRI transmission-line grid), the matrices associated with this analysis will be 2×2. The parallel plate waveguide is defined as conductor 1, while conductor 2 represents the microstrip transmission line. The vertical metallic strips are modeled as lumped inductors, as shown in the MTL model in Fig. 2.11.

Before beginning the MTL analysis, the values of the loading elements and the impedance and admittance matrices of the unloaded transmission lines must be found. In this case, the conductors are assumed to be lossless, so the impedance and admit-
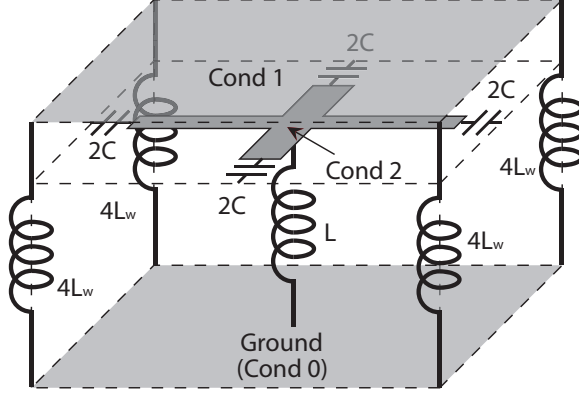
Figure 2.11: One unit cell of the MTL representation of the broadband NRI medium shown in Fig. 2.7.

tance matrices are entirely determined by the inductance and capacitance matrices:

$$
\begin{bmatrix} Z_{11} & Z_{12} \\ Z_{21} & Z_{22} \end{bmatrix} = j\omega \cdot \begin{bmatrix} L_{11} & L_{12} \\ L_{21} & L_{22} \end{bmatrix} \tag{2.16a}
$$

$$
\begin{bmatrix} Y_{11} & Y_{12} \\ Y_{21} & Y_{22} \end{bmatrix} = j\omega \cdot \begin{bmatrix} C_{11} & C_{12} \\ C_{21} & C_{22} \end{bmatrix}. \tag{2.16b}
$$

The values of the capacitance and inductance matrices are obtained in the static limit by modeling the unloaded conductors using Ansoft's Maxwell, a commercial finite-element electromagnetic simulator. Since separation between the conductors is small compared to the wavelength for the frequencies of interest, the static solution is accurate. The values of the loading elements (L, L_w and C) are extracted from full-wave simulations at the frequency of operation using Ansoft's HFSS. These values were found to vary negligibly over the entire frequency range of interest. The values of all the variables used in this MTL analysis are tabulated in Tab. 2.1.

Parameter	Value	Description
L_{11}	812.04 nH/m	Self inductance of the parallel plate waveguide
L_{21}	626.92 nH/m	Mutual inductance between the transmission lines
L_{22}	1085.8 nH/m	Self inductance of the NRI transmission-line grid
C_{11}	32.33 pF/m	Self capacitance of the parallel plate waveguide
C_{21}	-24.12 pF/m	Mutual capacitance between the transmission lines
C_{22}	31.25 pF/m	Self capacitance of the NRI transmission-line grid
L	2.89 nH	Loading inductor of the NRI transmission-line grid
L_w	5.41 nH	Loading inductor of the parallel plate waveguide
C	0.388 pF	Loading capacitor of the NRI transmission-line grid
d	10 mm	Horizontal dimension of the MTL unit cell
h	6.5 mm	Vertical dimension of the MTL unit cell

Table 2.1: Design parameters for the MTL system shown in Fig. 2.9.

2.3 Traditional MTL Analysis

To apply MTL analysis to the structure shown in Fig. 2.9, the structure must first be broken up into its constitutive elements: coupled transmission lines, loading capacitors and loading inductors. The circuit which models on-axis propagation in the NRI medium is shown in Fig. 2.12(a), with dashed lines delineating individual components. Transfer matrices for each of the elements are shown in Fig. 2.12(b), where the transfer matrices of the transmission-line segments are defined by Eq. 2.15. These matrices can then be combined through standard matrix multiplication in the order shown in Fig. 2.12(b) to obtain the transfer matrix of the entire unit cell [35, 36]. From this complete transfer matrix, the propagation characteristics of the broadband NRI medium can be determined.

2.3.1 Dispersion Diagrams

2.3.1.1 NRI Medium

Recalling from Eq. (2.15) that a transfer matrix actually consists of four $n \times n$ (here, 2×2) submatrices, it can be noted that the upper left submatrix depends only on the propagation constant of the medium: $\mathbf{A_{TL}} = \cosh \mathbf{\Gamma} l$. Diagonalizing
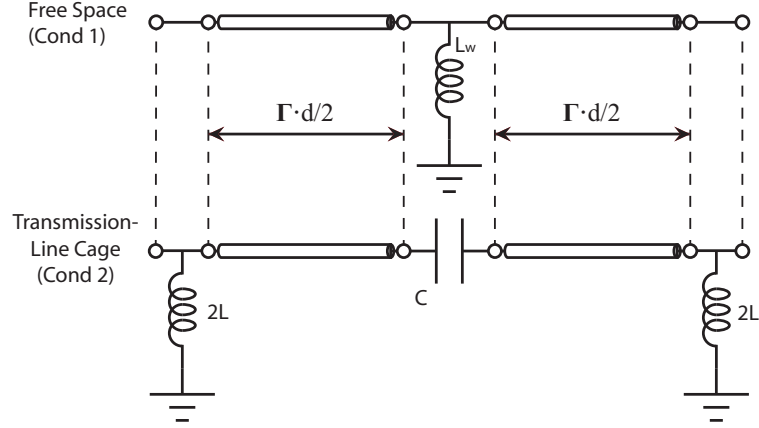
(a) MTL circuit model of the NRI transmission-line medium.
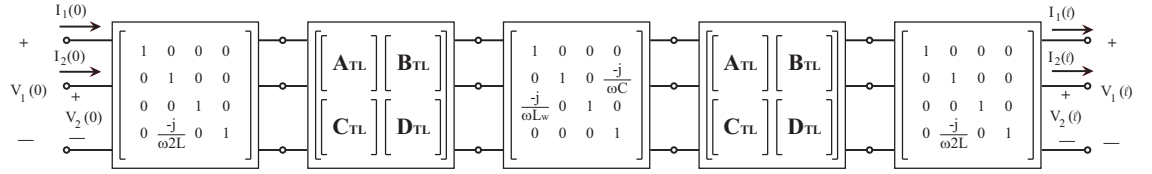
(b) Cascaded transfer matrices of the circuit elements shown in Fig. 2.12(a). The elements of the transmission-line transfer matrix can be found in Eq. (2.15).

Figure 2.12: MTL circuit and matrix representations of the broadband NRI medium.

this submatrix and solving for the propagation constant yields the permitted modes for the infinite medium, γ_c and γ_π [37]. By applying this analysis over a range of frequencies, the dispersion diagram of the NRI medium is given by the imaginary part of propagation constants ($\Im\{\gamma_{c,\pi}\}$). Over the frequency ranges for which the eigenmodes are in cutoff, the attenuation constants are given by the real parts of $\gamma_{c,\pi}$. The attenuation and propagation constants of both modes of the NRI medium are plotted in Fig. 2.13.

As can be seen in Fig. 2.13, the c-mode of the NRI medium is in cutoff throughout the frequency range of interest. The attenuation constant of this mode is over 100Np/m throughout this frequency range. Thus, the π-mode is the only mode present in the NRI structure. This mode exhibits the anticipated NRI behavior over a wide frequency range. To examine the accuracy of this analysis, the propagation constant calculated using MTL theory is compared to that obtained from finite ele-

31

ment simulations (also plotted in Fig. 2.13) with good agreement. It should be noted that MTL analysis does not predict the modes that are polarized orthogonally to the modes of interest (plotted with dotted lines in Fig. 2.8). This is because the image theory used to transform Fig. 2.7 into Fig. 2.9 is only valid for vertically polarized electric fields.
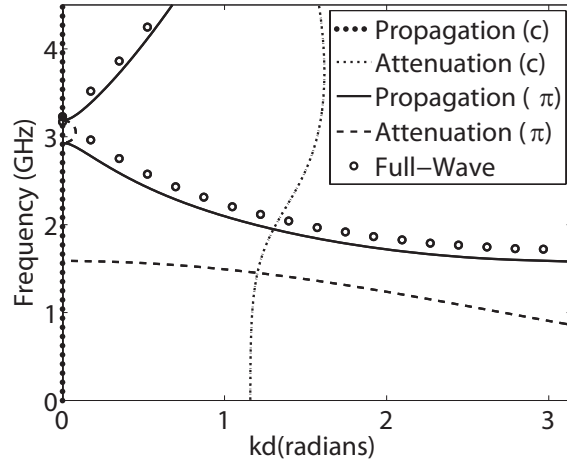
Figure 2.13: Dispersion diagrams of the NRI medium as calculated by MTL analysis and full-wave simulation (HFSS).

2.3.1.2 Negative Permeability Medium

The dispersion diagram of the negative permeability medium can also be calculated using MTL analysis. By setting the value of $L_w = \infty$, the effect of the central wire is removed from the third transfer matrix shown in Fig. 2.12(b). The resulting unit cell transfer matrix is that of the transmission-line cage medium.

The propagation and attenuation constants for both the c- and π-modes are plotted for the transmission-line cage unit cell in Fig. 2.14. These curves quantitatively show the contra-directional coupling that was qualitatively described in section 2.1.2.2. For frequencies below 1.82GHz, the c- and π-modes are separate. Over this frequency range, the c-mode corresponds closely to the parallel plate waveguide mode, exhibiting forward-wave propagation. The π-mode on the other hand is similar to

32

the backward-wave transmission-line mode. It is in cutoff until a resonant frequency (1.58GHz), at which point its propagation constant displays a negative slope with respect to frequency. At 1.82GHz the propagation constants of the two modes meet and a significant change is observed in the dispersion diagram. The propagation constants of both modes become complex, such that the imaginary parts of the two modes are identical while the real parts are equal in magnitude but opposite in sign. These complex propagation constants indicate that as one mode travels through the medium, it couples power into the other mode. This contra-directional coupling persists over nearly the same frequency range for which a stopband is observed in Fig. 2.4, with the upper limit of the stopband occurring at 3.2GHz. At higher frequencies, the c-mode is in cutoff, and the π-mode exhibits dispersion characteristics similar to that of a waveguide above cutoff or a periodic wire medium above its plasma frequency. Similar behavior is also observed for the NRI medium (see Fig. 2.13) over this frequency range.
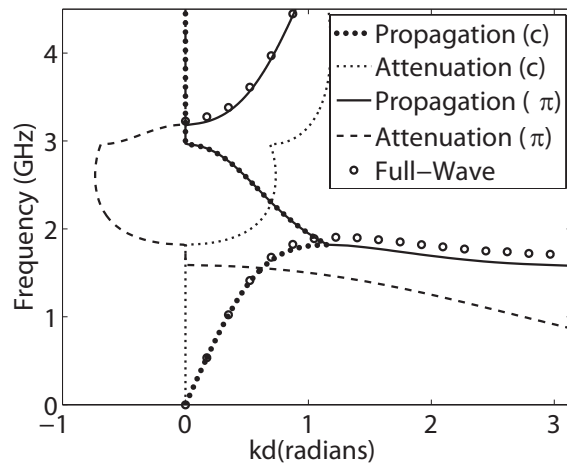
Figure 2.14: Dispersion diagrams of the NRI medium as calculated by MTL analysis and full-wave simulation (HFSS).

33

2.3.2 Finite Structures

The previous analysis dealt with finding the propagation characteristics of the infinite NRI or negative permeability medium, however, in practice, all structures are finite. Consequently, MTL analysis will be most useful if it can predict the behavior of finite structures as well. This can be accomplished by again using the transfer matrices of the complete unit cell defined in Fig. 2.12. For a slab that is n unit cells thick, the transfer matrix of a single unit cell should be raised to the nth power to find the transfer matrix for the entire finite slab. This final matrix is a 4×4 matrix of the form:

$$
\begin{bmatrix} V_1(\ell) \\ V_2(\ell) \\ I_1(\ell) \\ I_2(\ell) \end{bmatrix} = \begin{bmatrix} a_{11} & a_{12} & b_{11} & b_{12} \\ a_{21} & a_{22} & b_{21} & b_{22} \\ c_{11} & c_{12} & d_{11} & d_{12} \\ c_{21} & c_{22} & d_{21} & d_{22} \end{bmatrix} \begin{bmatrix} V_1(0) \\ V_2(0) \\ I_1(0) \\ I_2(0) \end{bmatrix}.
\tag{2.17}
$$

The reflection and transmission coefficients for a slab of the NRI medium are typically found for a free-space wave normally-incident on the structure. Recalling that the parallel plate waveguide represents free space propagation, this scenario can be modeled by connecting ports to the terminals of conductor 1 and terminating conductor 2 with an impedance that appropriately represents the physical situation. For example, if conductor 2 ends in an open circuit, the impedance applied to that terminal would be infinity, whereas if the conductor ends in a short circuit, the impedance would be zero. These terminations convert the four-port MTL structure shown in Fig. 2.15(a) into the two-port network shown in Fig. 2.15(b).

To express this simplification mathematically, the transfer matrix (Eq. 2.17) should no longer depend on the voltage and currents on conductor 2 (V_2 and I_2). Applying Kirchhoff's voltage laws at each of the terminations gives the relationships

between V_2 and I_2 at both of those locations:

$$V_2(0) = Z_L \cdot I_2(0) \tag{2.18a}$$

$$V_2(\ell) = -Z_L \cdot I_2(\ell) \tag{2.18b}$$

where Z_L is the impedance used to terminate conductor 2 at each end of the NRI slab. By using a variable for the termination impedance, this method remains valid for any symmetric 4-port structure. Further, this method can model the fringe capacitance in the case of an open circuit or the via inductance in the case of a short circuit. Eqs. (2.18a) and (2.18b) are used as boundary conditions to reduce the 4×4 transfer matrix of Eq. (2.17) to the 2×2 matrix

$$\begin{bmatrix} V_1(\ell) \\ I_1(\ell) \end{bmatrix} = \begin{bmatrix} \mathscr{A} & \mathscr{B} \\ \mathscr{C} & \mathscr{D} \end{bmatrix} \begin{bmatrix} V_1(0) \\ I_1(0) \end{bmatrix}, \tag{2.19}$$

where

$$\mathscr{A} = a_{11} - \frac{(b_{12} - a_{12} \cdot Z_L)(a_{21} - c_{21} \cdot Z_L)}{b_{22} - (a_{22} + d_{22}) \cdot Z_L + c_{22} \cdot Z_L^2}, \tag{2.20}$$

$$\mathscr{B} = b_{11} - \frac{(b_{12} - a_{12} \cdot Z_L)(b_{21} - d_{21} \cdot Z_L)}{b_{22} - (a_{22} + d_{22}) \cdot Z_L + c_{22} \cdot Z_L^2}, \tag{2.21}$$

$$\mathscr{C} = c_{11} - \frac{(d_{12} - c_{12} \cdot Z_L)(a_{21} - c_{21} \cdot Z_L)}{b_{22} - (a_{22} + d_{22}) \cdot Z_L + c_{22} \cdot Z_L^2}, \tag{2.22}$$

$$\mathscr{D} = d_{11} - \frac{(d_{12} - c_{12} \cdot Z_L)(b_{21} - d_{21} \cdot Z_L)}{b_{22} - (a_{22} + d_{22}) \cdot Z_L + c_{22} \cdot Z_L^2}. \tag{2.23}$$

The finite structure considered here consists of four of the unit cells shown in Fig. 2.12, with the second conductor being terminated with an additional $2L$ inductor on either end of the slab. To account for this inductance, the termination impedance was defined as $Z_L = j\omega 2L$. To provide a direct comparison, the finite structure was also simulated in Ansoft's HFSS. The full-wave model was a four-cell-thick slab consisting
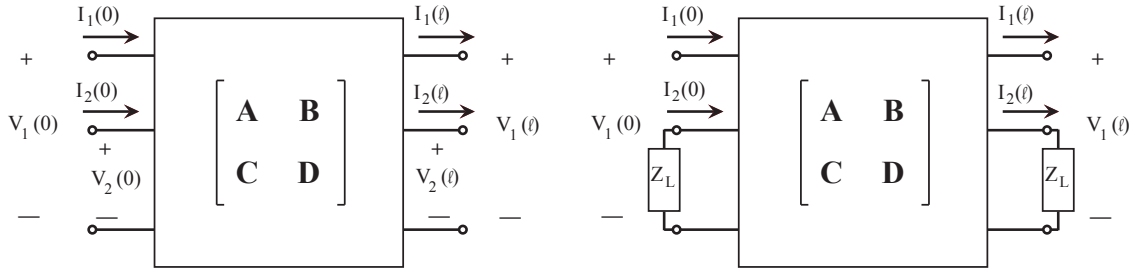
(a) Block diagram of the unterminated, finite MTL structure.

(b) Block diagram of the terminated, finite MTL structure.

Figure 2.15: Transformation of the four-port MTL system to a two-port system that can be excited by a plane wave in free space.

of the unit cells shown in Fig. 2.7. This structure shows the reason for the additional inductance used to terminate the second conductor in the MTL model. The metallic strips at the edge of the transmission-line cage were the same thickness as those in the middle of the slab. Since the metallic strips in the middle of the slab were modeled as the parallel combination of two $2L$ inductors, those at the edges of the slab needed to be as well. Perfect electric conductor boundary conditions were enforced on the top and bottom of each unit cell to achieve infinite periodicity in the vertical direction for the polarization of interest. Periodic boundary conditions with zero phase delay were applied to the sides of the four-cell slab to enforce infinite periodicity in the transverse direction. The reflection and transmission coefficients (equivalently, the scattering-parameters) of the four-cell slab were calculated for normal incidence and are compared with full-wave simulation results in Figures 2.16(a) and 2.16(b). Good agreement is shown, except for the low-frequencies where there is a slight frequency shift.

To provide further evidence that Eq. (2.19) is correct, the multiconductor circuit used in the MTL analysis was simulated using lumped element and transmission-line components in ADS. The S-parameters from this simulation agree exactly with those obtained through MTL analysis. With this confirmation, several explanations can

be given for the shift in the low-frequency values. The first is the extraction of the capacitance and inductance matrices of the host MTL transmission lines in the static limit. At low frequencies, the loading elements cause the phase delay across the unit cell to increase significantly, which alters the field distribution assumed in the static limit. The second explanation is the effect the finite size of the NRI slab had on the values of the constitutive parameters of the unit cell. Since the values of the loading elements and the host MTL transmission lines were extracted under the assumption of infinite periodicity, their values are slightly different at the boundaries of the slab.
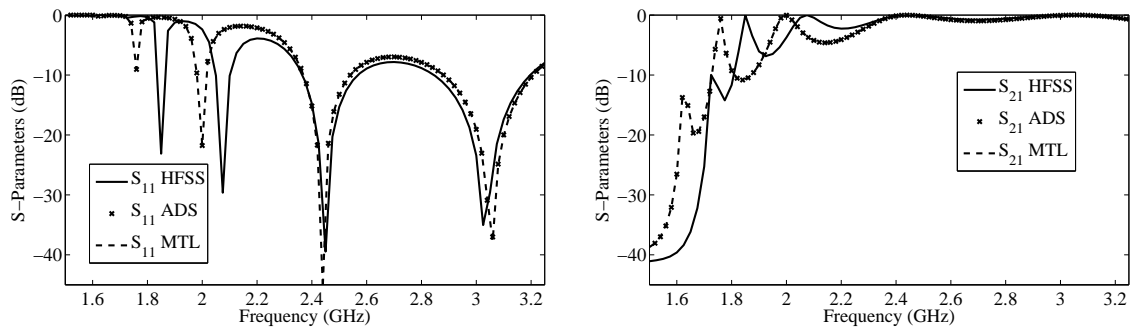
(a) Reflection coefficients calculated by full-wave analysis (HFSS), MTL analysis and a commercial circuit simulator (ADS).

(b) Transmission coefficients calculated by full-wave analysis (HFSS), MTL analysis and a commercial circuit simulator (ADS).

Figure 2.16: Scattering parameters of a four-cell NRI slab.

2.4   Homogenized MTL Analysis

Rigorous MTL analysis produces fast, accurate results, but it does not yield closed-form expressions nor much physical intuition beyond the circuit model itself. In order to derive simple intuitive equations that represent the NRI medium, the unit cell must be homogenized [34, 38]. To homogenize the unit cell, the transmission lines are broken down into their equivalent lumped components: inductors and capacitors. These lumped transmission-line components are simply the elements of the impedance and admittance matrices of the unloaded transmission lines. The transmission-line com-

ponents and the loading inductors and capacitors are then incorporated into a circuit model of the unit cell, as shown in Fig. 2.17. Because the unit cell is homogenized, the order of the elements is not important. For convenience, the elements of the NRI unit cell in Fig. 2.17 have been arranged in the form of a T-network.
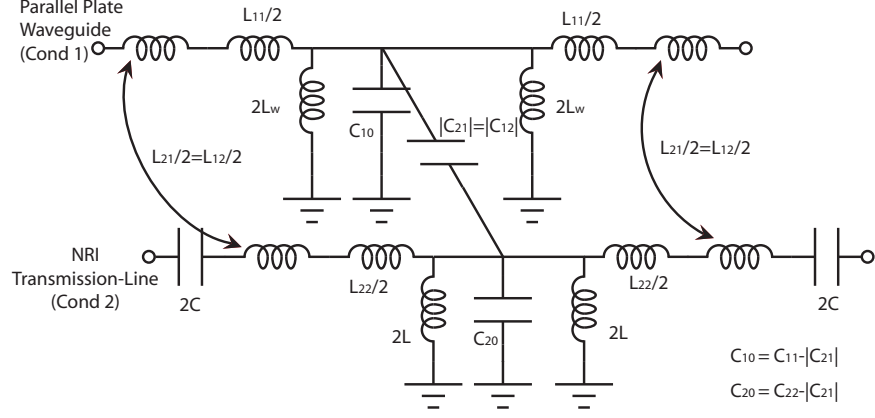
Figure 2.17: Circuit model of the NRI medium used for the homogenized MTL analysis.

After representing the unit cell as a T-network of lumped element components, the next step in the simplified MTL analysis is to solve for the homogenized impedance and admittance matrices. To find the impedance matrix, the impedance of the series loading element, C, is added to the impedance of the self-inductance on conductor 2 (L_{22}), effectively absorbing the lumped element into the transmission line. Similarly, to find the admittance matrix, the admittances of the shunt loading elements, L_w and L, are added to the admittances of the self-capacitances of conductor 1 (C_{11}) and conductor 2 (C_{22}), respectively. The resulting impedance and admittance matrices for the circuit in Fig. 2.17 are

$$
\begin{bmatrix} Z_{11} & Z_{21} \\ Z_{21} & Z_{22} \end{bmatrix} = j\omega \cdot \begin{bmatrix} L_{11}d & L_{21}d \\ L_{21}d & L_{22}d - \frac{1}{\omega^2 C} \end{bmatrix}
\tag{2.24a}
$$

$$
\begin{bmatrix} Y_{11} & Y_{21} \\ Y_{21} & Y_{22} \end{bmatrix} = j\omega \cdot \begin{bmatrix} C_{11}d - \frac{1}{\omega^2 L_w} & C_{21}d \\ C_{21}d & C_{22}d - \frac{1}{\omega^2 L} \end{bmatrix}.
\tag{2.24b}
$$

38
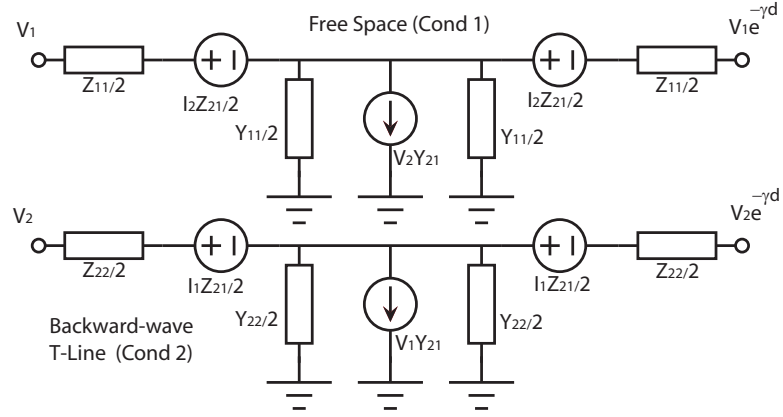
Figure 2.18: Schematic of the two-conductor MTL system for on-axis propagation in terms of impedance and admittance parameters.

The elements of the modified impedance and admittance matrices are subsequently used to form the homogenized circuit model of the unit cell, shown in Fig. 2.18. Note that reciprocity is assumed in the circuit model as well as in Eqs. (2.24a) and (2.24b).

Typically, absorbing the loading elements into the impedance and admittance matrices of the transmission lines would neglect the effect of spatial dispersion caused by the periodic nature of the unit cell. However, the periodicity can be accounted for using the Floquet theorem, which states that the voltages and currents on each end of the unit cell only differ from each other by a complex constant, here defined as $e^{-\gamma d}$. The Floquet theorem is enforced as shown in the circuit diagram in Fig. 2.18. Therefore, this method remains valid for any phase difference across the unit cell as long as the lengths of the interconnecting transmission lines are electrically short ($<< \lambda$).

2.4.1 Dispersion Diagram

For the case of on-axis propagation, the dispersion equation can be derived from the circuit shown in Fig. 2.18 by solving for the complex propagation constant, γ.

Application of Kirchhoff's voltage law yields the following expressions:

$$V_1 - I_1\frac{Z_{11}}{2} - I_2\frac{Z_{21}}{2} - I_2 e^{-\gamma d}\frac{Z_{21}}{2} - I_1 e^{-\gamma d}\frac{Z_{11}}{2} - V_1 e^{-\gamma d} = 0 \qquad (2.25)$$

$$V_2 - I_2\frac{Z_{22}}{2} - I_1\frac{Z_{21}}{2} - I_1 e^{-\gamma d}\frac{Z_{21}}{2} - I_2 e^{-\gamma d}\frac{Z_{22}}{2} - V_2 e^{-\gamma d} = 0. \qquad (2.26)$$

Simplifying these equations yields

$$V_1 \left(1 - e^{-\gamma d}\right) = I_1\frac{Z_{11}}{2}\left(1 + e^{-\gamma d}\right) + I_2\frac{Z_{21}}{2}\left(1 + e^{-\gamma d}\right) \qquad (2.27)$$

$$V_2 \left(1 - e^{-\gamma d}\right) = I_1\frac{Z_{21}}{2}\left(1 + e^{-\gamma d}\right) + I_2\frac{Z_{22}}{2}\left(1 + e^{-\gamma d}\right). \qquad (2.28)$$

Euler's identity states that $1 - e^{-\gamma d} = 2\sinh\left(\frac{\gamma d}{2}\right)e^{-\gamma d/2}$ and $1 + e^{-\gamma d} = 2\cosh\left(\frac{\gamma d}{2}\right)e^{-\gamma d/2}$. Dividing each side of Eqs. (2.27) and (2.28) by $\cosh\left(\frac{\gamma d}{2}\right)e^{-\gamma d/2}$ and combining the equations into a single matrix expression yields the relationship between the voltages and currents in terms of the impedance matrix:

$$2 \cdot \frac{\sinh\left(\frac{\gamma d}{2}\right)}{\cosh\left(\frac{\gamma d}{2}\right)} \begin{bmatrix} V_1 \\ V_2 \end{bmatrix} = \begin{bmatrix} Z_{11} & Z_{21} \\ Z_{21} & Z_{22} \end{bmatrix} \begin{bmatrix} I_1 \\ I_2 \end{bmatrix}$$

$$2 \cdot \tanh\left(\frac{\gamma d}{2}\right) \begin{bmatrix} V_1 \\ V_2 \end{bmatrix} = \begin{bmatrix} Z_{11} & Z_{21} \\ Z_{21} & Z_{22} \end{bmatrix} \begin{bmatrix} I_1 \\ I_2 \end{bmatrix}. \qquad (2.29)$$

To find the relationship between the currents and voltages in terms of the admittance matrix, Kirchhoff's current law can be applied to the circuit:

$$I_1 \left(1 - e^{-\gamma d}\right) = \tilde{V}_1 Y_{11} - \tilde{V}_2 Y_{21} \qquad (2.30)$$

$$I_1 \left(1 - e^{-\gamma d}\right) = \tilde{V}_1 Y_{21} - \tilde{V}_2 Y_{22}., \qquad (2.31)$$

where $\tilde{V}_i$ is the voltage at the midpoint of the ith conductor. $\tilde{V}_i$ is not known for either conductor, but it can be found by applying Kirchhoff's voltage law to the circuit one

40

half at a time:

$$\tilde{V}_1 = V_1 + I_1 Z_{11}/2 + I_2 Z_{21}/2 \tag{2.32a}$$

$$V_1 = e^{\gamma d} \cdot \tilde{V}_1 - I_1 Z_{11}/2 - I_2 Z_{21}/2 \tag{2.32b}$$

$$V_2 = \tilde{V}_2 + I_1 Z_{21}/2 + I_2 Z_{22}/2 \tag{2.33a}$$

$$V_2 = e^{\gamma d} \cdot \tilde{V}_2 - I_1 Z_{21}/2 - I_2 Z_{22}/2. \tag{2.33b}$$

Solving for $\tilde{V}_i$ in Eqs. (2.32) and (2.33) yields

$$\tilde{V}_1 = \frac{V_1 e^{-\gamma d/2}}{\cosh \frac{\gamma d}{2}} \tag{2.34}$$

$$\tilde{V}_2 = \frac{V_2 e^{-\gamma d/2}}{\cosh \frac{\gamma d}{2}}. \tag{2.35}$$

Substituting Eqs. (2.34) and (2.35) into Eqs. (2.30) and (2.31), gives the desired matrix equation:

$$2\sinh\left(\frac{\gamma d}{2}\right)\cosh\left(\frac{\gamma d}{2}\right)\begin{bmatrix} I_1 \\ I_2 \end{bmatrix} = \begin{bmatrix} Y_{11} & Y_{21} \\ Y_{21} & Y_{22} \end{bmatrix}\begin{bmatrix} V_1 \\ V_2 \end{bmatrix}$$

$$\sinh\left(\gamma d\right)\begin{bmatrix} I_1 \\ I_2 \end{bmatrix} = \begin{bmatrix} Y_{11} & Y_{21} \\ Y_{21} & Y_{22} \end{bmatrix}\begin{bmatrix} V_1 \\ V_2 \end{bmatrix}. \tag{2.36}$$

Combining (2.29) and (2.36), the current elements can be eliminated resulting in a 2×2 homogeneous system of equations (an eigenvalue problem):

$$\begin{bmatrix} a_1 - 4\sinh^2\left(\frac{\gamma d}{2}\right) & b_1 \\ b_2 & a_2 - 4\sinh^2\left(\frac{\gamma d}{2}\right) \end{bmatrix}\begin{bmatrix} V_1 \\ V_2 \end{bmatrix} = \begin{bmatrix} 0 \\ 0 \end{bmatrix}, \tag{2.37}$$

41

where

$$a_1 = Z_{11}Y_{11} + Z_{21}Y_{21}, \qquad a_2 = Z_{22}Y_{22} + Z_{21}Y_{21},$$

$$b_1 = Z_{11}Y_{21} + Z_{21}Y_{22}, \qquad b_2 = Z_{22}Y_{21} + Z_{21}Y_{11}.$$

In order to find nontrivial solutions, the determinant of Eq. (2.37) must be set equal to zero. This determinant produces the dispersion equation for on-axis propagation:

$$4 \cdot \sinh^2\left(\frac{\gamma d}{2}\right) = \frac{a_1 + a_2 \pm \sqrt{(a_1 - a_2)^2 + 4b_1 b_2}}{2}. \qquad (2.38)$$

Applying this analysis in two directions gives the following two-dimensional dispersion equation:

$$4 \cdot \sinh^2\left(\frac{\gamma_x d}{2}\right) + 4 \cdot \sinh^2\left(\frac{\gamma_y d}{2}\right) = \qquad (2.39)$$

$$\frac{a_1 + a_2 \pm \sqrt{(a_1 - a_2)^2 + 4b_1 b_2}}{2},$$

where γ_x and γ_y are the propagation constants in the $\hat{x}$ or $\hat{y}$ direction.

As in the traditional MTL analysis discussed in section 2.3, the dispersion equations give two unique modes. Here, the c-mode corresponds to the plus sign in front of the radical and the π-mode to the minus sign. Both modes are plotted in Fig. 2.19, along with the dispersion curve generated from full-wave simulations for comparison. As shown in Fig. 2.19, the c-mode is in cutoff throughout the entire frequency range of interest, while the π-mode supports a backward wave. The two-dimensional dispersion diagram (described in Appendix A) for the π-mode generated using (2.39) is compared with full-wave analysis in Fig. 2.20.

MTL analysis can also be used to examine how the propagation constant of the NRI medium changes with direction. In [29], full-wave analysis showed that the
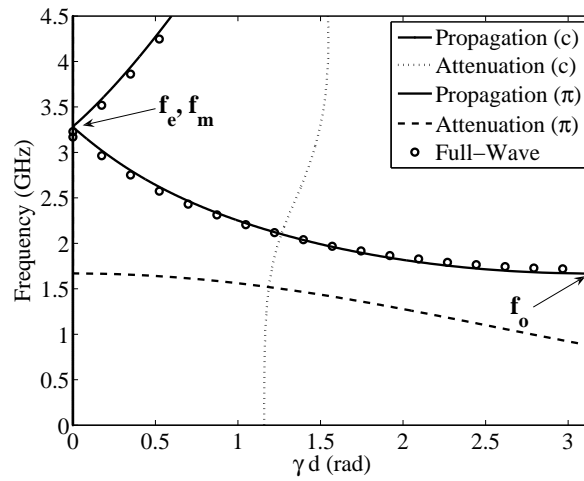
Figure 2.19: On-axis dispersion diagram. The π-mode corresponds to the backward-wave mode while the c-mode is in cutoff throughout the frequency range of interest.
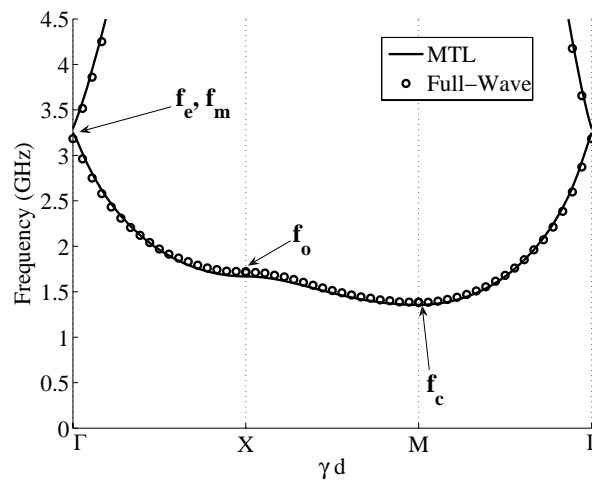
Figure 2.20: Two-dimensional dispersion diagram for the π-mode indicating the phase shifts $\Gamma = (0°, 0°)$, $X = (180°, 0°)$ and $M = (180°, 180°)$.

43

structure in Fig. 2.7 exhibited isotropic behavior (negligible spatial dispersion) when the phase difference across the unit cell was small. However, due to the amount of time required to perform the full-wave eigenmode simulations, only $k_x d \leq 40°$ and $k_y d \leq 40°$ were plotted. Using the two-dimensional dispersion Eq. (2.39), the isofrequency contours of the structure over the entire backward-wave band (shown in Fig. 3.15) can be calculated rapidly. Fig. 3.15 shows that the structure clearly exhibits isotropic propagation at high frequencies, however, at low frequencies the propagation constant changes significantly with direction due to spatial dispersion. This leads to the questions of how significant these deviations in propagation constant can be while still describing the propagation as "isotropic". Typically, this is influenced by the specific application, and the answer depends on the overall size of the material and the allowable deviation in phase over its extent. However, in discussing the properties of an infinite medium, a general condition should be given.

In [39], the representation of continuous media using two-dimensional grids of lumped elements is considered. Discretizing a continuous medium into such a grid network results in spatial dispersion. However, effective medium theory asserts that these lumped-element networks can be considered an accurate representation if the cell size is at most $d = \frac{\lambda}{10}$. The largest difference in propagation constant is between on-axis propagation and propagation 45° off-axis, as shown in Fig. 3.15. Expressions in [39] give the maximum percentage difference in propagation constant as 0.874% for a cell size of $d = \frac{\lambda}{10}$. By this stringent definition, the isotropic limit for this metamaterial occurs at a frequency of 2.52GHz. Frequencies below 2.52GHz will exhibit larger percentage differences in the propagation constant, however, as was mentioned earlier, the acceptable level of variation is dependent on the application.

This limit can also be obtained directly from Eq. (2.39). For convenience, the right hand side of the equation will be represented as $-\phi^2$. For on-axis propagation

(e.g. $\gamma_x = \gamma_{0°}$, $\gamma_y = 0$), Eq. (2.39) reduces to Eq. (2.38), now expressed as

$$4 \cdot \sinh^2 \left(\gamma_{0°} \frac{d}{2} \right) = -\phi^2. \tag{2.40}$$

For propagation 45° off-axis ($\gamma_x = \gamma_y = \gamma_{45°}/\sqrt{2}$), the dispersion equation can be written as

$$8 \cdot \sinh^2 \left(\frac{\gamma_{45°}}{\sqrt{2}} \frac{d}{2} \right) = -\phi^2. \tag{2.41}$$

Using Eqs. (2.40) and (2.41), the ratio of $\gamma_{45°}$ to $\gamma_{0°}$ is found in terms of ϕ as

$$\frac{\gamma_{45°}}{\gamma_{0°}} = \frac{\sinh^{-1} \left(\sqrt{\frac{-\phi^2}{4}} \right)}{\sqrt{2} \cdot \sinh^{-1} \left(\sqrt{\frac{-\phi^2}{8}} \right)}. \tag{2.42}$$

Thus, the value of ϕ determines the variation between on- and off-axis propagation.

In the limit where γd is small, Eq. (2.38) becomes

$$
\begin{aligned}
-\phi^2 &= 4 \cdot \sinh^2 \left(\frac{\gamma_x d}{2} \right) + 4 \cdot \sinh^2 \left(\frac{\gamma_y d}{2} \right) \\
&\approx 4 \cdot \left(\frac{\gamma_x d}{2} \right)^2 + 4 \cdot \left(\frac{\gamma_y d}{2} \right)^2 \\
&\approx (\gamma d)^2.
\end{aligned}
\tag{2.43}
$$

If $d = \frac{\lambda}{10}$ is again taken to be the maximum unit cell size for which propagation can still be assumed isotropic and given that $\gamma = j\frac{2\pi}{\lambda}$, the value of ϕ^2 at this limit becomes $\phi^2 = (\pi/5)^2 = 0.395$. Using this value in Eq. (2.42), results in

$$\frac{\gamma_{45°}}{\gamma_{0°}} = 1.0874. \tag{2.44}$$

In other words, the maximum percentage difference in propagation constant is 0.874%, the same as that obtained in [39].

45
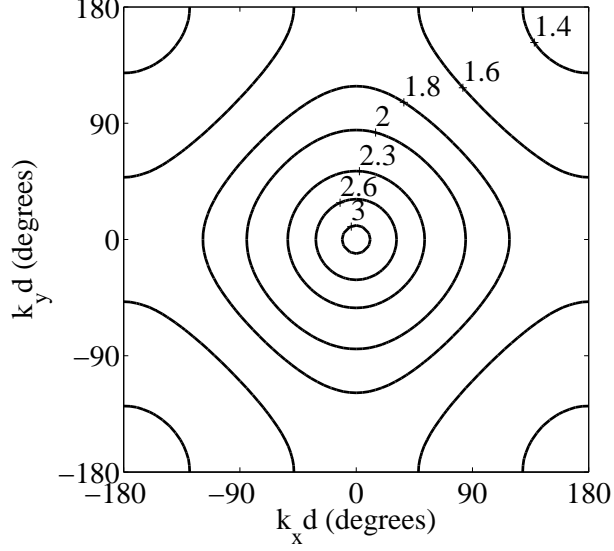
Figure 2.21: Isofrequency contour plot (in GHz) of the backward-wave mode with respect to two-dimensional propagation in the $\hat{x}$ and $\hat{y}$ directions.

2.4.2 Impedance and Material Parameters

The impedance of a two-conductor MTL structure is typically represented by $\mathbf{Z_0}$ (Eq. (2.14)): a 2×2 matrix relating the natural voltages to the natural currents on the two coupled lines [35]. Since the analysis in the previous section described the dispersion of the NRI medium in terms of the structure's c- and π-modes, it may be preferable to examine the modal impedances of the infinite NRI medium. These impedances can be found in a manner similar to that presented in [37]. Using Eq. (2.37), two expressions for the ratio of the voltages on conductor 1 and conductor 2 (R) can be found:

$$R = \frac{V_2}{V_1} = \frac{4\sinh^2\left(\frac{\gamma d}{2}\right) - a_1}{b_1} \tag{2.45}$$

or

$$R = \frac{V_2}{V_1} = \frac{b_2}{4\sinh^2\left(\frac{\gamma d}{2}\right) - a_2}. \tag{2.46}$$

46

Substituting either of these relationships into Eq. (2.29) allows the currents, I_1 and I_2, to be found in terms of either V_1 or V_2 rather than a combination of both. The impedances can then be found by taking the ratios of the voltage to the current on a given conductor, yielding the expressions

$$Z_1 = \frac{V_1}{I_1} = \frac{Z_{11}Z_{22} - Z_{21}^2}{2\tanh\left(\frac{\gamma d}{2}\right) \cdot (Z_{22} - Z_{21}R)} \tag{2.47}$$

$$Z_2 = \frac{V_2}{I_2} = \frac{(Z_{11}Z_{22} - Z_{21}^2)R}{2\tanh\left(\frac{\gamma d}{2}\right) \cdot (Z_{11}R - Z_{21})}. \tag{2.48}$$

These equations are valid for a single mode propagating in the direction determined by the Floquet propagation constant, γ. The mode is determined by the choice of $\gamma = \gamma_c$ or $\gamma = \gamma_\pi$. These impedance equations are only valid for an infinite medium. If the material is finite, then multiple modes would be required to satisfy the boundary conditions at the termination of the structure.

Despite not being strictly valid for finite slabs, the above impedance equations can still provide insight into the behavior of the NRI structure. Since Fig. 2.19 shows that the c-mode is in cutoff for all frequencies of interest, this mode can be ignored in an infinite medium. Additionally, conductor 1 represents a parallel plate waveguide, which models plane-wave propagation through the medium. Therefore, the transmission-line impedance of conductor 1 (Z_1) for the π-mode is proportional to the overall wave impedance of the infinite NRI medium. In order to find the exact expression for the wave impedance (which expresses the ratio of the electric field to the magnetic field, rather than the voltage to the current), the transmission-line impedance should be multiplied by the width-to-height ratio,

$$\eta_{1\pi} = Z_{1\pi} \cdot \frac{d}{h}. \tag{2.49}$$

The wave impedance for the infinite medium composed of the unit cells shown in
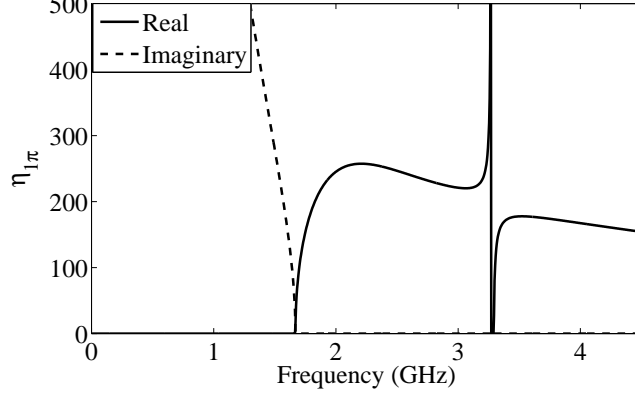
Figure 2.22: Wave impedance of the π-mode on conductor 1 for the volumetric NRI medium.

Fig. 2.7 is plotted in Fig. 2.22. The resonance that occurs around 3.28GHz is due to the fact that the plasma frequencies are not exactly the same, resulting in a small stopband between the electric and magnetic plasma frequencies. From this graph, it is clear that the electric plasma frequency occurs slightly before the magnetic plasma frequency since the impedance grows rapidly (indicating ϵ close to zero) before going to zero (indicating μ equal to zero). It should also be noted that the impedance of the infinite medium was not designed to match that of free-space. Instead the unit cell was modeled exactly as it was shown in Fig. 2.7. As described in [29], the values of the loading elements of Fig. 2.7 were selected to produce an impedance match at 2.45GHz for a four-cell slab, which is evident in Fig. 2.16(a).

In conventional materials, the wave impedance is equal to $\eta = \sqrt{\mu/\epsilon}$ and the propagation constant is equal to $\gamma = j\omega\sqrt{\mu\epsilon}$. By taking either the ratio or the product of these formulae and dividing by the radial frequency, ω, the permeability and permittivity for the infinite medium can be defined as

$$\mu_r = \frac{-j\gamma_\pi \eta_{\pi 1}}{\omega \mu_0} \tag{2.50}$$

$$\epsilon_r = \frac{-j\gamma_\pi}{\omega \eta_{\pi 1} \epsilon_0}. \tag{2.51}$$

48

However, to treat this metamaterial in the same way as conventional materials, it must behave like a homogeneous medium. This means that the propagation constant must not be distorted by spatial dispersion. As was discussed in section 2.4.1, homogeneous behavior is only possible when the phase difference across the unit cell is small. This restricts the frequency range over which effective material parameters can be defined. Under these conditions, the expressions for the material parameters can be simplified. If γd is assumed to be small in Eq. (2.47), then the expression simplifies to

$$Z_1 \approx \frac{1}{\gamma} \frac{Z_{11}Z_{22} - Z_{21}^2}{d \cdot (Z_{22} - Z_{21}R)}. \tag{2.52}$$

This equation is particularly useful for expressing μ_r because it depends inversely on γ. Therefore, by inserting Eq. (2.52) into Eq. (2.50), γ drops out of the expression, yielding

$$\mu_r \approx -j \frac{Z_{11}Z_{22} - Z_{21}^2}{\omega\mu_0 h \cdot (Z_{22} - Z_{21}R_\pi)}. \tag{2.53}$$

In the equation for ϵ_r, Z_1 having an inverse dependence on γ is not desirable because no cancelation would occur. This would instead result in the expression for ϵ_r being proportional to γ^2. To obtain a simpler expression, a different equation for Z_1 must be derived. Instead of using the ratio of the voltages on conductors 1 and 2, the ratio of the currents is used. This ratio, r, is defined as

$$r = \frac{I_2}{I_1} = \frac{4\sinh^2\left(\frac{\gamma d}{2}\right) - a_1}{b_2} \tag{2.54}$$

or

$$r = \frac{I_2}{I_1} = \frac{b_1}{4\sinh^2\left(\frac{\gamma d}{2}\right) - a_2}. \tag{2.55}$$

Inserting this relationship into Eq. (2.36), gives the following expression for the ratio

of V_1 to I_1:

$$Z_1 = \sinh{(\gamma d)} \frac{Y_{22} - Y_{21} r}{Y_{11} Y_{22} - Y_{21}^2} \tag{2.56}$$

$$\approx \gamma d \cdot \frac{Y_{22} - Y_{21} r}{Y_{11} Y_{22} - Y_{21}^2}, \tag{2.57}$$

as long as γd is small. In this new equation, Z_1 is now directly proportional to γ, which will result in γ dropping out of Eq. (2.51), yielding

$$\epsilon_r \approx -j \frac{Y_{11} Y_{22} - Y_{21}^2}{\omega \epsilon_0 \left(d^2/h \right) \cdot \left(Y_{22} - Y_{21} r_\pi \right)}. \tag{2.58}$$

The simplified expressions in Eqs. (2.53) and (2.58) provide physical insight into what determines the effective permeability and permittivity. Eq. (2.58) shows that the permittivity depends only on elements of the admittance matrix (with the exception of the current ratio, r), i.e. the shunt elements in the circuit diagram. This is expected since the unloaded admittance matrix consists of capacitive elements, whose values are directly related to the permittivity of the medium. Similarly, Eq. (2.53) depends only on elements of the impedance matrix (with the exception of the voltage ratio, R), which are the series elements of the circuit diagram. This is expected as well because the unloaded elements of the impedance matrix are inductances, which are dependent on the permeability of the medium.

The form of Eqs. (2.53) and (2.58) is also important. In both Eqs. (2.53) and (2.58), the zeros of the functions are isolated in their numerators. These zeros represent the magnetic and electric plasma frequencies, respectively. Using Eq. (2.53) and the constituents of the homogenized impedance matrix in Eq. (2.24a), the magnetic plasma frequency is found to be

$$\omega_m = \sqrt{\frac{1}{L_{11} L_{22} - L_{21}^2} \frac{L_{11}}{Cd}}. \tag{2.59}$$

In the case of the electric plasma frequency, the numerator of Eq. (2.58) has two zeros. However, one occurs at a frequency well-above the range of interest. Ignoring this zero, the electric plasma frequency is given by the expression

$$\omega_e = \frac{1}{\sqrt{2 \cdot (C_{11}C_{22} - C_{21}^2)}} \cdot \frac{}{\sqrt{\left(\frac{C_{11}}{Ld} + \frac{C_{22}}{L_w d} - \sqrt{\left(\frac{C_{11}}{Ld} - \frac{C_{22}}{L_w d} \right)^2 - \frac{4C_{21}^2}{Ld L_w d}} \right)}}. \tag{2.60}$$

Both of the plasma frequencies will be discussed further in the following section.

The relative permittivity and permeability of the infinite medium are shown in Fig. 2.23. Both the approximate (Eqs. (2.53) and (2.58)) and the exact (Eqs. (2.50) and (2.51)) curves are plotted, but it should be emphasized that neither expressions are valid when the medium exhibits spatial dispersion. As mentioned in the previous section, the effective medium approximation is only valid when γd is small. Even the exact expressions are limited by this condition. Since γd being small was the only assumption made to obtain the approximate expressions, the material parameters are valid when the approximate and exact curves overlap. When the curves diverge, this indicates that it is no longer appropriate to define effective permittivity and permeability.

2.4.3 Resonances

In NRI media, three important frequencies can be used to characterize the dispersion curve: the electric and magnetic plasma frequencies and the low-frequency backward-wave cutoff. The first two were introduced in the previous section, and both correspond to the propagation constant being equal to zero, while the third corresponds to the frequency at which the phase difference across the unit cell is 180°.
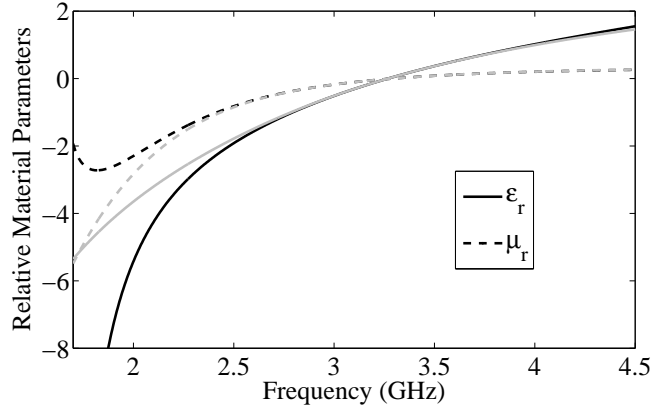
Figure 2.23: Material parameters for the volumetric NRI medium. The black lines correspond to the exact solutions given by Eqs. (2.50) and (2.51). The gray lines correspond to the approximate solutions given by Eqs. (2.53) and (2.58).

In addition to deriving the plasma frequency equations (Eqs. (2.59) and (2.60)) from the relative permeability and permittivity expressions, they can also be obtained from physical arguments combined with circuit analysis. The series inductors of an unloaded MTL system govern its magnetic response, and consequently, its permeability response. Altering the effective inductance of the transmission lines will affect the permeability of the medium. The effective inductance of a MTL system can be changed by the addition of a reactive series element. In Fig. 2.17, the effective inductance of the MTL system is changed by adding the series capacitor, C. This results in a negative effective permeability for some frequencies, as shown in Fig. 2.23. At the magnetic plasma frequency, ω_m, the inductive elements of the unloaded MTL system resonate with the loading capacitor such that the effective permeability is zero. When this occurs, the middle and both ends of the unit cell appear to be shorted to ground, as depicted in Fig. 2.24. This short-circuits the shunt elements, leaving only the series elements, as shown in Fig. 2.25. The effective permeability goes to zero when the series-only impedance of conductor 1 goes to zero. The series-only impedance of conductor 1, which accounts for the elements of conductor 2 through the mutual

52
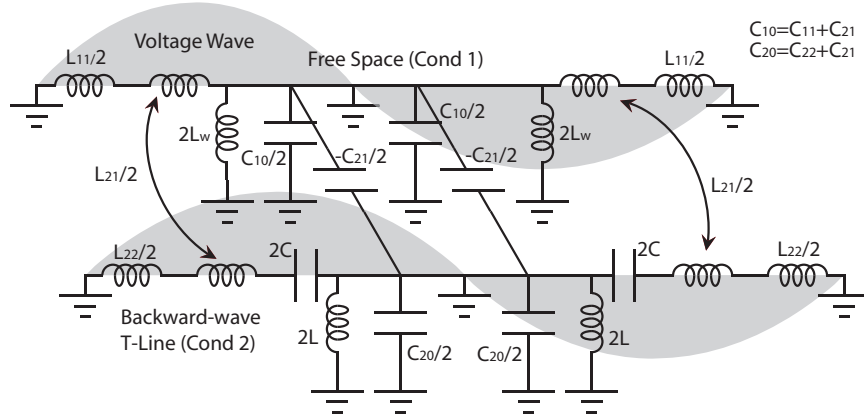
Figure 2.24: Schematic showing the magnetic plasma frequency resonance on the MTL system for on-axis propagation.
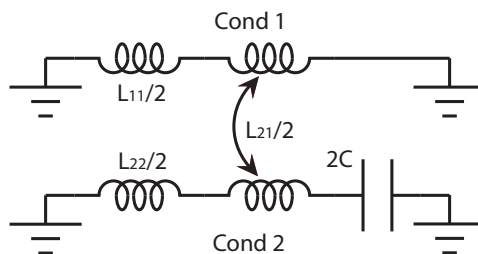
Figure 2.25: The left half of the circuit shown in Fig. 2.24 after being simplified due to the shorting of the shunt elements.

inductance, L_{21}, is given by

$$Z_{series1} = j\omega L_{11}d - \frac{(j\omega L_{21}d)^2}{j\omega L_{22}d - \frac{1}{j\omega C}}. \tag{2.61}$$

Setting Eq. (2.61) equal to zero and solving for ω yields the same expression for ω_m as Eq. (2.59).

A similar analysis can be applied to find the electric plasma frequency, ω_e. In the unloaded MTL system, the shunt capacitors are responsible for determining the electric response, and therefore, the permittivity of the medium. Again, reactive loading elements, such as L_w and L, are placed in shunt to change the effective capacitance and, consequently, the effective permittivity. Fig. 2.23 shows that the introduction of these loading elements creates a negative permittivity over certain
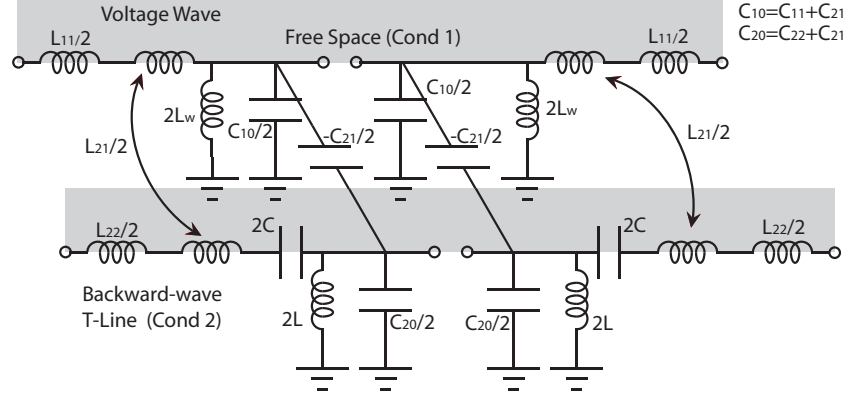
Figure 2.26: Schematic showing the electric plasma frequency resonance on the MTL system for on-axis propagation.

frequencies. At the electric plasma frequency, ω_e, the capacitive elements of the unloaded MTL system will resonate with the loading shunt inductors such that the effective permittivity is zero. In this case, the middle and both ends of the unit cell appear as open circuits (shown in Fig. 2.26), thereby eliminating the effects of the series elements. Without the series elements, the circuit appears as shown in Fig. 2.27. The effective permittivity goes to zero when the shunt-only impedance of conductor 1 to ground goes to infinity. The shunt-only impedance of conductor 1 to ground is given by the expression

$$Z_{shunt1} = \frac{-j\omega C_{22}}{\left(C_{11}C_{22} - C_{21}^2\right)d}. \tag{2.62}$$

$$\frac{\omega^2 - \frac{1}{LC_{22}d}}{\omega^4 - \frac{\omega^2}{\left(C_{11}C_{22}-C_{21}^2\right)d}\left(\frac{C_{11}}{L} + \frac{C_{22}}{L_w}\right) - \frac{1}{\left(C_{11}C_{22}-C_{21}^2\right)^2d^2}\frac{1}{L_wL}}.$$

By setting the denominator equal to zero and solving for ω, two solutions are found, one of which is exactly the same as the expression for ω_e given by Eq. (2.60). The second solution corresponds to a resonance for the c-mode, which occurs at a frequency well above those of interest.

The equation for the low-frequency backward-wave cutoff for on-axis propagation
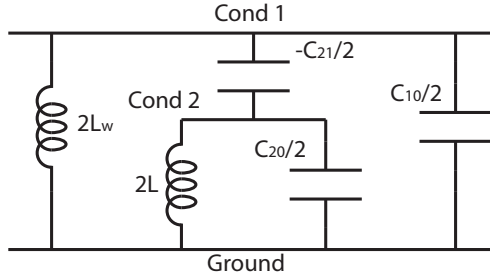
Figure 2.27: The left half of the circuit shown in Fig. 2.26 after being simplified due to the elimination of the series elements.

is found by setting $\gamma d = 180°$ in Eq. (2.38), which is the "X" point on the dispersion diagram in Fig. 2.20. For this resonant condition, each end of the unit cell is shorted to ground, as shown in Fig. 2.28. Unfortunately, this results in a complicated expression with multiple solutions. Noting that the desired condition describes the lowest frequency in the backward-wave band, higher order frequency terms can be ignored, giving the following approximation

$$\omega_o \approx \sqrt{\frac{1}{4LC + LC_{22}d - CL_{22}d}}. \tag{2.63}$$

It is interesting to note that this is the exact expression for the low-frequency cutoff of the backward-wave transmission line (conductor 2) in isolation. This result indicates that the coupling between conductor 1 and conductor 2 is insignificant near this cutoff frequency.

Off-axis propagation can support propagation at even lower frequencies. The two-dimensional low-frequency backward-wave cutoff can be found by simply setting $\gamma_x d = 180°$ and $\gamma_y d = 180°$ in Eq. (2.39), which is the "M" point of the dispersion diagram in Fig. 2.20. After applying the same approximations as were used to obtain Eq. (2.63) for the case of on-axis propagation, the equation for the two-dimensional
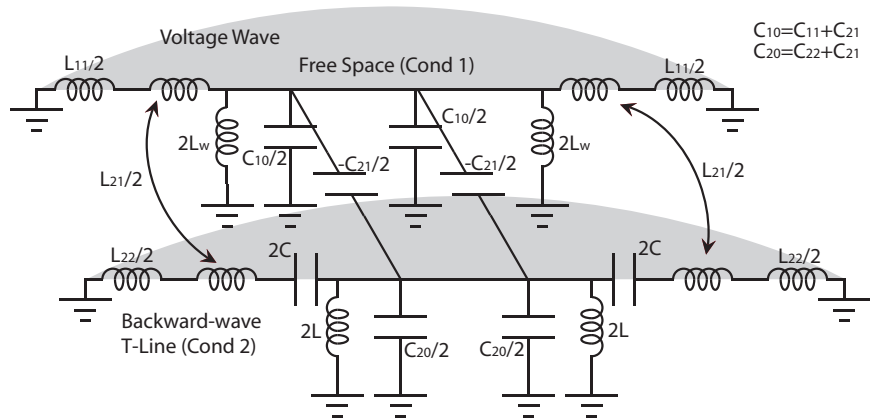
Figure 2.28: Schematic showing the low-frequency backward-wave cutoff resonance on the MTL system for one-dimensional propagation.

low-frequency cutoff is given by

$$\omega_c \approx \sqrt{\frac{1}{8LC + LC_{22}d - CL_{22}d}}.$$ (2.64)

CHAPTER III

The Experimental Realization of Broadband NRI Media

The multiconductor transmission-line (MTL) analysis described in the previous section provided theoretical evidence that negative-refractive-index (NRI) metamaterials could indeed exhibit a broad backward-wave bandwidth. The next step was to verify this claim experimentally through the physical realization of a broadband NRI lens [12]. In order to achieve sub-wavelength focusing in free-space, the NRI medium must be low loss and have a relative permittivity and permeability (ϵ_r and μ_r) close to -1. As mentioned earlier, impedance mismatches and high loss prevented previous volumetric NRI lenses from achieving super resolution [40, 41, 42, 43]. In this chapter, these issues are mitigated sufficiently such that the lenses presented here demonstrate resolution beyond the diffraction limit.

3.1 The First Experimental Broadband NRI Lens

The first broadband NRI lens to be fabricated adhered as closely to the design presented in Chapter II (Fig. 2.7) as possible. One unit cell of the experimental NRI medium is shown in Fig. 3.1 [44]. One slight difference between the original design shown in Fig. 2.7 and the one depicted in Fig. 3.1 was the inclusion of RO4003

circuit boards to provide a substrate for the capacitive grid. A second modification was that the inductively loaded central strip was replaced with a thin wire. There were three reasons for this change. First, the requisite inductance could be achieved using commercially available wires, so there was no need for the added complexity of lumped inductors. Secondly, the wires displayed a superior quality factor compared to commercial chip inductors. Finally, metallic strips would need to be printed on microwave substrates like the capacitive grids, and the presence of the dielectric would introduce a slight asymmetry to the unit cell.
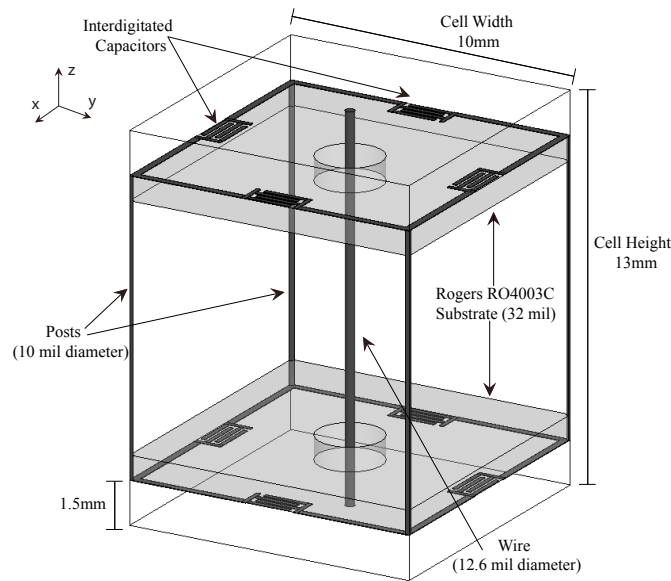
Figure 3.1: One unit cell of the physically-realizable broadband NRI medium.

3.1.1 Design of the Broadband NRI Lens

According to simulations performed in [29], a slab thickness of four unit cells was sufficient to realize the broad bandwidth achieved through the traveling-wave nature of the transmission-line cage. As a result, a four-cell slab of this structure was designed to have effective material parameters of $\epsilon_r \approx -1$ and $\mu_r \approx -1$ at the design frequency of 2.45GHz. The simulated scattering parameters of this four-cell slab were obtained using Ansoft's HFSS and are plotted in Fig. 3.2. All simulations

were performed with conductors as the boundaries on the top and bottom of the unit cell. This ensured that the electric field was always polarized in vertical direction and more accurately represented the experiments described in section 3.1.3.
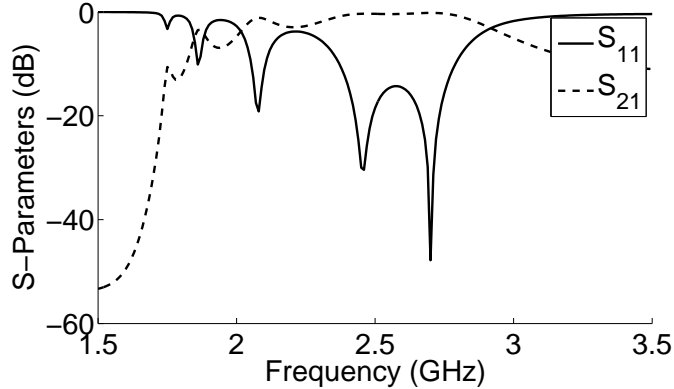
Figure 3.2: Simulated S-parameters of a four-cell thick slab of NRI metamaterial contained within a parallel plate waveguide.

The effective material parameters were extracted from the simulated S-parameters. To tune the permittivity of the medium, the diameters of the both the central wire and the posts of the transmission-line cage (see Fig. 3.1) were varied. The length of the interdigital fingers of the capacitors were changed in order to realize the desired effective permeability. After optimization, the effective material parameters of the simulated structure were $\epsilon_r = -0.99 + j0.011$ and $\mu_r = -1.02 - j0.054$ at the design frequency. Equivalently, the refractive index and wave impedance were found to be $n = -1.01 - j0.021$ and $\eta_{Bloch} = 384 + j12\Omega$. Since η_{Bloch} was close to the free-space wave impedance of 377Ω, the structure was well matched to free-space at 2.45GHz, a fact that is confirmed by Fig. 3.2. It should be noted, that for the time-harmonic progression of $e^{j\omega t}$ used throughout this thesis, the imaginary part of the index of refraction should be negative in passive media, as calculated above. This may make the positive imaginary part of ϵ_r appear unphysical, however this is not the case. The method of extraction used to obtain the material parameters is similar to those used for natural materials (e.g. [45]). However, the equation used to

calculate the wave impedance approaches a singularity when the electrical length of the NRI slab is a multiple of $\frac{\lambda}{2}$ [46], which compromises the accuracy of the extracted material parameters. This phenomenon has recently been analyzed in detail [47] and is attributed to weak spatial dispersion that is neglected in the equations for natural materials. Nevertheless, if one considers the index of refraction, n, the imaginary part is consistent with a passive medium. This method is more reliable because extracted value of n does not depend on the wave impedance. The passive nature of the broadband NRI medium is further verified by Fig. 3.3, which shows that the loss is positive for all frequencies.

The simulated value for n gave an attenuation constant of $\alpha = 1.08\text{Np/m}$ and a propagation constant of $\beta = 51.6\text{rad/m}$ at 2.45GHz. A metric commonly used to quantify the loss in NRI media is the figure of merit (FOM) [48, 49]. It is defined as

$$FOM = \left|\frac{n'}{n''}\right| = \left|\frac{\beta}{\alpha}\right| \tag{3.1}$$

where n' and n'' are the real and imaginary parts of the refractive index, respectively. For this structure the figure of merit was calculated to be $FOM = 47.9$ at the design frequency. For comparison, the planar NRI transmission-line medium used to verify super resolution in [50] had a figure of merit of $FOM = 32.14$. The figure of merit of the broadband NRI medium exceeds that observed in the NRI transmission-line medium predominantly because the wire used to achieve negative permittivity has a higher Q than the lumped element inductors used to load the NRI transmission lines.

The dispersion curve of the optimized NRI unit cell (plotted in Fig. 3.4) indicates that it exhibits a backward-wave bandwidth of 44.3%: ranging from 1.83GHz to 2.86GHz. Due to the wide frequency range over which the index of refraction is negative, the operating frequency of 2.45GHz is no longer close to the low-frequency resonance of 1.83GHz (where the permeability changes from highly-positive to highly-

negative values) as is the case for the split-ring resonator (SRR)/wire medium. The losses are lower the further the operating frequency is from this resonance [8], as is evident in Fig. 3.3. The power lost due to conductor and dielectric losses is 0.37dB at 2.45GHz for the entire four-cell slab or 0.092dB/cell (equivalently 0.092dB/cm), demonstrating that this NRI structure has minimal power loss at the operating frequency.
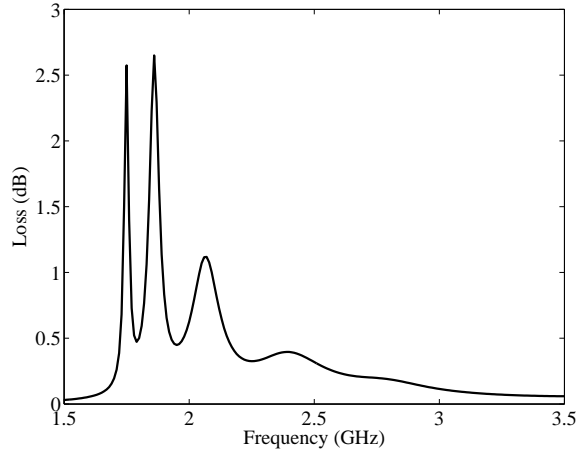
Figure 3.3: Simulated conductor and dielectric losses for a four-cell slab given by $Loss(dB) = -20\log\left(\sqrt{|S_{11}|^2 + |S_{21}|^2}\right)$. The four peaks in loss occur when the four-cell slab is at resonant lengths of 180°, 360°, 540° and 720°.
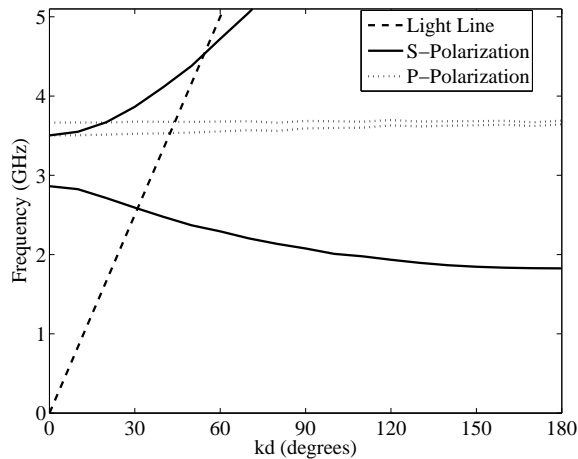
Figure 3.4: Simulated dispersion curve of the infinite NRI medium shown in Fig. 3.1.

3.1.2 Fabrication

The broadband NRI lens was fabricated by first constructing the transmission-line cage to serve as the negative permeability medium then adding the central wires to introduce negative permittivity. The first step in fabricating the transmission-line cage was to print a capacitively loaded grid onto two 32mil (0.81mm) RO4003 substrates ($\epsilon_r = 3.38$), as shown in Fig. 3.5. The unit cell size of the grid was 1cm in both of the horizontal directions. The capacitors were interdigital, printed capacitors optimized through simulation to have a value of 322fF. Small holes were drilled at the grid junctions and plated with copper to accommodate the wire posts that served as the inductors of the NRI transmission-line grid. The capacitively loaded grids were then spaced 1cm apart and the posts, made from copper wire with a 10 mil (254μm) diameter, were soldered between them. The negative permeability slab was four cells thick and had a width of 15 cells ($1.225\lambda_0$ at the design frequency). To emulate infinite periodicity in the vertical direction, the slab was placed between two parallel plates, spaced 1.3cm apart. Foam blocks were cut to support the transmission-line cage structure, ensuring a 1.5mm separation between the parallel plates and the RO4003 substrates.

Once the negative permeability medium was fabricated, making a NRI medium was only a matter of adding wires to achieve negative permittivity. The holes in the center of the negative permeability unit cell (2.25mm in diameter) allowed these wires to pass through. These holes are depicted in the unit cell enlargement in Fig. 3.5. Copper-clad RO4003 substrates were used as the parallel plates. Copper-plated holes were drilled into these ground planes to allow for proper grounding of the negative permittivity wires. The wires were 12.6mil (0.32mm) in diameter and 1.3cm in length. They were soldered between the top and bottom parallel plates to create the NRI lens, which was also four cells thick with a width of 15 cells. A photograph of the NRI lens within the parallel plate waveguide is shown in Fig. 3.6.
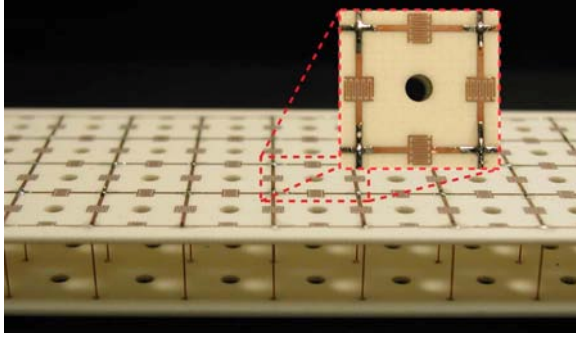
Figure 3.5: Picture of the negative permeability slab with an enlargement of a capacitively-loaded grid unit cell.
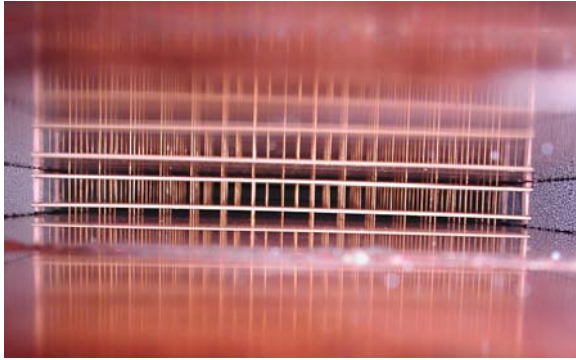
Figure 3.6: Photograph of the NRI lens inside the parallel plate waveguide.

3.1.3 Experiments

All the experiments for the negative permeability and NRI media were conducted in a parallel plate waveguide (PPW) environment. Gradient absorber FL-4500CL, manufactured by ETS-Lindgren, was used to prevent reflections from the edge of the PPW, similar to that described in [51]. While Justice et. al. used wedge-shaped absorber, the resonant frequency of 1.82GHz and the size of the plates (45.7-by-61.0 cm) did not permit wedges of sufficient size to fully attenuate the low frequency radiation. Nevertheless, tests confirmed that the gradient absorber successfully eliminated the reflections from the edges of the PPW. The absorber was cut into 1.3cm slabs (to ensure the correct unit cell height) and arranged in a rectangle around the lens, as shown in Fig. 3.7. Also pictured in Fig. 3.7 are the Amphenol Connex 132147 coaxial connectors, which were used as probes to provide the fixed-point excitations

inside the PPW. The dielectric jackets covering the connectors were trimmed such that only the center conductor protruded from the surface of the plates.
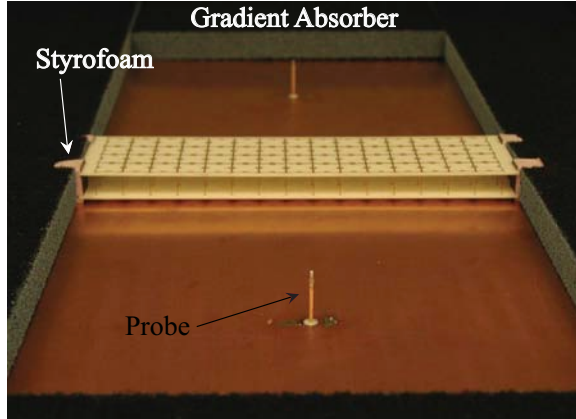
Figure 3.7: Photograph of the bottom plate of the parallel-plate waveguide with gradient absorber walls and the negative permeability slab. This photograph shows the two-probe experimental setup used to measure the stopband characteristics of the negative permeability medium. The probes have been placed 7cm from the cell so that only the transmission of the propagating waves is considered.

3.1.3.1 Negative Permeability Stopband Measurements

When the permeability and permittivity of a medium have opposite signs, waves attenuate exponentially as they travel through the medium. The negative permeability medium, therefore, exhibits a stopband over the region where negative permeability occurs, as discussed in section 2.1.2.2. For the fabricated negative permeability metamaterial, this stopband is shown by the dispersion curve in Fig. 3.8. While the dispersion curve could not be measured directly from experiments, the negative permeability medium was tested to verify its attenuation characteristics. This was done by placing two sources (coaxial connector probes) 7cm (0.57λ) away from either face of the slab (see Fig. 3.7). This distance placed the air/slab interfaces beyond the reactive near-field of the probes and into the Fresnel region. This ensured that all of the evanescent fields emanating from the probes would attenuate sufficiently before reaching the slab, eliminating the possibility of evanescent field recovery. This was

important for stopband measurements because any evanescent waves that reached the first slab interface could be resonantly amplified, producing enhanced fields at the receiving probe. Further, because the distance from the source to the slab was greater than the thickness of the slab, no internal nor external focusing of the evanescent spectrum could occur. The transmission between the two probes was measured, and both the simulated and experimental results are displayed in Fig. 3.9. The plot shows total attenuation better than 20dB for the measured four-cell slab with respect to the parallel plate environment without the slab present. At the design frequency of 2.45GHz, the slab corresponds to an electrical thickness of just less than $\frac{\lambda_0}{3}$. Therefore, the negative permeability slab acts as a highly-attenuating stopband medium.
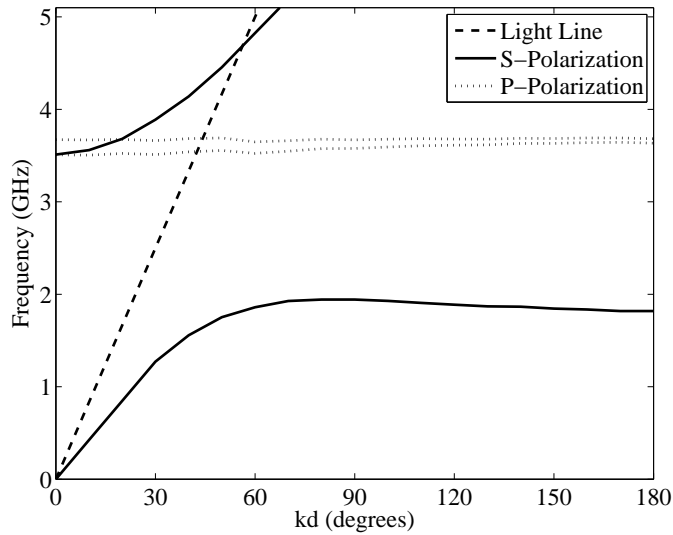
Figure 3.8: Simulated dispersion curve of the infinite negative permeability medium.

The exact frequencies over which the medium exhibits a stopband (a negative permeability) cannot be accurately determined from Fig. 3.9, since the impedance, index of refraction and attenuation constant of the slab all play an important role in determining the magnitude of S_{21}. In contrast, the stopband edges are clearly defined in Fig. 3.8, which shows the propagating eigenmodes of the negative permeability medium. This is because the eigenmode analysis assumes infinite periodicity, and,
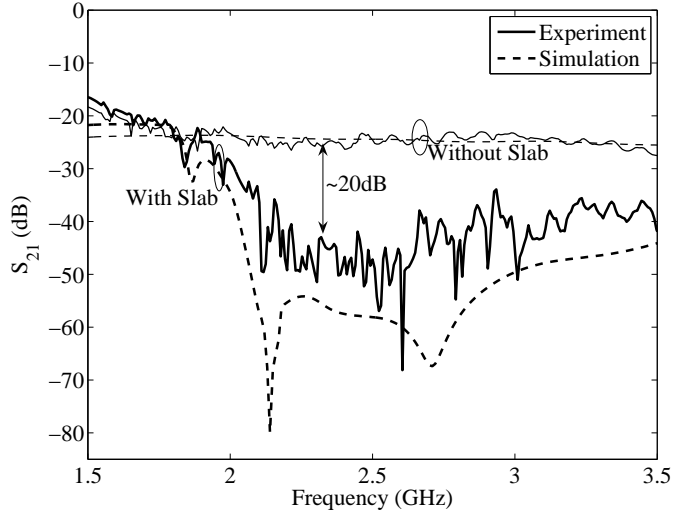
Figure 3.9: Stopband performance of the negative permeability slab shown in Fig. 3.5. Measurements are denoted by the solid line and simulated results are shown with the dashed line. The darker lines denote the transmission coefficients when the slab is present, while the lighter lines denote the transmission coefficients when the slab is removed.

therefore, even the slightest attenuation constant results in a stopband. In a finite structure, such as the one shown in Fig. 3.7, the small attenuation constants near the stopband edges do not significantly affect the transmission through the slab. Therefore, one cannot say with exact certainty where the stopband begins and ends based only on the transmission data.

Given the knowledge of the high- and low-frequency edges of the stopband from Fig. 3.8, both the simulated and experimental data plotted in Fig. 3.9 show counterintuitive behavior at the edges of the stopband. At the low-frequency end, the magnitude of S_{21} is nearly the same with the transmission-line cage as without it. On the other hand, at the high-frequency edge, the transmission-line cage provides more than 10dB of attenuation. The difference in transmission magnitude at these two frequencies is not a result of attenuation within the negative permeability medium. Instead, it is an effect of the experimental setup and the specific material parameters at each frequency.

Similar to arrays of split-ring resonators, the broadband negative permeability

slab exhibits a high, positive permeability at frequencies just below the low-frequency stopband edge. In this same frequency range, the electrical loading caused by the slab also increases the permittivity. Together, these two effects increase the positive index of refraction of the medium while maintaining a wave impedance that is similar to that of free space. Consequently, the slab remains reasonably well-matched to free space and refracts the cylindrical wave emanating from the transmitting probe toward the slab's normal, increasing the power density at the receiving probe. This explains why both the measured and simulated magnitudes of S_{21} are greater with the slab than without it at frequencies below the stopband.

At frequencies above the high-frequency edge of the stopband, the magnitude of S_{21} remains low due to the reflections from the slab. As the permeability transitions from negative to positive, it remains much lower than that of free space. Since the permittivity of the medium is still high due to the electrical loading caused by the slab, the slab exhibits a low impedance and reflects much of the power incident on it. Furthermore, the low index of refraction above the magnetic plasma frequency means the slab refracts the cylindrical wave away from the normal, decreasing the power density at the receiving probe. Both of these effects result in low transmission at frequencies above the high-frequency edge of the stopband. For these reasons, the eigenmode analysis shown in Fig. 3.8 is typically used to determine where the medium exhibits a stopband due to negative permeability rather than transmission data.

3.1.3.2 Negative-Refractive-Index Focusing Measurements

To test the focusing characteristics of the NRI medium, the source was moved to a location 2cm away from the first interface of the lens. Now a substantial portion of the evanescent spectrum could reach the lens and could therefore be recovered by the NRI lens. In order to measure the fields over a two-dimensional space within the

PPW containing the NRI lens, a small slit less than 3mm in height was cut into the absorber at the end of the PPW opposite the source. A horizontal probe made out of 0.086in (2.18mm) semirigid cable, with the inner conductor polarized in the vertical direction, was inserted into the slit and could be moved independently with respect to the PPW. The probe was then used to scan the electric fields at the exit face of the lens and beyond using an automated computer routine that controlled the position of the translation stage to which the probe was attached. This program also interfaced with a HP8753D network analyzer to store the S-parameters observed at the probe locations. The performance of the probe was tested by measuring the fields within the empty PPW, that is, without the NRI lens present. The fields of the PPW were not disturbed by the presence of the probe in any observable way.

The NRI lens performed best at 2.424GHz, which corresponds to a shift of 1% from the design frequency of 2.45GHz. Since this frequency was found to be optimal for two separate lenses that were made, the shift can primarily be attributed to the manufacturing tolerances in the fabrication of the interdigitated capacitors. Fig. 3.10 shows contour plots of both magnitude and phase of a region up to 6.5cm beyond the second interface of the lens. Measurements were taken every 1.2mm in the $\hat{x}$ (longitudinal) direction and every 2.5mm in the $\hat{y}$ (transverse) direction. To prevent the NRI lens from being damaged by the probe or vice versa, the scan was started 2mm away from the face of the lens. The high fields observed close to the interface of the lens in Fig. 3.10(a) indicate the resonant amplification of the evanescent spectrum. The phase diagram shows a cylindrical wave emanating from the focus (located at [x,y] = [2,0]), confirming source reconstruction.

Fig. 3.11 plots the normalized measured electric field amplitude along the image plane (x = 2cm), as well as the diffraction-limited curve as a reference. The
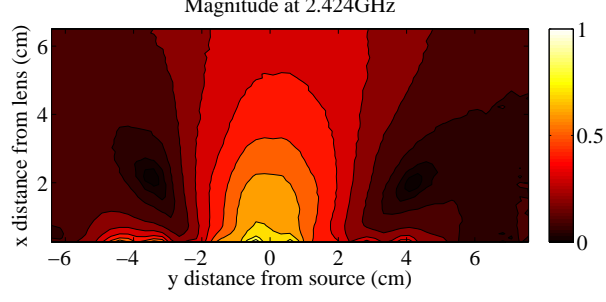
(a) Normalized field magnitude beyond the exit face of the NRI lens.
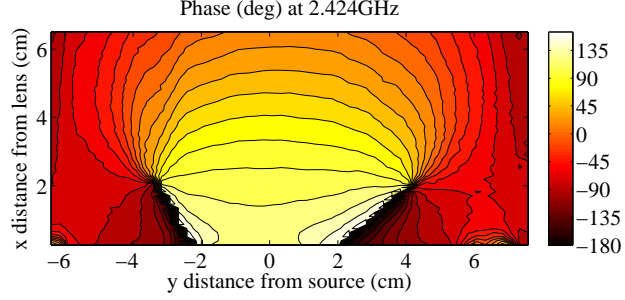
(b) Relative phase of the electric field beyond the exit face of the lens.

Figure 3.10: Plots of the measured vertically-polarized electric field at 2.424GHz

diffraction-limited curve is given by the following equation [50]:

$$
C \int_{\infty}^{\infty} \frac{e^{-jk_{x0}d}e^{-jk_{xn}d}e^{-jk_y y}}{k_{x0}} dk_y
$$
$$
k_{x0} = -k_{xn} = \sqrt{k_0^2 - k_y^2} \text{ for } k_y < k_0, \tag{3.2}
$$
$$
k_{x0} = k_{xn} = -j\sqrt{k_y^2 - k_0^2} \text{ for } k_y > k_0
$$

where $d = 4.00$cm and is defined as the thickness of the lens, k_{x0} represents the $\hat{x}$-directed propagation outside of the lens, k_{xn} represents the $\hat{x}$-directed propagation inside of the lens, and C is a normalization constant [50]. This equation accounts for both the propagating and evanescent portions of the spectrum at the focal plane. The propagating spectrum experiences phase advancement in the longitudinal direction as it travels through the NRI slab, hence $k_{x0} = -k_{xn}$ for $k_y < k_0$. The evanescent waves, on the other hand, are assumed to decay in both media, thus producing a

69

diffraction-limited curve. It is apparent by comparing the diffraction-limited curve and the experimental data that the proposed lens design does achieve super-resolution. The half-power beamwidth of the diffraction-limited curve is 0.36λ, as is expected for a line source of TM polarization outside of the reactive near field. The half-power beamwidth of the experimental curve is 0.252λ, which corresponds to a resolution enhancement of 2.0. In the experiment, this resolution enhancement is maintained over a bandwidth of 8MHz or 0.33%.
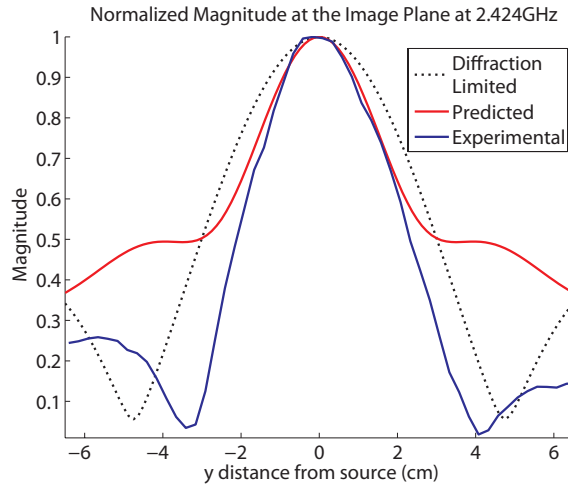
Figure 3.11: Normalized electric field magnitude at the image plane (x = 2cm). The experimental field magnitude is plotted with a solid line, the theoretical diffraction-limited field magnitude is plotted with a dotted line and the field magnitude as predicted by assuming a homogeneous, isotropic, lossy slab of the simulated material parameters given in the second section is plotted with a dashed line.

The bandwidth of resolution enhancement is notably smaller than the backward-wave bandwidth, but this is inherent to the phenomenon of super resolution. As mentioned previously and rigorously shown in [40, 41, 42, 43], to achieve super resolution at the image plane, μ_r and ϵ_r must be very close to -1. Because backward waves are inherently dispersive, the material parameters necessarily diverge from the ideal values as the frequency changes. The resolution enhancement bandwidth measures the bandwidth over which the material parameters are close enough to produce

a resolution enhancement of a particular value, in this case $R_e = 2.0$. This frequency range can be only a fraction of the full backward-wave bandwidth. Lowering the target resolution enhancement results in a broader range of material parameters that are capable of recovering the desired portion of the evanescent spectrum. As a result, the bandwidth of a specific resolution enhancement increases as the target enhancement value decreases.

The resolution enhancement is given by the equation

$$R_e = \frac{k_{ymax}}{k_0} \tag{3.3}$$

where k_{ymax} is the maximum transverse wavenumber that contributes to the image. This quantity can be obtained by finding k_{xmax}, which is given by the equation [41]

$$k_{xmax} = \frac{-j \ln |\Gamma_1|}{d} = \frac{-j}{d} \ln \left| \frac{\frac{\omega \mu_n}{k_{xn}} - \frac{\omega \mu_0}{k_{x0}}}{\frac{\omega \mu_0}{k_{x0}} + \frac{\omega \mu_n}{k_{xn}}} \right| \tag{3.4}$$

where Γ_1 is the Fresnel reflection coefficient at the first interface of the lens, k_{xn} is the magnitude of the $\hat{x}$ component of the wave vector in the NRI lens, μ_n is the permeability in the NRI lens and d is again the lens thickness. The indices of refraction for the lens and free-space are predicted to be approximately the same, therefore $k_{xn} \approx k_{x0}$. The equation simplifies to

$$k_{xmax} \approx \frac{-j}{d} \ln \left| \frac{\mu_r - 1}{\mu_r + 1} \right| \tag{3.5}$$

where μ_r is relative permeability of the NRI lens as given in the section 3.1.1. Once k_{xmax} is found, k_{ymax} is given by the separation relation $k_{ymax} = \sqrt{k_0^2 - k_{xmax}^2}$. Then using Equation (3.3), the resolution enhancement is calculated to be 2.01, which is in excellent agreement with the experimental value of 2.0.

Alternatively, the expected resolution enhancement can be found by deriving the

optical transfer function (OTF) for an isotropic, homogeneous NRI lens of thickness d, infinite width and the same material parameters that were reported in section 3.1.1. This method does not rely on the approximations used in Eq. (3.5), so it remains applicable even if the condition $k_{xn} \approx k_{x0}$ is not satisfied. From the OTF, the resolution enhancement was determined to be 1.98, again in good agreement with the experiments.

Both of the previous methods used to calculate the resolution enhancement assume that the slab is infinite in extent. To verify that these equations are still applicable to the finite structure used in the experiments, two homogeneous slabs having the same material parameters as those given in section 3.1.1 were simulated using HFSS. The first had a transverse ($\hat{y}$) dimension equal to 15cm; the second had a transverse dimension equal to 40cm. These widths correspond to numerical apertures of $NA = \sin(75.1°) = 0.966$ and $NA = \sin(84.3°) = 0.995$, respectively. The normalized electric field magnitude at the image plane is shown in Fig. 3.12. The smaller numerical aperture exhibited a resolution of 0.248λ and the larger numerical aperture exhibited a resolution of 0.255λ, which both closely match the measured value of 0.252λ. This shows that the resolution enhancement is not significantly affected by the truncation of the structure.

3.2 Free Space Measurements of NRI Media

The previous section provided verification that broadband volumetric NRI media could be designed and used for super-resolved focusing. However, the material parameters of the slab, such as the permeability, permittivity and loss, could only be calculated from simulation rather than extracted from experimental data. The simplest method of measuring the material parameters of a metamaterial slab is to illuminate it with a normally incident plane wave to obtain the S-parameters. This was not possible using cylindrical sources in a parallel plate waveguide, so a new lens
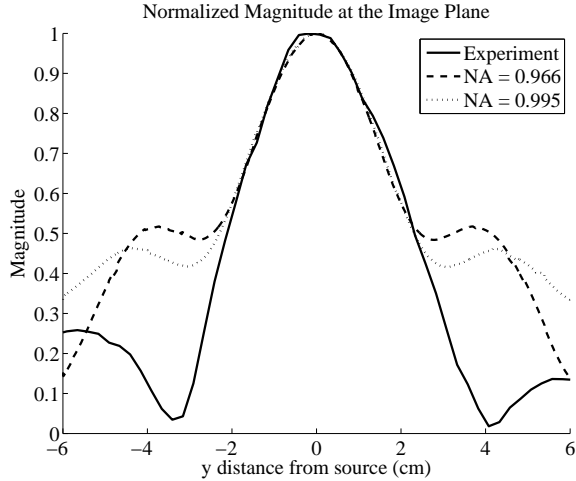
Figure 3.12: Normalized electric field magnitude at the image plane (x = 2cm) for two homogeneous slabs having numerical apertures of 0.966 (dashed) and 0.995 (dotted) compared to the experimental results (solid).

was designed to operate in free space over X-band frequencies. One unit cell of the design is shown in Fig. 3.13. This design, while similar to the one in Fig. 3.1, was much easier to fabricate because the transmission-line cage was constructed using a single circuit board. The capacitive grids were printed on either side of a single substrate and were connected by copper-plated vias rather than wire posts that must be soldered manually. The ease of fabrication allowed for the construction of an electrically large slab, which had a transverse extent of 5λ at its operating frequency of 10.435GHz.

3.2.1 Design

One unit cell of the broadband NRI medium is shown in Fig. 3.13, with the physical dimensions provided in Table 3.1. In the absence of the central wire, the structure represents one unit cell of the negative permeability medium, which is formed by the remaining transmission-line cage introduced in Chapter II. Again, the central wire is used to achieve negative permittivity in the NRI medium for waves with vertically-polarized electric fields.

73
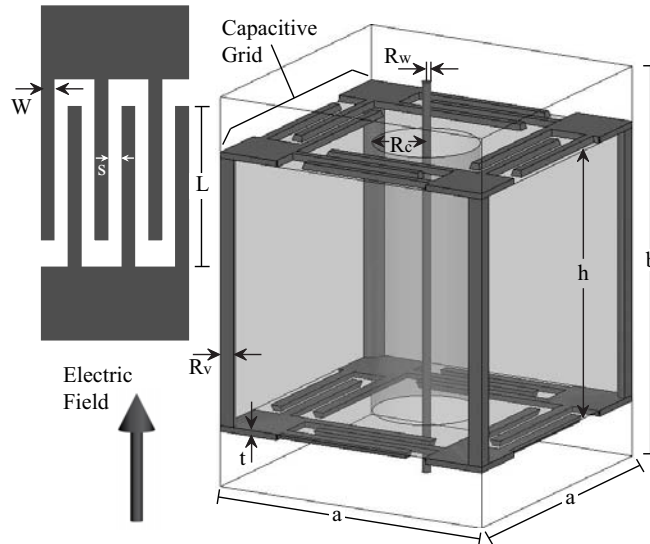
Figure 3.13: Unit cell of the broadband NRI medium with an enlargement of the interdigitated capacitor footprint. Removing the central wire results in the unit cell of the broadband negative-permeability medium.

As in the earlier NRI lens, the material parameters of the free-space metamaterial were designed such that the lens would produce a super-resolved focus at the operating frequency, necessitating that $\mu_r \approx \epsilon_r \approx -1$. The electric response of the transmission-line cage generally increases the relative permittivity of the medium, similar to structures described in [52]. In the structure shown in Fig. 3.13, the increase in permittivity is particularly significant due to the large area occupied by the interdigital capacitors. This higher permittivity has two consequences: one ad-

Parameter	Description	Designed	Measured
a	Unit cell width	2.54mm	2.54mm
b	Unit cell height	3.40mm	3.40mm
h	Substrate height	2.34mm	2.29mm
t	Conductor thickness	52μm	40μm
R_w	Central wire radius	39μm	39μm
R_v	Via radius	127μm	165μm
R_c	Drilled hole radius	457μm	457μm
L	Length of capacitor finger	1.22mm	1.22mm
W	Width of capacitor finger	100μm	$100\pm10\mu$m
s	Spacing between fingers	100μm	$100\pm10\mu$m

Table 3.1: Dimensions of the NRI unit cell.

vantageous and one detrimental. The advantage is that thicker wires (i.e. lower inductances) can be used to achieve $\epsilon_r = -1$ at the design frequency. This is particularly important since higher gauge wires (AWG>40 or R_w<39μm) exhibit higher losses and are quite fragile. The disadvantage is that as frequency increases the relative permittivity approaches a value above $\epsilon_r = 1$, while the relative permeability remains lower than $\mu_r = 1$. Since $\mu_r = \epsilon_r = -1$ at a lower frequency, the slope (with respect to frequency) of the permittivity is greater than the slope of the permeability at these higher frequencies. Consequently, in impedance-matched structures, the electric plasma frequency is significantly lower than the magnetic plasma frequency ($f_e < f_m$), and the high-frequency end of the backward-wave band is limited by the permittivity response.

This decrease in bandwidth for the impedance-matched structure is illustrated in Fig. 3.14. The dispersion diagram of the NRI medium with the nominal parameters given in Table 3.1 shows that the backward-wave bandwidth of this structure is 49.2%. However, if the impedance of the medium is not a concern, the bandwidth can be made much larger. Increasing the height of the unit cell, b, and the wire radius, R_w, increases the electric plasma frequency providing a wider NRI bandwidth. Additional bandwidth can be achieved by lowering the low-frequency resonance of the negative permeability medium. This is done by extending the length of the interdigital fingers of the capacitor, thereby increasing the capacitance. By optimizing these three parameters, the NRI bandwidth can be increased up to 68.2%. This shows that this topology of NRI media can achieve bandwidths even larger than those measured in the experimental structure, if one is not constrained by the impedance matching criterion.

For all metamaterials that can be described by effective medium theory, the unit cell width is required to be much smaller than a wavelength (specifically, a $< \frac{\lambda_0}{10}$) to ensure isotropic propagation throughout the medium. The design in Fig. 3.13 satisfies
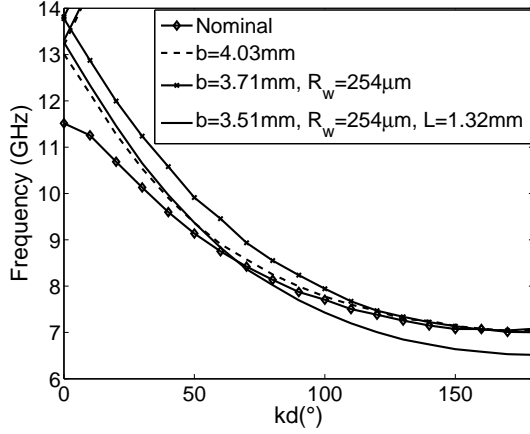
Figure 3.14: Variations in backward-wave bandwidth of the NRI medium through the change of its geometric parameters. In all cases except the nominal, $f_e = f_m$, but the medium is not impedance-matched to free-space.

this condition for all frequencies in the backward-wave band, ensuring the validity of effective medium theory at the operating frequency where $n \approx -1$. Despite meeting this requirement, the effective medium theory breaks down at low frequencies, where the permeability diverges and the phase delay across the unit cell is large. In this region, the refractive index has a very large magnitude, such that a $\approx \frac{\lambda_{NRI}}{2}$. When this occurs, the NRI medium exhibits spatial dispersion, as can be seen in Fig. 3.15. However, for frequencies closer to the operating point ($f > 9\text{GHz}$), the medium exhibits two-dimensionally isotropic behavior for waves propagating in the $\hat{x}$-$\hat{y}$ plane, as indicated by the circular contours at these frequencies.

3.2.2 S-Parameter Measurements

Using the design with the physical parameters listed in Table 3.1, NRI and negative-permeability slabs with thicknesses of four cells (1.02cm) were constructed in order to measure their material properties. The slabs were built using 46 horizontal printed-circuit-board layers, which were spaced 1.07mm apart. Each layer consisted of a capacitive grid printed on each face of the board (shown in Fig. 3.16). These grids were connected to each other by vias of radius R_v, as shown in Fig. 3.13. The

76
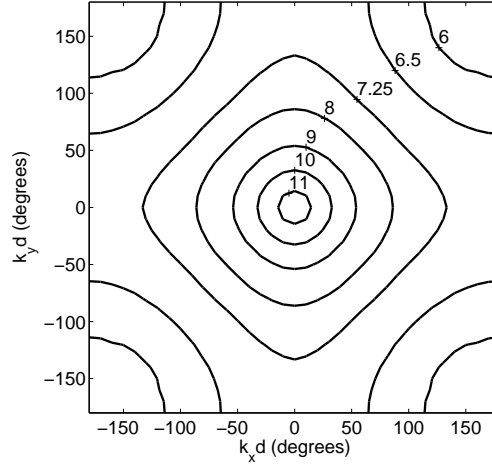
Figure 3.15: Equifrequency contour plot of the infinite NRI medium. The frequencies of each contour are labeled in GHz.
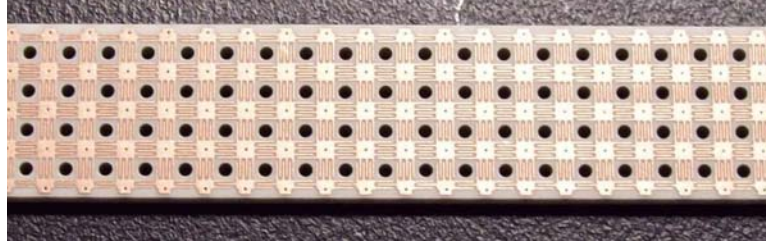
Figure 3.16: Photograph of the capacitive grid on one of the printed-circuit-board layers used to construct both the negative-permeability and NRI slabs.

layers were held with the prescribed spacing by a plastic holder on either end. Once assembled, this structure formed the negative-permeability slab discussed below. The NRI lens was constructed using the same printed-circuit-board layers which were supported in the same fashion, but vertical wires were threaded through the center of each unit cell. The wires were then attached with silver epoxy to ground planes located at the top and bottom of the structure.

To measure the scattering parameters (S-parameters) of these slabs in free space, the samples were illuminated with a tightly focused, collimated source. In order to produce a collimated beam that was confined within a small radius, a quasi-optical Gaussian beam telescope was used [53]. The telescope consisted of a rectangular horn antenna and a pair of lenses, known as an achromatic doublet [54]. As the
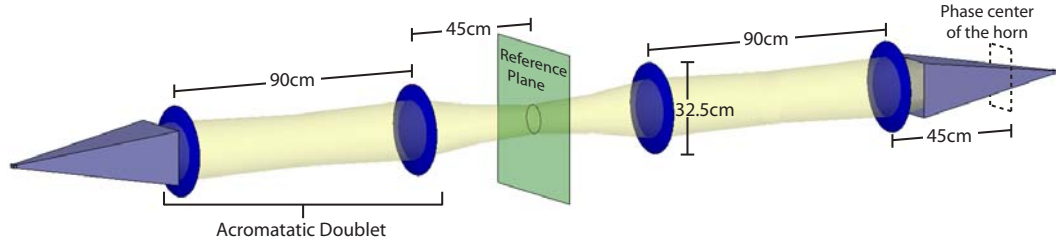
Figure 3.17: Schematic of the Gaussian beam telescope measurement system. The reference planes of the Gaussian beam telescopes are assumed to be aligned at the green plane.

name suggests, the achromatic doublet produced a focus whose size and location were independent of frequency. An additional benefit of using a pair of lenses rather than a single lens was that the spot size at the focus was much smaller. Each lens in the doublet was made of Rexolite ($n = 1.59$) and was bi-hyperbolic in shape. The diameters of the lenses were 32.5cm and the input and output focal distances were equal to 45cm. The reference plane of the Gaussian beam telescope occurred at the output focus of the second lens, 1.8m away from the input beam waist of the horn antenna. A schematic of the quasi-optical measurement setup is shown in Fig. 3.17.
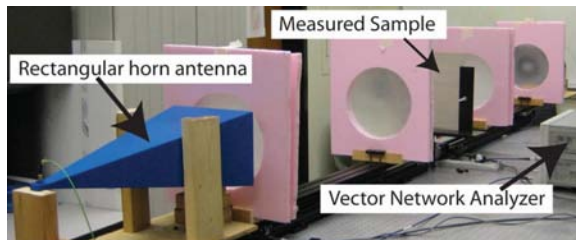
Figure 3.18: Photograph of the quasi-optical, free-space measurement system.

The S-parameters of the slabs were measured by placing the metamaterial sample between two Gaussian-beam telescopes, as shown in Fig. 3.18. Each telescope was placed on a separate linear translation stage, whose position was controlled by a stepper motor with 5μm accuracy. This allowed the reference planes to be exactly aligned with the faces of the slab. The beam radii at the focal planes were approximately 5cm, while the slabs measured 16cm high and 16cm wide. As a result, the amplitude of the Gaussian beam was 20dB lower at the edge of the sample than at its

center, limiting diffraction from the slab. The horn antennas of each telescope were connected to the two ports of an Agilent E8361A network analyzer, which collected the transmission and reflection data.

Before any data were taken, the system was calibrated using a free-space Thru-Reflect-Line (TRL) calibration method. This calibration de-embedded the S-parameters of the slab from those of the entire measurement system. The calibration of the measurement system was particularly important because it corrected for the imperfections inherent in the system's design. One such issue was that the phase centers of the horn antennas were frequency dependent. This caused the input beam waist (the phase center of the horn) to deviate from the input focus of the achromatic doublet for some frequencies. This, in turn, caused the output beam waist not to coincide with the output focus of the doublet, which resulted in imperfect collimation at the reference plane for those frequencies. This effect, however, was slight since the deviation in beam waist position was small relative to the Rayleigh range [53]. Nevertheless, the TRL calibration was able to account for the phase variation over the reference plane and eliminate its effects. A second issue was that the Gaussian beam telescopes were designed to focus the fundamental Gaussian mode. However, the rectangular horn antennas only coupled 88% of their power into the fundamental mode [55], with the rest of the power being coupled into higher-order modes. These higher-order modes have larger effective beam radii than the fundamental, which made them more susceptible to diffraction losses. Consequently, some of the power in higher-order modes escaped the measurement system. Fortunately, these losses increased the purity of the transmitted beam, while the effect of the lost power was eliminated through the calibration process. The TRL calibration also accounted for scattering from proximate objects, most notably, the plastic stand which supported the sample. To check the accuracy of the calibration, commercial microwave substrates were measured and their permittivity and permeability values were verified.

79

Due to errors in the manufacturing process, some of the dimensions shown in Fig. 3.13 were slightly different from those on the fabricated structure. Both the values of the original design as well as those measured on the fabricated boards are presented in Table 3.1. The most significant changes were in the substrate height (designed as 2.34mm, measured as 2.29mm) and the via diameter (designed as 254μm, measured as 330μm). These errors shifted the design frequency from 10GHz to 10.435GHz. The simulations were redone to accurately reflect the dimensions of the measured structure. The new simulated results are used in the remainder of this section, rather than those of the original design.
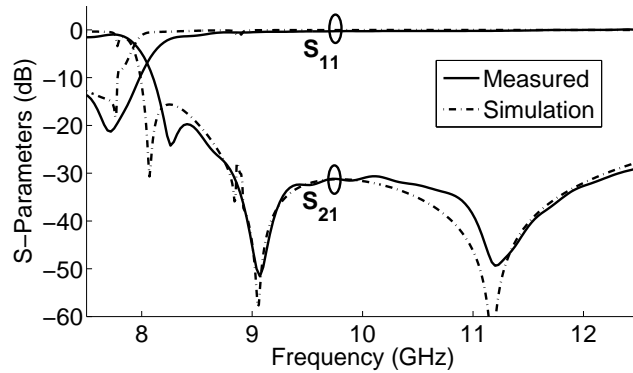
Figure 3.19: Simulated and measured magnitudes of S_{11} and S_{21} for the negative-permeability slab.
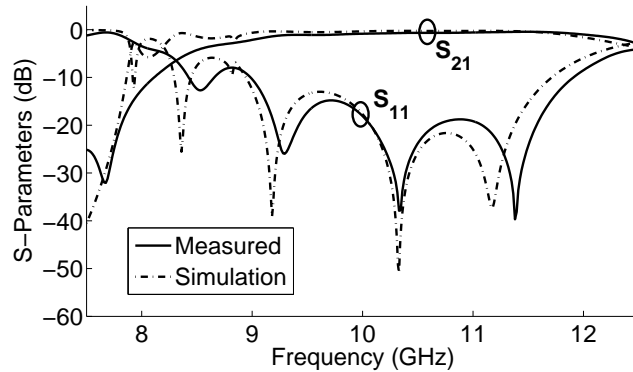
Figure 3.20: Simulated and measured magnitudes of S_{11} and S_{21} for the NRI lens.

The measured S-parameters of the negative-permeability medium are compared to simulation in Fig. 3.19. By calculating the effective permeability from the S-

parameters, the structure was found to exhibit negative permeability over a bandwidth of 45.3%. In this negative-permeability region, the slab provided excellent attenuation (S_{21}<-30dB) over a frequency range of 8.86GHz to 12.3GHz. Additionally, the medium exhibited low loss throughout this frequency range. At the operating frequency of 10.435GHz, the four-cell negative-permeability slab experienced material losses of only 0.235dB.
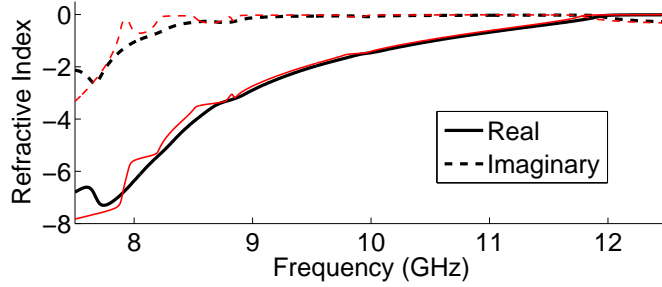
Figure 3.21: Real (solid lines) and imaginary (dashed lines) parts of the measured (thick, black lines) and simulated (thin, red lines) index of refraction of the NRI slab.
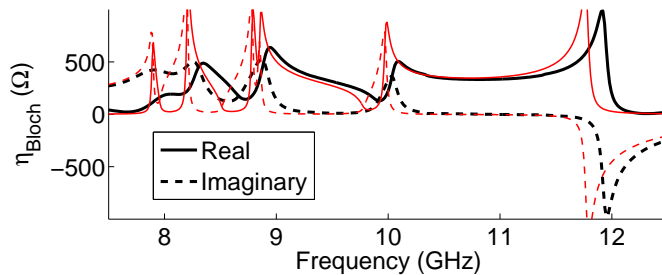
Figure 3.22: Real (solid lines) and imaginary (dashed lines) parts of the measured (thick, black lines) and simulated (thin, red lines) impedance of the NRI slab. The singularities are due to Fabry-Perot resonances of the slab.

The measured and simulated S-parameters of the NRI lens are shown in Fig. 3.20. The slab exhibited S_{11}<-10dB from 8.99GHz to 11.91GHz, indicating that the structure was well-matched to free space over this frequency range. The S-parameters were used to calculate the material properties of the NRI lens, such as index of refraction (Fig. 3.21), impedance (Fig. 3.22), permeability and permittivity (Fig. 3.23), and loss (Fig. 3.24). As shown in Fig. 3.23, both permittivity and permeability are
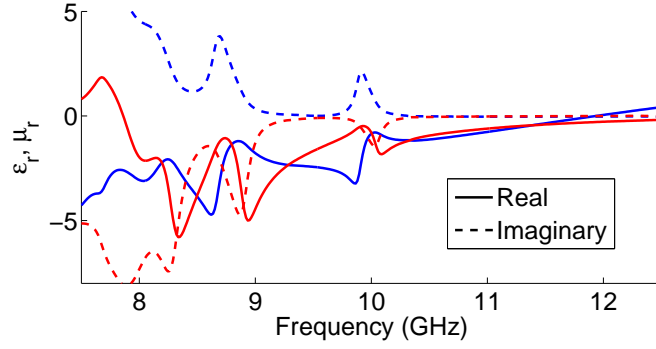
Figure 3.23: Real (solid lines) and imaginary (dashed lines) parts of the measured relative permittivity (blue) and permeability (red) of the NRI slab. The singularities are due to Fabry-Perot resonances.
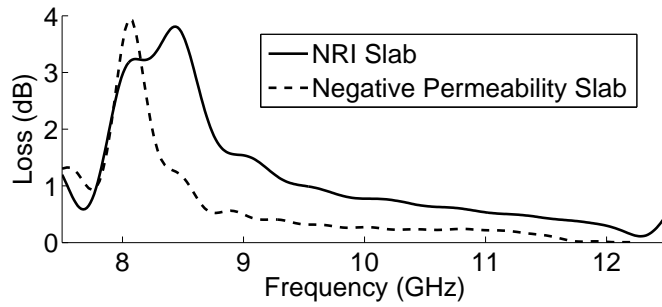
Figure 3.24: Measured loss of the NRI (solid line) and negative-permeability (dashed line) four-cell slabs.

negative over a bandwidth of 41.2%. The resonant frequency of the permeability ($f_o = 7.86$GHz) limits the bandwidth at low frequencies, while the high-frequency limit is the electric plasma frequency ($f_e = 11.93$GHz). The extracted permittivity and permeability curves display unusual behavior below 10GHz. At these frequencies, the unit cells exhibit spatial dispersion, degrading the accuracy of the effective medium theory. Additionally, the material parameter extraction method used to calculate the wave impedance breaks down when the electrical length of the NRI slab is a multiple of $\frac{\lambda}{2}$ [46]. This phenomenon occurs around 7.8GHz, 8.2GHz, 8.7GHz and 10.0GHz for the measured slab (see Fig. 3.22). Since the wave impedance is used to calculate relative permittivity and permeability, the extraction inaccuracies are inherent in these curves as well. As a result, the permittivity curve has a positive

imaginary part close to the resonant frequencies, which might raise concerns about the structure exhibiting gain. To verify the passivity of the medium, one should focus on the index of refraction (Fig. 3.21), for which the extraction method remains accurate even at resonant lengths. The imaginary part of the index of refraction is negative for all frequencies, as is required for a passive structure. The passivity the material is further verified by Fig. 3.24, which shows that the loss is positive for all frequencies. Additionally, Fig. 3.24 shows that despite having high losses close to the resonant frequency (f_o), the losses are less than 1dB for the entire four-cell slab for all frequencies above 9.5GHz. This means that the majority of the backward-wave bandwidth is low-loss, making this lens suitable for practical microwave applications.

The operating frequency of the NRI lens is 10.435GHz, which corresponds to the frequency at which the relative permeability was closest to -1. The material parameters at this frequency were found to be $\epsilon_r = -1.16 - j0.01$ and $\mu_r = -1.00 - j0.05$. At the operating frequency, the entire four-cell ($\frac{\lambda_0}{3}$) slab exhibited a loss of only 0.67dB, or 0.17dB/cell. The low loss performance of the slab was further verified by the measured figure of merit ($FOM = \frac{n'}{n''}$), which was calculated to be 31.4 at the design frequency.

The bandwidth, loss and FOM of the NRI lens are compared with other NRI media reported in literature in Table 3.2. These media represent several different topological approaches to achieving a negative index of refraction, including SRR/wire arrays [56, 57], a planar NRI transmission-line (TL) medium [50] and volumetric NRI TL media [58, 59] in addition to the proposed structure. The planar NRI TL medium has a bandwidth conspicuously larger than any of the other topologies. This is primarily because this medium uses chip components, by which much higher capacitance and inductance values can be realized compared to printed elements. This medium also exhibits a FOM slightly higher than the one measured in the proposed structure, however, the value in [50] is taken from simulation. Comparison of this value to the

Author	Frequency	Bandwidth	Loss Per Cell	FOM
Measured Structure	10.435GHz	41.2%	0.17dB	31.4
Simulated Structure	10GHz	41.1%	0.07dB	70.2
Li et. al. [56] *	14.2GHz	10.1%	0.37dB	-
Grbic et. al. [50]	1.057GHz	107.3%	-	32.1 †
Aydin et. al. [57]	3.74GHz	7.9%	2.7dB	12.07
Iyer et. al. [58]	11.5GHz	24.2%	1.2dB	-
Iyer et. al. [59]	2.4GHz	20.7%	0.2dB †	-

Table 3.2: Comparison of the loss performance of NRI media

full-wave simulation of the proposed structure is more appropriate. In that case, the FOM of the planar NRI TL medium is less than half of the proposed structure's FOM, despite operating at a frequency one order of magnitude lower.

Compared to all other volumetric structures, the measured structure exhibits lower loss and wider bandwidth regardless of topology or frequency of operation. As is expected, the SRR/wire media have the narrowest bandwidths compared to other topologies. The bandwidths of the volumetric NRI TL media are better but still about half that of the proposed structure. Unlike the bandwidth, the per-unit-cell losses of these NRI media do not form a predictable pattern. While the proposed structure exhibits the best loss performance, a relationship between topology and loss remains unclear. Such variation can be attributed to a lack of standardization in the way each medium is designed. In each structure, the substrate, Q-factor of the loading elements, unit cell size (in terms of wavelength) and operating frequency are different. All of these factors influence the loss performance of a NRI medium. Further confusing the matter, the reported losses are often the minimum losses that occur in the backward-wave band, rather than those that occur at the frequency of operation. To exemplify the difference, the proposed structure exhibits losses as low as 0.095dB/cell at the high-frequency edge of the backward-wave band (11.9GHz),

---

*One-dimensional propagation only
†Quoted from simulation

which is much lower than the 0.17dB measured at the operating frequency. Regardless of these many differences, the structure in Fig. 3.13 clearly represents the realization of a volumetric NRI medium with the widest bandwidth and lowest loss performance of any design published to date.
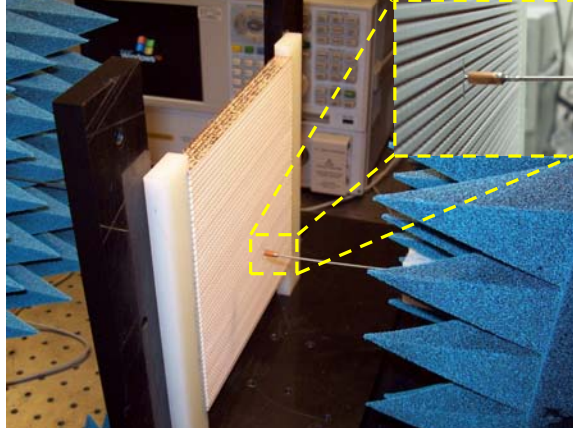
Figure 3.25: Photograph of the near-field focusing measurement setup. The inset shows an enlargement of the dipole probe with a sleeve balun.

3.2.3 Focusing Experiments

In addition to measuring the S-parameters of the NRI lens, focusing experiments were also performed. Two dipoles with sleeve baluns were used to excite the lens and probe the fields around it. The dipoles (each of which were 7.1mm or $\lambda_0/4$ in length) were oriented such that the electric field incident on the lens was vertically polarized. One probe was used as a source and held a fixed distance of 5.08mm (half the lens thickness) away from the lens. The other probe was attached to a three-dimensional translation stage and used to scan the fields beyond the exit face of the lens. The vertically-polarized electric field was measured on a horizontal plane, such that both the scanning probe and the source probe were at the same height. The half-power beamwidth was measured at the image plane, located 5.08mm away from the exit face of the lens, and evanescent spatial frequencies were recovered from 10.015GHz to 10.78GHz, a fractional bandwidth of 7.4%. The normalized magnitude and phase
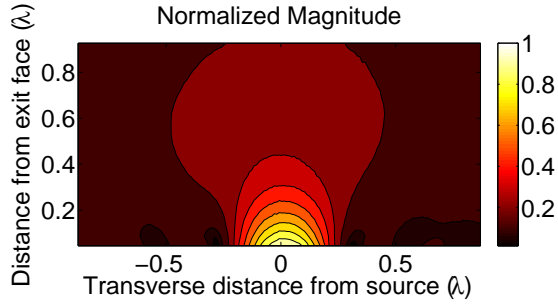
(a) Contour plots of the normalized electric field magnitude on the exit side of the NRI lens.
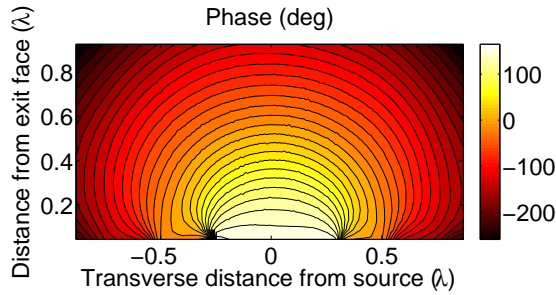
(b) Contour plots of the unwrapped electric field phase on the exit side of the NRI lens.

Figure 3.26: Plots of the measured vertically-polarized electric field at 10.435GHz.

of the vertically-polarized electric field at 10.435GHz are shown in Fig. 3.26.

Fig. 3.27 shows the normalized field amplitude at the image plane at 10.435GHz. A half-power beamwidth of $0.27\lambda_0$ was observed, which is significantly narrower than the diffraction-limited beamwidth for a line source of $0.36\lambda_0$. Fig. 3.28 shows how the focus changes with frequency, plotting curves for several frequencies at which super-resolution is observed.

To provide a point of comparison, the field was measured in the absence of the lens as well. The normalized field amplitude for this measurement is also plotted at the operating frequency of 10.435GHz in Fig. 3.27. Prior to normalization, the electric field magnitude measured with the lens present was 88% higher than without the lens.

The dashed curve in Fig. 3.27 represents the theoretical image of a vertically-directed line current as predicted by the impedance and propagation constant of the
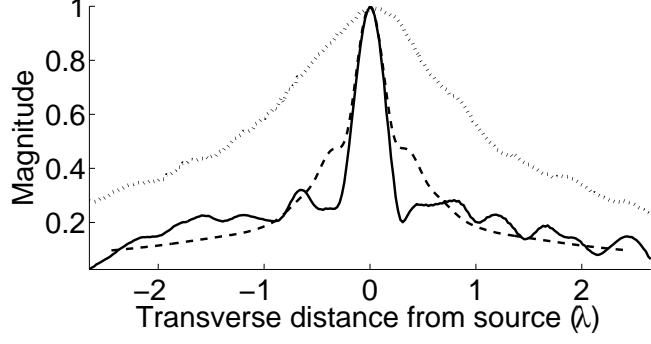
Figure 3.27: Normalized electric field magnitude at the image plane at 10.435GHz for the measured field with (solid line) and without (dotted line) the lens, as well as the predicted field with the lens (dashed line).
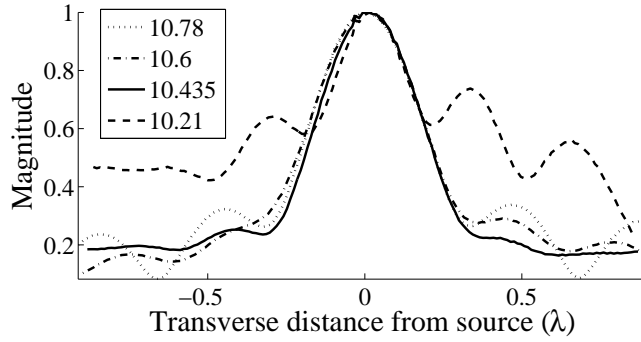
Figure 3.28: Normalized electric field magnitude at the image plane for several frequencies exhibiting sub-diffraction-limited focusing.

NRI medium (η_n and k_n, respectively), which were measured in section 3.2.2. The field at the image plane is calculated by first finding the transfer function of the lens in terms of the transverse wavenumber $k_{||}$. This is given by the expression

$$
\begin{aligned}
T\left(k_{||}\right) &= \frac{E_{image}\left(k_{||}\right)}{I_{source}\left(k_{||}\right)} \\
&= \frac{\eta_0 k_0}{k_{\perp 0}} \cdot \frac{\left(1 - \Gamma^2\right) \cdot e^{-jk_{\perp 0}4a} e^{-jk_{||}x}}{e^{jk_{\perp n}4a} - \Gamma^2 \cdot e^{-jk_{\perp n}4a}}
\end{aligned}
\tag{3.6}
$$

87

where

$$\Gamma = \frac{\eta_n k_n k_{\perp 0} - \eta_0 k_0 k_{\perp n}}{\eta_n k_n k_{\perp 0} + \eta_0 k_0 k_{\perp n}}$$

$$k_{\perp 0} = \sqrt{k_0^2 - k_{||}^2} \text{ for } k_{||} < k_0,$$

$$k_{\perp n} = -\sqrt{k_n^2 - k_{||}^2} \text{ for } k_{||} < k_n,$$

$$k_{\perp 0} = -j\sqrt{k_{||}^2 - k_0^2} \text{ for } k_{||} > k_0$$

$$k_{\perp n} = j\sqrt{k_{||}^2 - k_n^2} \text{ for } k_{||} > k_n.$$

Then the contribution of the continuum of transverse wavenumbers was calculated for each point x along the image plane, resulting in the expression

$$E_N(x) = C \cdot I_{source} \int_\infty^\infty T\left(k_{||}\right) dk_{||} \tag{3.7}$$

where C is a constant that normalizes the maximum field amplitude at the image plane to 1. As Fig. 3.27 shows, the focus predicted by this analysis agrees well with the one obtained experimentally. The agreement between the focusing and transmission measurements confirms the results of both experiments. Furthermore, since the predicted curve was calculated under the assumption of a homogeneous slab, its agreement with the measured focal pattern validates the use of effective medium theory in designing the NRI metamaterial.

To further demonstrate the resolution enhancement produced by the lens, Fourier transforms of all three curves shown in Fig. 3.27 were calculated and are plotted in Fig. 3.29. Again, the spectrum of the field measured with the lens present exhibited good agreement with the spectrum predicted analytically using the measured material parameters. Both of these curves include evanescent Fourier components ($|k_{||}| > k_0 = \frac{2\pi}{\lambda_0}$), indicating the recovery of evanescent waves at the focal plane. However, the spectrum calculated from the field in the absence of the lens only includes $|k_{||}| \leq k_0$,

corresponding to propagating waves. This shows that without the lens, the evanescent waves decayed completely before reaching the focal plane, while with the lens, part of the evanescent spectrum was recovered.
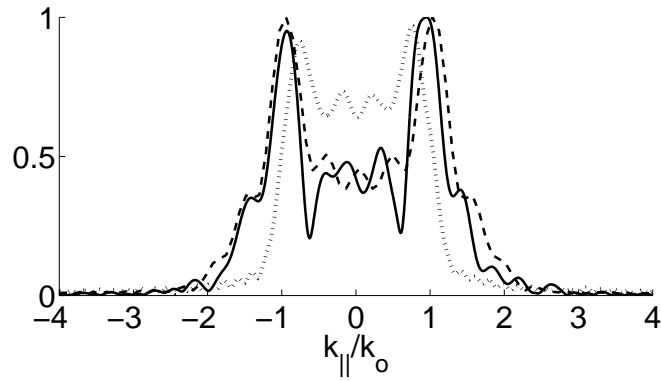
Figure 3.29: Normalized Fourier transform magnitude of the field at the image plane for the measured field with (solid line) and without (dotted line) the lens, as well as the predicted field with the lens (dashed line). The values of these curves are normalized by the peak amplitude of the spectrum calculated with the lens present.

CHAPTER IV

Isotropic NRI Media

Expanding the backward-wave bandwidth of negative-refractive-index (NRI) media represented an important step towards making these metamaterials suitable for real-world applications. However, the designs presented worked only for electromagnetic waves of a specified polarization. In fact, all of the NRI metamaterials that have been fabricated to date were polarization dependent [13, 15, 44, 56, 57, 58, 59, 60]. This shortcoming has prevented NRI lenses from achieving the three-dimensional reconstruction of arbitrary sources that has been discussed theoretically [12]. In this chapter, the problem of polarization-dependent material parameters in NRI media is addressed through the development of a volumetric metamaterial that exhibits a NRI for waves of any polarization over a broad backward-wave bandwidth.

4.1   Design of the Isotropic NRI Medium

One might think that isotropic NRI media have not been fabricated due to the inability to realize either negative permittivity or negative permeability isotropically, but this is not the case. In fact, isotropic negative permittivity and negative permeability have both been observed, albeit in separate materials. Isotropic negative permittivity media exist in the natural world in the form of metals below their plasma frequencies [61] and ionized gases in the ionosphere. Further, specific negative permit-

tivity values can be engineered at microwave frequencies by using a three-dimensional wire grid [7, 32] rather than a solid block of metal, as used at optical wavelengths. Although isotropic negative permeability media are not as readily available, one such medium was constructed from a lattice of split-ring resonators (SRRs) designed to resonate at 63.28MHz [17]. Despite the ability to realize isotropic negative permeability and isotropic negative permittivity separately, metamaterials with both properties have remained elusive due to the fabrication challenges associated with combining the elements responsible for negative permittivity and negative permeability into a single medium. Several theoretical designs for isotropic NRI media have been proposed [18, 19, 62], but none have been manufactured due to their complicated three-dimensional assembly.

Beyond the fabrication difficulties inherent in creating isotropic NRI metamaterials, the practical issues of bandwidth and loss discussed in the preceding chapters also hindered the development of polarization-independent media. Naturally, maintaining the improved bandwidth and loss performance achieved in broadband polarization-dependent structures [44, 58, 59, 60, 63] was emphasized in the design of the isotropic NRI medium. The development of a broadband, low-loss, isotropic NRI metamaterial would address three of the most significant problems with NRI media and would allow them to be more readily incorporated into practical microwave applications.

4.1.1 Topology of the Isotropic NRI Medium

The desire for the isotropic NRI metamaterial to exhibit broad bandwidth precludes the use of SRR [17] or resonant-sphere arrays [62] to achieve negative permeability. The electrical connections between unit cells in the transmission-line cage introduced in Chapter II prevent that topology from being used to realize isotropic negative permeability as well. As a result, a new metamaterial element that exhibits isotropic negative effective permeability was developed: the split-cube res-
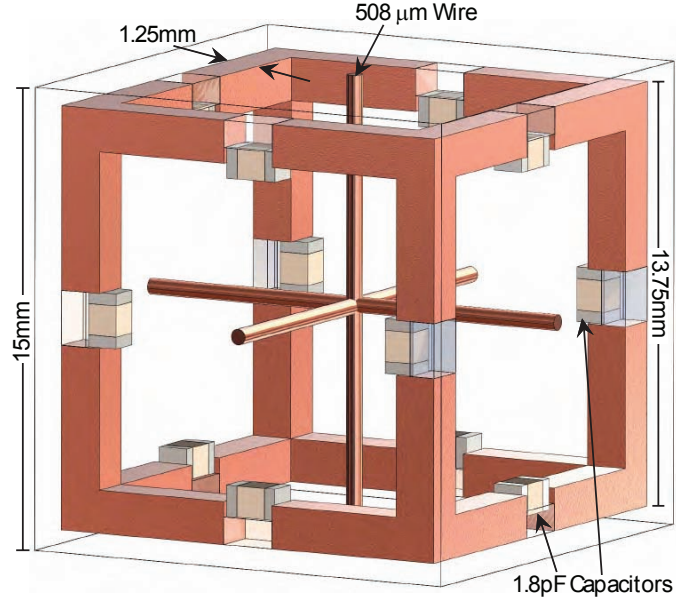
Figure 4.1: One unit cell of the 3-D isotropic NRI medium.

onator (SCR), which can be seen in Fig. 4.1 [64]. The SCR can be considered the three-dimensional analogue to the SRR. Instead of a two dimensional ring shape, the SCR is based on a three-dimensional cubic frame. Since the SCR is already a three-dimensional structure, the complete negative permeability medium can be constructed simply by placing these structures side-by-side. This fabrication method is much easier than assembling interconnected lattices of two-dimensional printed circuit boards, as is necessary when using SRRs.

In addition to its straightforward manufacturing process, the cubic shape of the SCR gives it full octahedral symmetry (i.e. it is of the point group O_h [65]). This means that the structure can be rotated 24 different ways and reflected 24 different ways without changing its appearance. The symmetry allows the SCR to produce the same magnetic response regardless of the direction in which the incident magnetic field is oriented, making this single element capable of producing polarization-independent negative permeability.

As in the previous NRI media discussed in this thesis, negative permittivity is realized using thin wires. To achieve isotropic negative permittivity, the wires are

92

oriented along all three axes of the cubic unit cell, as shown in Fig. 4.1. This wire grid also exhibits full octahedral symmetry, so the permittivity response is the same no matter the direction of the electric field. When the wire grid is integrated with the SCR array, the complete medium exhibits a NRI independent of polarization.

4.1.2 Eigenmode Simulations
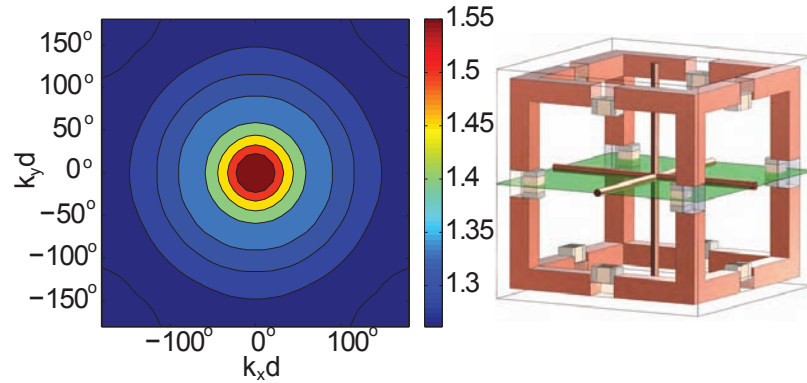
(a) Isofrequency countours in the $\hat{x} - \hat{y}$ plane.
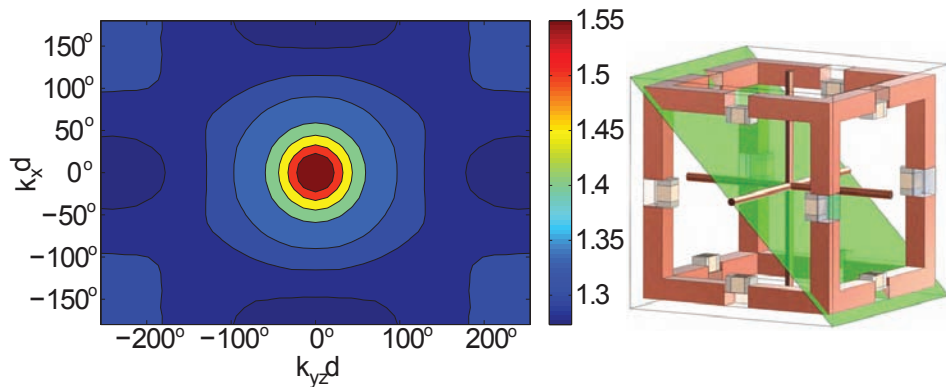
(b) Isofrequency countours in the $\hat{x} - \hat{y}\hat{z}$ plane.

Figure 4.2: Isofrequency contour plots for the unit cell shown in Fig. 4.1. The green planes indicate the plane in which propagation was confined for a each contour plot.

The symmetry of the unit cell alone does not guarantee isotropic propagation. The phase delay across the unit cell must also be sufficiently small to ensure that the metamaterial does not suffer from spatial dispersion. The maximum allowable phase delay depends on the specific application, but as a general rule, the electrical

length of the unit cell should be less than $\lambda_0/10$. A target operating frequency of 1.5GHz ($\lambda_0 = 20$cm) and a unit cell size of 1.5cm (0.075λ) were chosen in order to ensure isotropic propagation over all frequencies of interest. In order to determine the isotropy explicitly, the isofrequency contours [66] for the NRI index mode of the unit cell were obtained from HFSS eigenmode simulations. Fig 4.2 shows the isofrequency contours for propagation in two different planes: the horizontal plane (Fig. 4.2(a)) and a plane that cuts the unit cell along a diagonal (Fig. 4.2(b)). Each isofrequency contour plot indicates the plane in which the propagation vector was confined by the green plane in the adjacent unit cell diagram. In Fig. 4.2(a), $k_x d$ and $k_y d$ were swept independently from $0°$ to $180°$ while $k_z d$ was held constant at $0°$. In Fig. 4.2(b), the phase delay $k_x d$ was swept independently from $0°$ to $180°$, while the phase delays in the $\hat{y}$ and $\hat{z}$ were both swept from $0°$ to $180°$ such that $k_y d = k_z d$. The isofrequency contours are plotted with respect to $k_x d$ and $k_{yz} d$, where $k_{yz} d = \sqrt{(k_y d)^2 + (k_z d)^2}$. As a result, $k_{yz} d$ has a maximum value of $254.6°$ rather than $180°$. As can be seen in Fig. 4.2, the simulated isofrequency contours for the unit cell's NRI mode are nearly circular for frequencies above 1.4GHz. Therefore, the unit cell exhibits isotropic propagation for frequencies above 1.4GHz that are also in the NRI frequency range.

Eigenmode simulations were also performed to obtain the three-dimensional dispersion diagram (described in Appendix A) of the infinite isotropic NRI medium. The first four modes of the unit cell are plotted in Fig. 4.3. The lowest two modes are the NRI modes, as indicated by the negative slope of their eigenfrequencies as the phase delay varies from Γ ($k_x d = 0°$, $k_y d = 0°$, $k_z d = 0°$) to X ($k_x d = 180°$, $k_y d = 0°$, $k_z d = 0°$). These two modes represent the two orthogonal polarizations that can propagate through the medium in a specific direction (e.g. for propagation in the $\hat{x}$ direction: a $\hat{z}$-directed electric field with a $-\hat{y}$-directed magnetic field and a $\hat{y}$-directed electric field with a $\hat{z}$-directed magnetic field). For frequencies between 1.33GHz and 1.61GHz these modes overlap, indicating polarization-independent behavior. Below

94

1.33GHz, the two modes split, indicating that waves traveling through the medium in the same direction but with different polarizations experience different propagation constants. Thus, the design is polarization dependent below 1.33GHz and is unsuitable for three-dimensional focusing in that frequency range. The contour plots in Fig. 4.2 indicate that the medium also suffers from spatial dispersion over these frequencies, so the multimode behavior simply confirms that this design is best-suited for use above 1.4GHz.
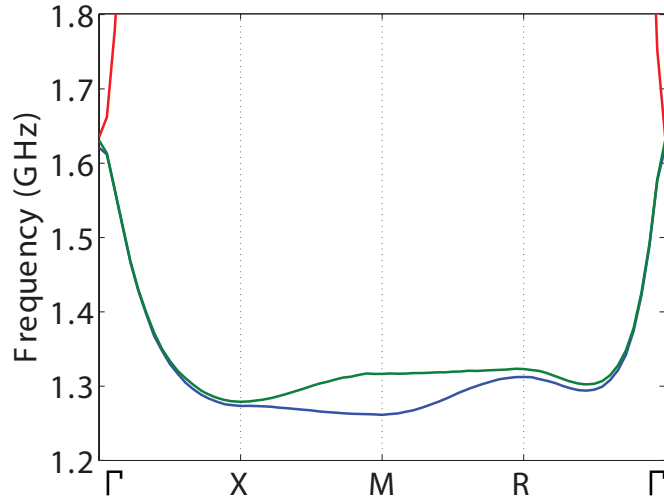
Figure 4.3: Three-dimensional dispersion diagram for the isotropic NRI medium.

Fig. 4.3 illustrates that the overlapping NRI modes are the only modes found between 1.33GHz and 1.61GHz. A previous three-dimensional isotropic structure [18] displayed an undesired mode within the NRI frequency range. Such spurious modes can couple power from the evanescent spectrum. Therefore, ensuring the design is free of spurious modes is of particular importance for near-field applications, such as the NRI lens.

The dispersion diagram also shows the broadband behavior of the proposed NRI medium. For on-axis propagation (Γ to X), the structure exhibits NRI behavior from 1.27GHz to 1.61GHz: a fractional bandwidth of 24.1%. This is more than twice the bandwidth that would be expected of a three-dimensional SRR/wire array and is still

greater than any previously proposed three-dimensional NRI medium [18, 19, 62]. Still more remarkable is the negative permeability bandwidth that is achieved by the SCR arrays. The dispersion diagram for the SCR array without the wire grid (plotted in Fig. 4.4) exhibits a stopband between 1.27GHz and 1.98GHz. This stopband is due to the negative effective permeability of the medium over these frequencies. This represents a fractional negative permeability bandwidth of 43.7%, which is more than four times what can be expected from an array of SRRs.
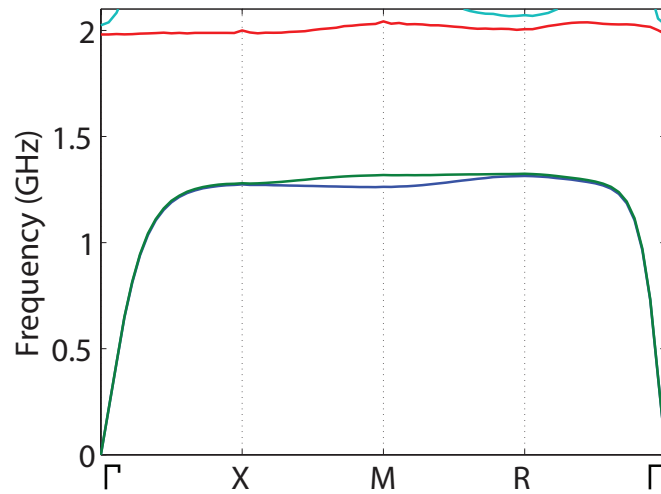
Figure 4.4: Three-dimensional dispersion diagram for the isotropic negative permeability medium.

In Chapter II, the broadband performance of the polarization-dependent NRI and negative permeability media was shown to be a result of strong cell-to-cell coupling. However, unlike the unit cells of the transmission-line cage, the SCRs are not electrically connected to their neighbors. As a result, the cell-to-cell interaction must be achieved through other coupling methods: such as mutual inductance or mutual capacitance. Researchers have coupled SRRs through magnetoinductive waves [27], but the mutual inductance that can be achieved between SRRs in the same plane is small. As a result, the magnetoinductive coupling only resulted in a minor increase in negative permeability bandwidth. On the other hand, strong coupling exists between adjacent SCRs, as depicted in Fig. 4.5(a). Adjacent SCRs are closely spaced and

exhibit a large mutual capacitance between opposing faces. In contrast, only weak capacitive coupling is observed between adjacent SRRs (Fig. 4.5(b)) despite having the same interelement spacing as the SCRs. The significant coupling between neighboring SCRs allows the SCR array to behave as a traveling-wave structure, which results in broadband performance.

(a) Coupling between SCR unit cells.   (b) Coupling between SRR unit cells.
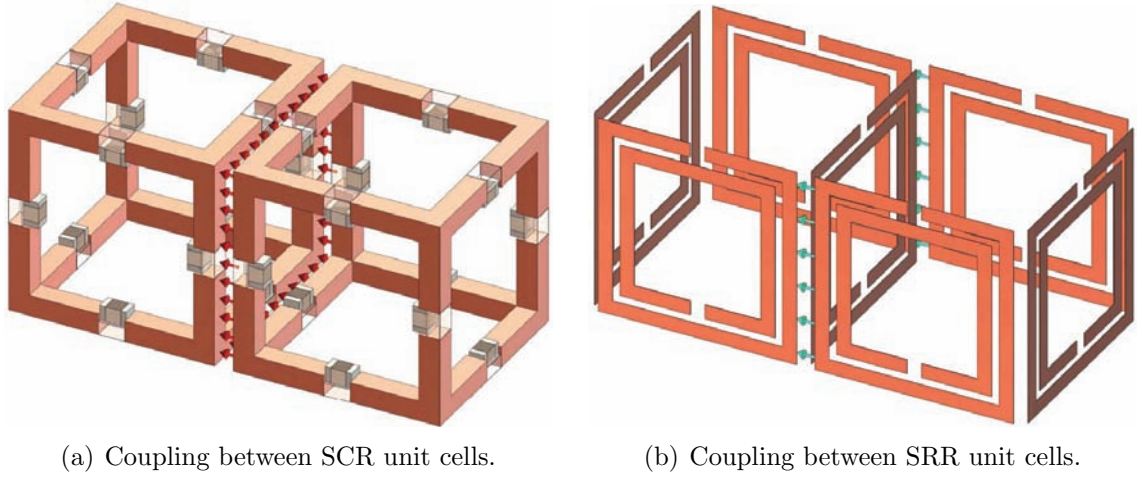
Figure 4.5: Drawings comparing the cell-to-cell capacitive coupling between SCR unit cells and SRR unit cells.

4.1.3   Finite Structure Simulations
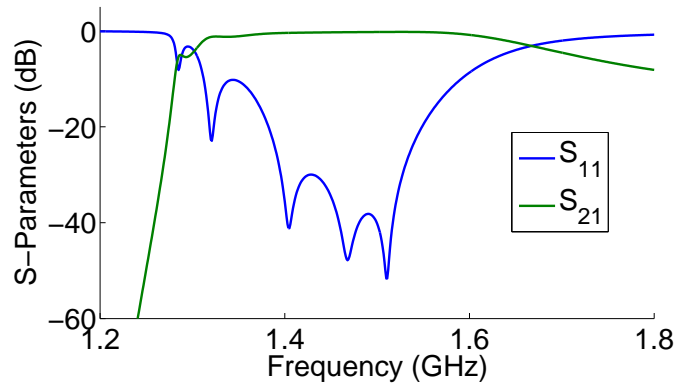
Figure 4.6: Simulated magnitudes of the reflection and transmission coefficients of the NRI slab for normal incidence.

The isotropy and broad bandwidth of the proposed unit cells make them suit-

able for the construction of a three-dimensional NRI lens. As in the case of the polarization-dependent metamaterials designed in Chapter III, the NRI lens was simulated using Ansoft's HFSS. By exciting a four-cell-thick slab of infinite transverse extent with a normally-incident free-space plane wave, the S-parameters of the isotropic NRI medium (Fig. 4.6) were calculated. The refractive index (Fig. 4.7), impedance (Fig. 4.8), loss (Fig. 4.9), Figure of Merit (Fig. 4.10), relative permeability (Fig. 4.11) and permittivity (Fig. 4.12) were all extracted from the simulated S-parameters. The lens was optimized such that $\mu_r \approx \epsilon_r \approx -1$ at the design frequency by adjusting the wire diameters, the capacitor values and the physical dimensions of the SCRs. The dimensions and values of the optimized design are depicted in Fig. 4.1. Due to the availability of only discrete wire sizes and capacitor values, the design frequency shifted marginally to 1.51GHz. At this frequency, the simulated relative permeability and permittivity are $\mu_r = -1.006 - j0.017$ and $\epsilon_r = -1.007 - j0.011$, respectively, leading to an index of refraction of $n = \sqrt{\mu_r \epsilon_r} = -1.006 - j0.014$ and a wave impedance of $\eta = 376.5 + j1.1\Omega$. Since the impedance of the medium is close to that of free space ($\eta_0 = 376.7\Omega$) at the design frequency, the lens is nearly reflectionless, with a simulated reflection coefficient magnitude of $|S_{11}| = -51.6$dB. Furthermore, the S-parameters show that the structure is well matched to free space over a large bandwidth, ranging from 1.31GHz to 1.59GHz.
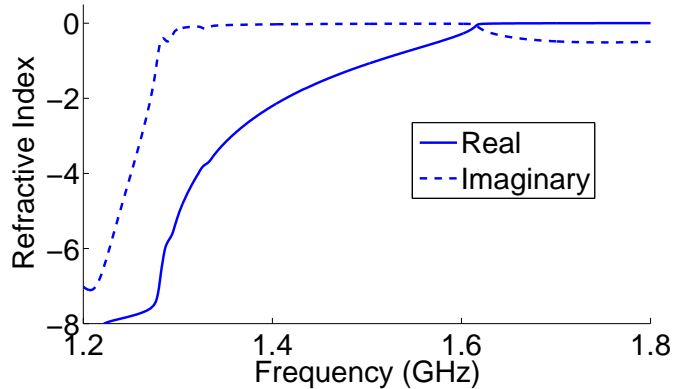
Figure 4.7: The simulated refractive index of the NRI slab extracted from the normal incidence transmission data.
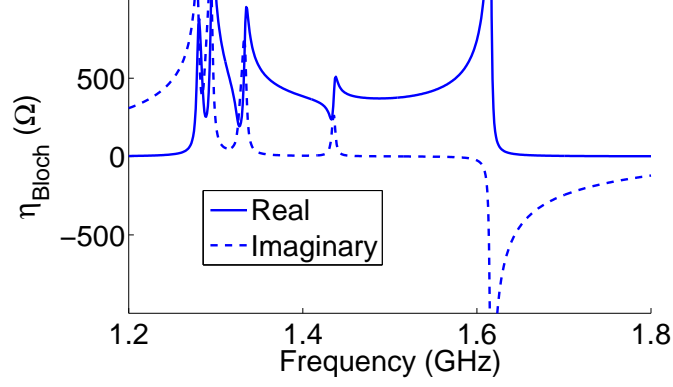
Figure 4.8: The simulated Bloch impedance of the NRI slab extracted from the normal incidence transmission data. The resonances that occur in the lower frequencies are a result of the electrical length of the slab being a multiple of $\lambda/2$.
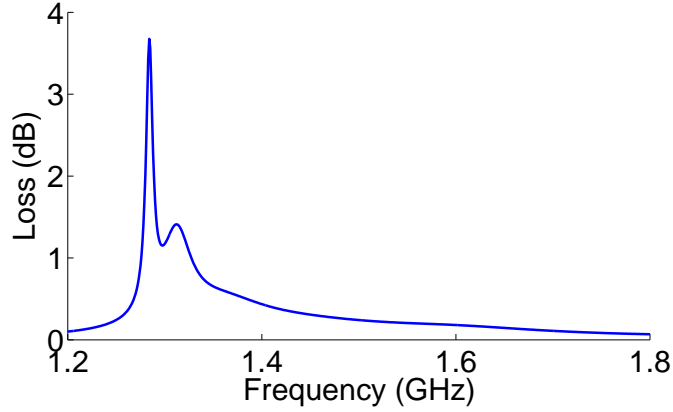
Figure 4.9: The simulated loss of the NRI slab extracted from the normal incidence transmission data.

As can be immediately noticed from Figs. 4.7, 4.9 and 4.10, the structure was low loss, exhibiting a simulated loss of 0.25dB for the entire four cell slab and a Figure of Merit ($|n'/n''|$) equal to 72 at the operating frequency. This loss performance is comparable the simulated structure presented in section 3.2, the experimental version of which exhibited the lowest loss per cell for any NRI medium.

Figs. 4.11 and 4.12 also reveal why a medium with more than 40% negative permeability bandwidth has a NRI bandwidth of just over half of that. The reason for this is that the slope of the permittivity curve at $\epsilon_r = -1$ is much steeper than

99
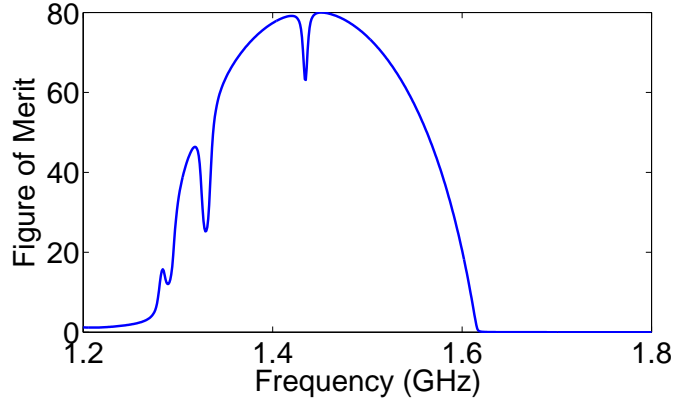
Figure 4.10: The simulated Figure of Merit ($|n'/n''|$) of the NRI slab extracted from the normal incidence transmission data.
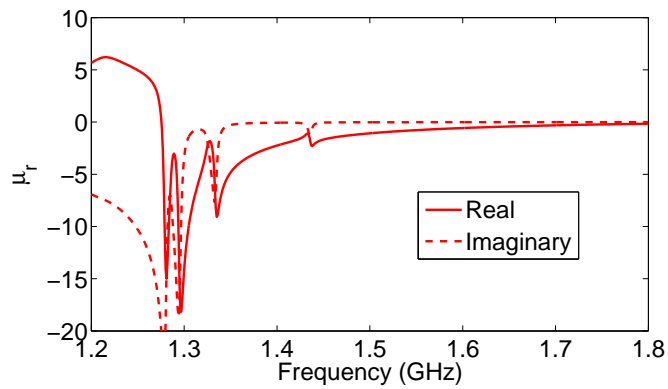
Figure 4.11: The simulated relative permeability of the NRI slab extracted from the normal incidence transmission data.

the slope of the permeability curve at $\mu_r = -1$. As a result, the electric plasma frequency will be well below the magnetic plasma frequency for a medium with the material parameters $\epsilon_r = \mu_r = -1$ at the operating frequency. Fig. 4.12 shows that this was the case for this design. The electric plasma frequency occurs at 1.61GHz, while the magnetic plasma frequency was shown in section 4.1.2 to be 1.98GHz. This bandwidth limitation illustrates the cost of realizing an impedance matched structure on the bandwidth of the NRI medium.
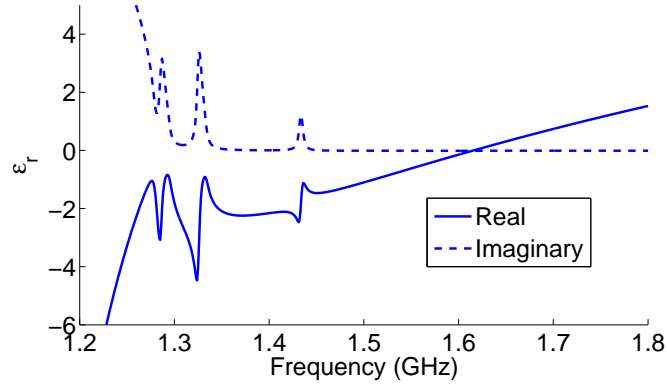
Figure 4.12: The simulated relative permittivity of the NRI slab extracted from the normal incidence transmission data.

4.2 Fabrication of the Isotropic NRI Medium

With the four-cell NRI lens designed, the next challenge was to build the isotropic NRI medium. This challenge was an important one because previously proposed designs of isotropic NRI media were prohibitively difficult to fabricate [18, 19]. The difficulty with earlier structures was primarily caused by their reliance on printed-circuit-board techniques to realize three-dimensional structures. In such structures, the printed circuit boards would be assembled at right angles to each other, requiring extensive manual effort. More importantly, loading circuit components had to be electrically connected across these 90° junctions in both designs. Such connections are not only challenging to execute but are also mechanically unstable, since any flexing of the joints will result in significant stress on the electrical connection. To avoid these issues, the SCRs were fabricated using stereolithography: a fabrication technique that uses a laser to cure plastic resin layer-by-layer in order to construct three-dimensional forms. This fabrication procedure produced a solid cubic frame, which added to the mechanical strength of the isotropic NRI medium rather than compromising it.

The fabrication of each SCR began with the formation of the 13.75mm cubic frame out of plastic (Accura 60 resin) using the stereolithography process. Each leg

of the frame had a cross-sectional area of 50mil×50mil with a notch in the center 70mil long and 20mil deep into which a capacitor was placed when the SCR was complete. The next step was to electroplate the frame with copper. The notches had to remain free from copper, so that they would not short circuit the capacitors that would be placed across them. This was accomplished by masking the surface of these notches during the electroplating process. The frames were subsequently wrapped in wire to ensure uniform copper plating over their surfaces. The frames were plated in batches of 60 using a LPKF MiniContac RS copper plating system. After the electroplating process, the masks were removed from the notches, exposing the bare plastic underneath. The final step of the SCR fabrication was to solder a 1.8pF capacitor into every notch (for a total of 12 capacitors per SCR). A photograph of the cubic frame and a complete SCR is shown in Fig. 4.13.

More than 400 SCRs were fabricated using this process. They were arrayed in a $10 \times 10 \times 4$ lattice to produce a negative permeability medium. A separation of 1.25mm was maintained between the SCRs in all directions by placing the 400 SCRs into ten custom-machined trays made from 4mm Rohacell foam. Arrays of 10×4 SCR-footprints were milled to a depth of 1.375mm in both sides of the Rohacell (Fig 4.14). The double-sided milling allowed each row of SCRs to be locked in proper alignment with the row above and below it. The ten trays were stacked atop each other to create the negative permeability medium. As a result of the low permittivity and loss tangent of the Rohacell ($\epsilon_r = 1.05$, $\tan \delta < 0.0002$), the presence of the trays only slightly perturbed the material parameters of the medium.

Negative permittivity was then introduced by threading 24 AWG (20mil diameter) wires through the unit cells in all three axial directions. As shown in Fig. 4.1, the junctions of the wires were electrically connected. These connections were required in order to maintain NRI behavior when the incident electric field is not aligned with any of the wires. To aid in the mechanical stability of the connections, the wires were
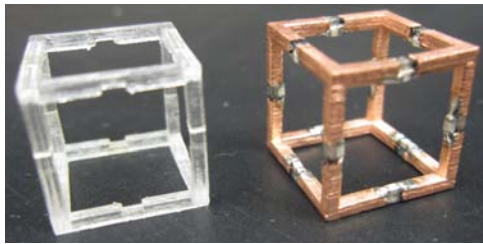
Figure 4.13: A plastic 3-D cubic frame (left) and a completed cube (right).

Figure 4.14: Top-view of one of the Rohacell trays.
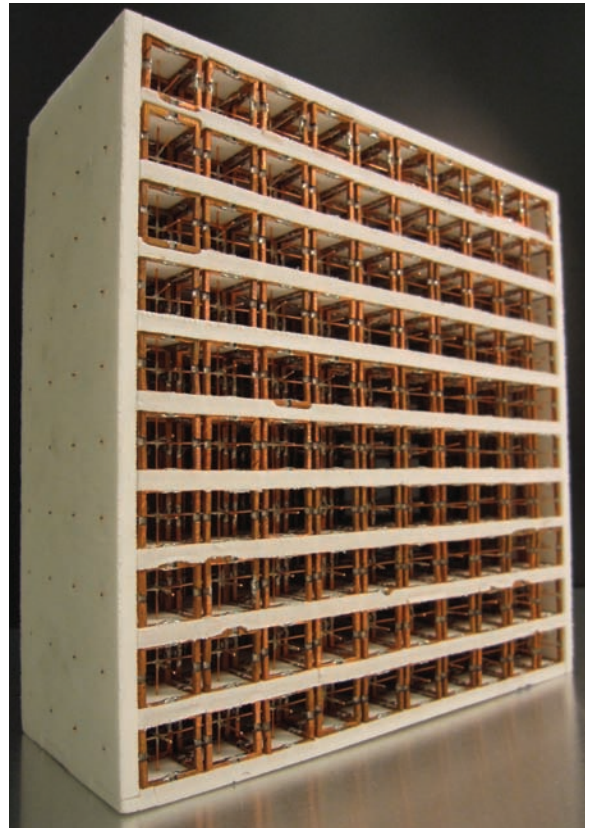
Figure 4.15: Front-view of the completed NRI Lens.

woven together, alternating their over-under pattern every unit cell. This weave kept the wires in place and allowed reliable electrical connections to be achieved at the junctions using silver epoxy. With the integration of the wire grid, the construction of the three-dimensional, isotropic NRI medium (Fig. 4.15) was complete. The fabricated NRI lens measured 15cm×15cm×6cm or $0.75\lambda \times 0.75\lambda \times 0.3\lambda$.

4.2.1 Differences Between the Designed and Fabricated Lens

Any process that is not well-characterized through prior experience will produce some unanticipated results. Electroplating the plastic frames of the SCRs using a printed-circuit-board copper plating system proved to be a challenge in this respect. While it was anticipated that electroplating the cubic frames would increase their thickness, the actual increase was larger than expected. Measurements of the SCR dimensions after the plating process showed that the size of the cubic frame was 13.85mm (compared to anticipated 13.75mm) and the cross-sectional area of each leg increased from 50mil×50mil to 60.5mil×60.5mil.
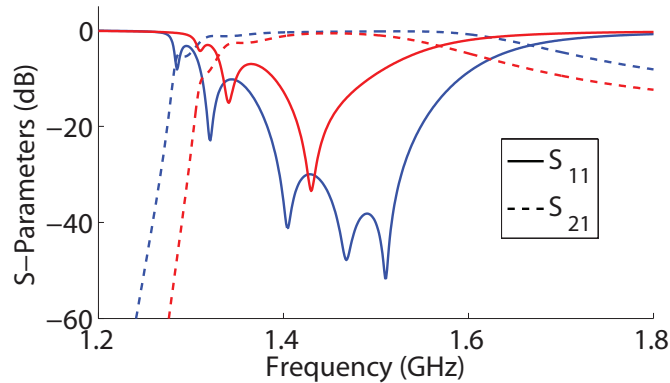
Figure 4.16: Simulated magnitudes of the reflection and transmission coefficients of the NRI slab for normal incidence. The blue curves represent the original design; the red curves more accurately reflect the dimensions of the fabricated structure.

To observe the effects of the added copper thickness on the material parameters of NRI medium, the HFSS simulations of the finite structure were redone using the new

Figure 4.17: The simulated refractive index of the NRI slab extracted from the normal incidence transmission data. The blue curves represent the original design; the red curves more accurately reflect the dimensions of the fabricated structure.

dimensions. The red curves in Fig. 4.16 represent the updated S-parameters of the four-cell slab. For comparison, the S-parameters of the original design are also plotted in Fig. 4.16 and are denoted by the blue curves. Using the S-parameters from both the original and the updated simulations, the refractive index (Fig. 4.17), impedance (Fig. 4.18), loss (Fig. 4.19), Figure of Merit (Fig. 4.20), relative permeability (Fig. 4.21) and permittivity (Fig. 4.22) were calculated for both the original design (blue curves) and the design accounting for the excess copper plating present in the fabricated lens (red curves). Figs. 4.21 and 4.22 best illustrate the effect of over-plating on the material parameters of the medium. The permittivity curve shifted down in frequency due to the thicker legs of the cubic frames as well as reduced space between adjacent SCRs (since the unit cells were still 15mm). The reduced spacing resulted in a higher mutual capacitance between neighboring SCRs and the thicker legs resulted in lower inductances separating those mutual capacitances. The overall consequence of these effects was an increase in the relative permittivity of the medium, similar to the structures reported in [52]. The permeability curve on the other hand shifted higher in frequency due to the overplating of the SCRs. The additional copper thickness lowered the inductance of the cubic frame, which raised both the resonant frequency

105

Figure 4.18: The simulated Bloch impedance of the NRI slab extracted from the normal incidence transmission data. The blue curves represent the original design; the red curves more accurately reflect the dimensions of the fabricated structure. The resonances that occur in the lower frequencies are a result of the electrical length of the slab being a multiple of $\lambda/2$.

of the SCR as well as the magnetic plasma frequency.

Since the material parameters of the NRI lens changed, the operating frequency shifted as well. The permeability of the medium is most critical for achieving super-resolved focusing. Therefore, the new operating point was set to where $\mu_r \approx -1$. At 1.54GHz, the simulated material parameters for the fabricated structure were found to be $\mu_r = -0.994 - j0.027$ and $\epsilon_r = -0.179 - j0.016$. Since the operating point follows the permeability and the permittivity curve shifted in the opposite direction with respect to frequency, the permittivity value deviated significantly from the original design. While this compromised the resolution of the lens, a predictable, super-resolved focus was still expected.

Another difference between the fabricated structure and the original design was the loss. The higher loss observed in the fabricated structure can be attributed to the capacitors not having as high a Q-factor as expected as well as the extra resistance caused by the solder joints, which were not included in the original simulation. In either case, the representative loss can be effectively modeled in simulation by adjusting the shunt resistance of the capacitors from $R = 28.6k\Omega$ (which was used in the
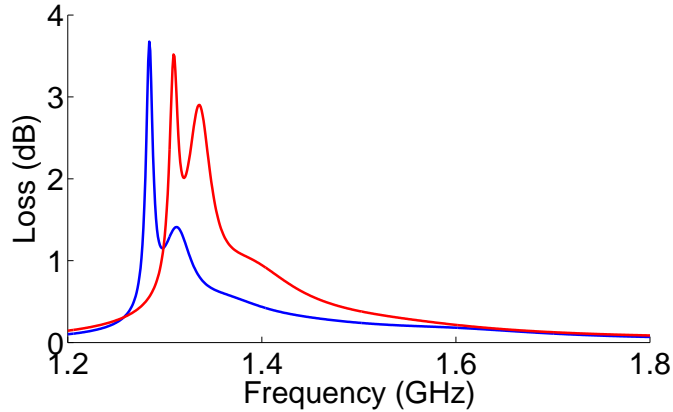
Figure 4.19: The simulated loss of the NRI slab extracted from the normal incidence transmission data. The blue curves represent the original design; the red curves more accurately reflect the dimensions of the fabricated structure.

original design) to $R = 17.7k\Omega$. Both Figs. 4.19 and 4.20 show that the simulated loss of the fabricated structure was higher than in the original design. Despite the difference, the simulation of the fabricated structure still exhibits low-loss performance in these simulations, with a maximum Figure of Merit above 40 (at 1.45GHz) and a loss of about 0.31dB at the operating frequency. It should be noted that the Figure of Merit was 17.2 at the operating point, however this does not reflect an increase in loss (represented by the imaginary part of the index of refraction n'') so much as it does a decrease in the magnitude of the real part of the index of refraction ($|n'|$) which was $|-0.422|$ as a result of the changes in permittivity.

4.3   Setup of the Focusing Experiments

Although the NRI lens did not have sufficient transverse extent to measure the material parameters directly using a quasioptical gaussian beam measurement system as in Chapter III, considerable information can be gained through near-field focusing experiments. The experimental setup for these focusing experiments is similar to the free-space focusing measurements conducted in Chapter III, except this time both electric and magnetic dipoles were used as the sources and probes. As an example,

107
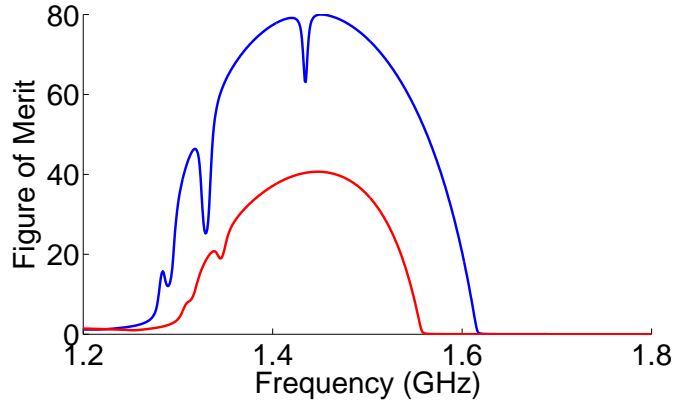
Figure 4.20: The simulated Figure of Merit ($|n'/n''|$) of the NRI slab extracted from the normal incidence transmission data. The blue curves represent the original design; the red curves more accurately reflect the dimensions of the fabricated structure.

a diagram of the experimental setup with electric dipoles can be seen in Fig. 4.23. Regardless of whether electric or magnetic dipole probes are used, the source dipole was located 3cm (half the thickness of the NRI lens) from the input face of the lens, while the second dipole (identical to the source dipole) probed the fields on the opposite side of the lens (i.e. beyond the output face). A three-dimensional translation stage controlled the location of the second dipole, allowing it to be positioned with an accuracy of 5μm. To perform a scan of the fields, the translation stage moved the second dipole probe by 2.5mm intervals, while a computer recorded the complex transmission coefficients measured with an Agilent E8361A network analyzer at each position.

The orientation of the probes depended on whether they were electric or magnetic dipoles. In the case of the electric dipoles (each of which were 2cm or $\lambda_0/10$ in length), the dipole was oriented vertically, as shown in Fig. 4.23. Other polarizations were tested by rotating the lens rather than the dipoles. By rotating the device under test rather than the probes, the surrounding test environment remained constant, producing more reliable results. In the "vertical" lens orientation, the Rohacell trays were stacked vertically, as depicted in Fig. 4.15. The "horizontal" and
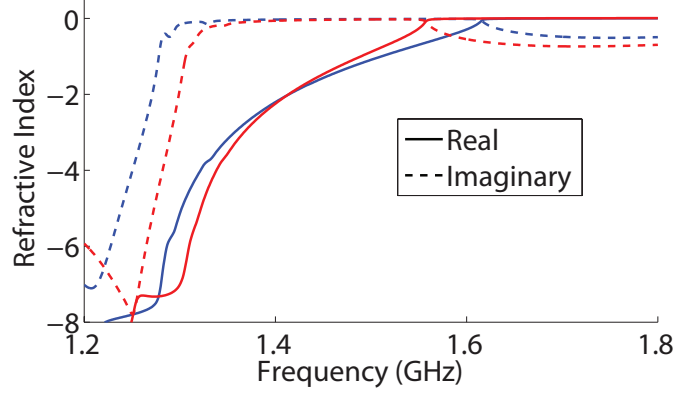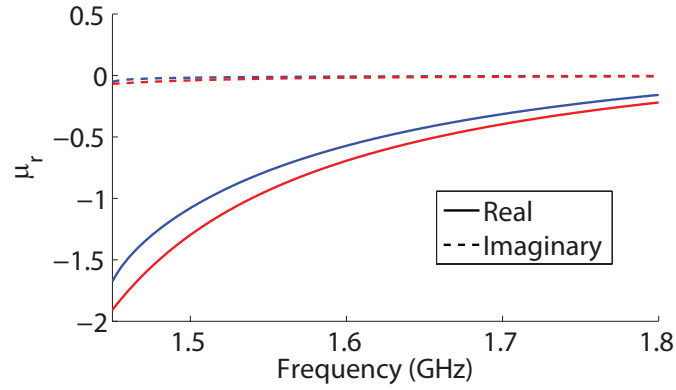
Figure 4.21: The simulated relative permeability of the NRI slab extracted from the normal incidence transmission data. The blue curves represent the original design; the red curves more accurately reflect the dimensions of the fabricated structure.

"off-axis" orientations were tested by rotating the lens 90° and 45°, respectively. The best focusing results were found to occur at 1.54GHz, exactly corresponding to the operating point predicted by the updated simulation. The measured electric field magnitudes at 1.54GHz are plotted in both the horizontal plane (the plane normal to the dipoles that extends beyond the output face of the lens) and the focal plane (the plane parallel to the output face of the lens but 3cm away), in Figs. 4.24(a) and 4.24(b), respectively.

The magnetic dipole probes were implemented as shielded loops. Each loop was approximately 1cm in diameter and made from 1.17mm semirigid coaxial cable. The loops lay in a plane parallel to the face of the NRI lens such that the magnetic dipole (aligned along the axis of the loop) was perpendicular to the face of the lens. Using these magnetic dipole probes, scans were performed in the horizontal plane and the focal plane for the same three polarizations that were tested using the electric dipole probes. The results of these scans are plotted in Fig. 4.25.
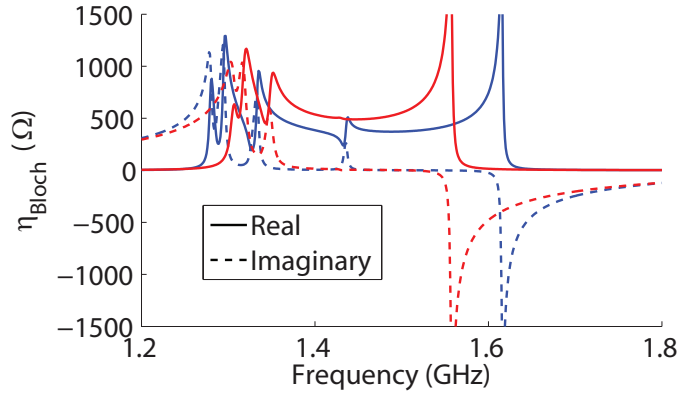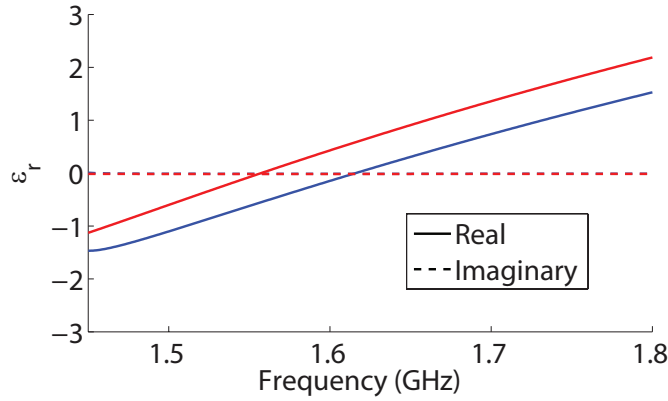
Figure 4.22: The simulated relative permittivity of the NRI slab extracted from the normal incidence transmission data. The blue curves represent the original design; the red curves more accurately reflect the dimensions of the fabricated structure.

4.4 Comparison of the Experimental Results to Theory

Analyzing the focusing results of the NRI lens quantitatively requires theoretical predictions of the expected performance of the NRI lens based on the material parameters extracted from simulation. These predictions were made by deriving the three-dimensional Green's functions for a dipole source in front of a slab with infinite transverse extent and arbitrary material parameters, similar to the procedure derived in [67].

4.4.1 Plane Wave Propagation

In order to derive the complete Green's functions for an infinitesimal source, the behavior for TE and TM plane waves incident on the slab should be characterized. All other waves can be expressed as the superposition of these plane waves, allowing the response of arbitrary sources to be calculated. To start, the expressions for TM waves ($H_z = 0$) will be derived. Equations for TE waves ($E_z = 0$) can then be found by duality.

Consider the diagram in Fig. 4.26. Since the slab has infinite transverse extent, the geometry exhibits cylindrical symmetry with respect to ϕ (although the plane

110
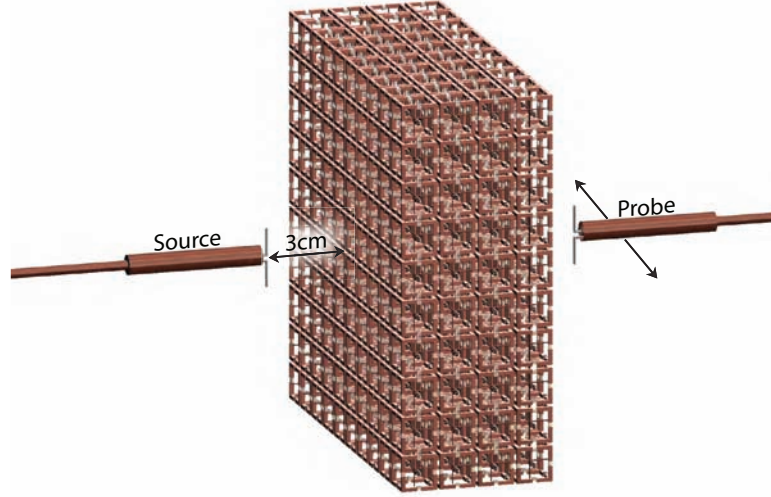
Figure 4.23: Diagram depicting the experimental setup (with electric dipoles) for the measurement of the isotropic NRI lens.

wave does not). However, this symmetry allows the coordinate system to be oriented to best suit the needs of the solution. The value of ϕ can be chosen such that the direction of propagation lies in the $\hat{\rho}$-$\hat{z}$ plane. For the TM waves considered here, this means the magnetic field is always oriented in the $\hat{\phi}$ direction. The electric field vectors are, therefore, defined as

$$\mathbf{E_1^+} = E_0 \left(\hat{\rho} \frac{k_{z0}}{k_0} + \hat{z} \frac{k_\rho}{k_0} \right) \tag{4.1a}$$

$$\mathbf{E_1^-} = R_{TM} \cdot E_0 \left(\hat{\rho} \frac{k_{z0}}{k_0} - \hat{z} \frac{k_\rho}{k_0} \right) \tag{4.1b}$$

$$\mathbf{E_2^+} = T_{TM} \cdot E_0 \left(\hat{\rho} \frac{k_{z2}}{k_2} + \hat{z} \frac{k_\rho}{k_2} \right) \tag{4.1c}$$

$$\mathbf{E_2^-} = (-\Gamma_{TM}) T_{TM} \cdot E_0 \left(\hat{\rho} \frac{k_{z2}}{k_2} - \hat{z} \frac{k_\rho}{k_2} \right) \tag{4.1d}$$

$$\mathbf{E_3^+} = \frac{\eta_0}{\eta_2} (1 + \Gamma_{TM}) T_{TM} \cdot E_0 \left(\hat{\rho} \frac{k_{z0}}{k_0} + \hat{z} \frac{k_\rho}{k_0} \right), \tag{4.1e}$$

where Γ_{TM} is the reflection coefficient seen by a TM plane wave incident from free space onto an infinite half space of the NRI medium (the Fresnel reflection coefficient).
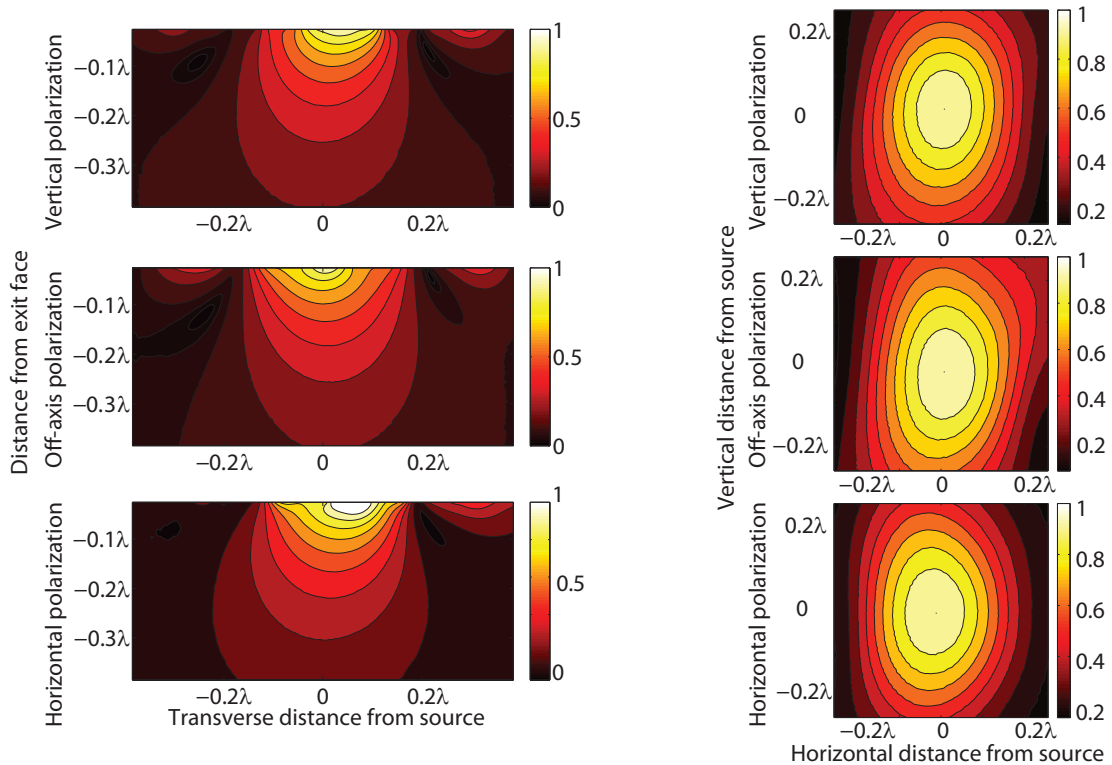
(a) Plots of the measured electric field at 1.54GHz in the horizontal plane.

(b) Plots of the measured electric field at 1.54GHz in the image plane.

Figure 4.24: Normalized electric field magnitudes.
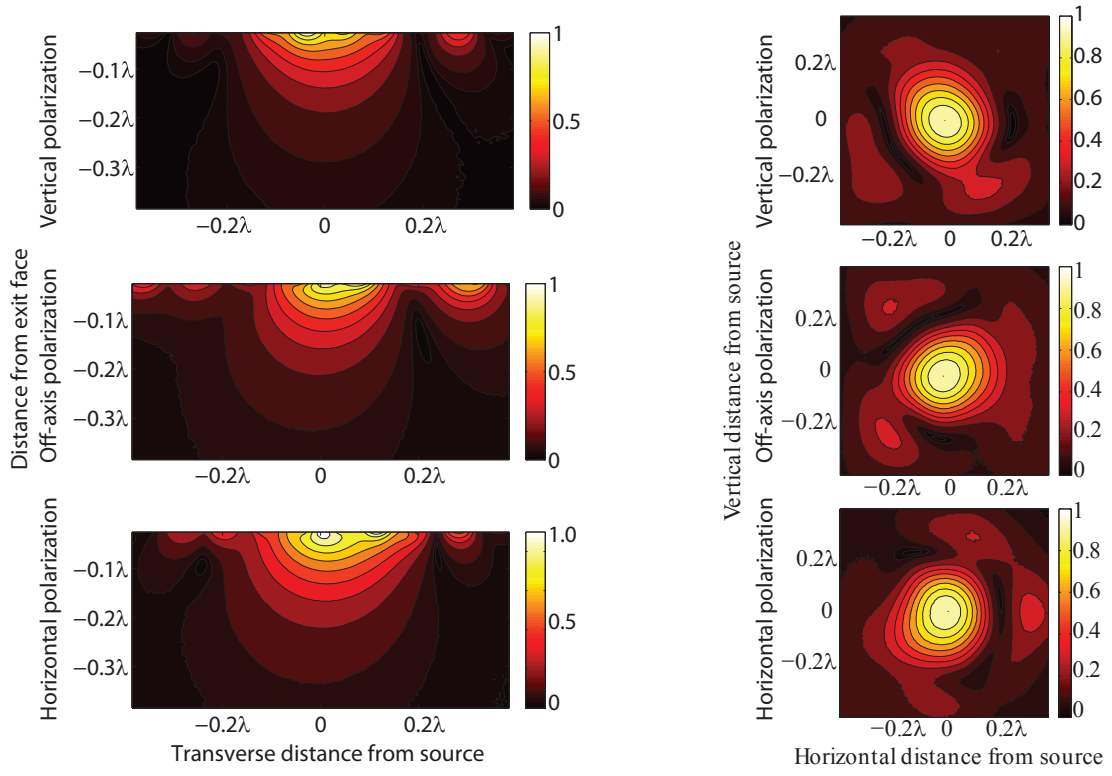
(a) Plots of the measured magnetic field at 1.54GHz in the horizontal plane.

(b) Plots of the measured magnetic field at 1.54GHz in the image plane.

Figure 4.25: Normalized magnetic field measurements.
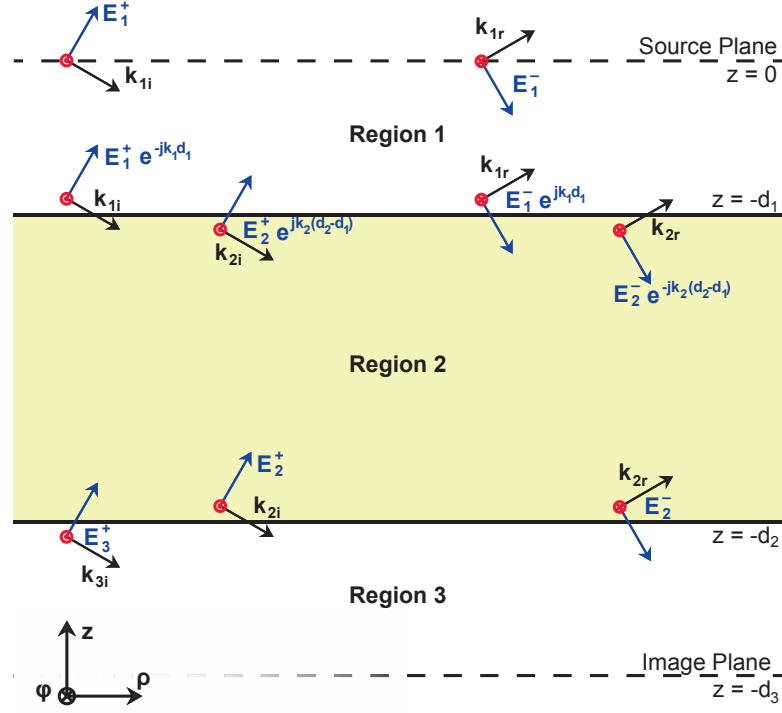
Figure 4.26: Electric field components for the TM plane waves incident on a homogeneous slab with infinite transverse extent.

This can be defined as

$$\Gamma_{TM} = \frac{\epsilon_0 k_{z2} - \epsilon_2 k_{z0}}{\epsilon_0 k_{z2} + \epsilon_2 k_{z0}}. \tag{4.2}$$

The coefficients R_{TM} and T_{TM} relate $|\mathbf{E_1^-}|$ and $|\mathbf{E_2^+}|$ to E_0, respectively. These quantities can be found using the boundary conditions at the first free space/slab interface for the $\hat{\rho}$-components and the $\hat{z}$-components:

$$\frac{k_{z0}}{k_0} E_0 \cdot \left(e^{-jk_{z0}d_1} + R_{TM} e^{jk_{z0}d_1} \right)$$
$$= \frac{k_{z2}}{k_2} T_{TM} E_0 \cdot \left(e^{jk_{z2}(d_2-d_1)} - \Gamma_{TM} e^{-jk_{z2}(d_2-d_1)} \right) \tag{4.3}$$

$$\frac{\epsilon_0 k_\rho}{k_0} E_0 \cdot \left(e^{-jk_{z0}d_1} - R_{TM} e^{jk_{z0}d_1} \right)$$
$$= \frac{\epsilon_2 k_\rho}{k_2} T_{TM} E_0 \cdot \left(e^{jk_{z2}(d_2-d_1)} + \Gamma_{TM} e^{-jk_{z2}(d_2-d_1)} \right) \tag{4.4}$$

114

Solving these equations for R_{TM} and T_{TM} yields

$$R_{TM} = e^{-jk_{z0}\cdot 2d_1} \cdot \frac{\Gamma_{TM} - \Gamma_{TM}e^{-jk_{z2}\cdot 2(d_2-d_1)}}{1 - \Gamma_{TM}^2 e^{-jk_{z2}\cdot 2(d_2-d_1)}} \tag{4.5}$$

$$T_{TM} = e^{-jk_{z0}d_1} \cdot \frac{\tau_{TM}e^{-jk_{z2}(d_2-d_1)}}{1 - \Gamma_{TM}^2 e^{-jk_{z2}\cdot 2(d_2-d_1)}}, \tag{4.6}$$

where τ_{TM} is the transmission coefficient seen by a TM plane wave incident from free space onto an infinite half space of the NRI medium. This can be defined as

$$\tau_{TM} = \frac{2\epsilon_0 k_{z0}}{\epsilon_0 k_{z2} + \epsilon_2 k_{z0}} \cdot \frac{k_2}{k_0}. \tag{4.7}$$

Using Eqs. (4.1), and accounting for propagation in both the $\hat{\rho}$ and $\hat{z}$ directions, a complete description of the electric fields in each of the three regions can be derived:

$$\mathbf{E_1} = e^{-jk_\rho\rho}E_0\left(\hat{\rho}\frac{k_{z0}}{k_0}\left(e^{jk_{z0}z} + R_{TM}e^{-jk_{z0}z}\right) + \hat{z}\frac{k_\rho}{k_0}\left(e^{jk_{z0}z} - R_{TM}e^{-jk_{z0}z}\right)\right) \tag{4.8a}$$

$$\mathbf{E_2} = e^{-jk_\rho\rho}T_{TM}\cdot E_0\left(\hat{\rho}\frac{k_{z2}}{k_2}\left(e^{jk_{z2}(z+d_2)} - \Gamma_{TM}e^{-jk_{z2}(z+d_2)}\right)\right.$$
$$\left. + \hat{z}\frac{k_\rho}{k_2}\left(e^{jk_{z2}(z+d_2)} + \Gamma_{TM}e^{-jk_{z2}(z+d_2)}\right)\right) \tag{4.8b}$$

$$\mathbf{E_3} = e^{-jk_\rho\rho}e^{jk_{z0}(z+d_2)}\frac{\eta_0}{\eta_2}\left(1 + \Gamma_{TM}\right)T_{TM}\cdot E_0\left(\hat{\rho}\frac{k_{z0}}{k_0} + \hat{z}\frac{k_\rho}{k_0}\right). \tag{4.8c}$$

The TE fields ($E_z = 0$) can be found by applying duality to Eqs. (4.8):

$$\mathbf{H_1} = e^{-jk_\rho\rho}H_0\left(\hat{\rho}\frac{k_{z0}}{k_0}\left(e^{jk_{z0}z} + R_{TE}e^{-jk_{z0}z}\right) + \hat{z}\frac{k_\rho}{k_0}\left(e^{jk_{z0}z} - R_{TE}e^{-jk_{z0}z}\right)\right) \tag{4.9a}$$

$$\mathbf{H_2} = e^{-jk_\rho\rho}T_{TE}\cdot H_0\left(\hat{\rho}\frac{k_{z2}}{k_2}\left(e^{jk_{z2}(z+d_2)} - \Gamma_{TE}e^{-jk_{z2}(z+d_2)}\right)\right.$$
$$\left. + \hat{z}\frac{k_\rho}{k_2}\left(e^{jk_{z2}(z+d_2)} + \Gamma_{TE}e^{-jk_{z2}(z+d_2)}\right)\right) \tag{4.9b}$$

$$\mathbf{H_3} = e^{-jk_\rho\rho}\frac{\eta_2}{\eta_0}\left(1 + \Gamma_{TE}\right)T_{TE}e^{jk_{z0}(z+d_2)}\cdot H_0\left(\hat{\rho}\frac{k_{z0}}{k_0} + \hat{z}\frac{k_\rho}{k_0}\right). \tag{4.9c}$$

The TE reflection and transmission coefficients in Eq. (4.9) (also found by duality) are defined as

$$\Gamma_{TE} = \frac{\mu_0 k_{z2} - \mu_2 k_{z0}}{\mu_0 k_{z2} + \mu_2 k_{z0}} \tag{4.10}$$

$$\tau_{TE} = \frac{2\mu_0 k_{z0}}{\mu_0 k_{z2} + \mu_2 k_{z0}} \cdot \frac{k_2}{k_0} \tag{4.11}$$

$$R_{TE} = e^{-jk_{z0} \cdot 2d_1} \cdot \frac{\Gamma_{TE} - \Gamma_{TE} e^{-jk_{z2} \cdot 2(d_2 - d_1)}}{1 - \Gamma_{TE}^2 e^{-jk_{z2} \cdot 2(d_2 - d_1)}} \tag{4.12}$$

$$T_{TE} = e^{-jk_{z0}d_1} \cdot \frac{\tau_{TE} e^{-jk_{z2}(d_2 - d_1)}}{1 - \Gamma_{TE}^2 e^{-jk_{z2} \cdot 2(d_2 - d_1)}}. \tag{4.13}$$

4.4.2   Point Source Excitation

If the NRI lens were excited by a plane wave Eqs. (4.8) and (4.9) would completely describe the fields both inside and outside of the lens. Since the lens is instead excited by a dipole source that is quite close to the lens interface, this difference in excitation must be taken into account. Considering the dipole probes are much smaller than a wavelength ($\lambda_0/10$), they can be approximated as infinitesimal. As a result, the source dipole should radiate a spherical wave. The fields produced by a dipole radiating in front of a slab can be predicted using the Green's functions which describe this situation. The Green's function for a point source radiating at the origin in free space is $e^{-jk_0 r}/(4\pi r)$.

As shown in the previous section, the waves incident on the slab will behave differently depending on the orientations of their fields. Consequently, the spherical wave emitted by the dipole source must be decomposed into TM and TE waves. Only the TM waves have a non-zero E_z component, so the E_z component of the electric field uniquely determines all the field components of the TM waves. For an electric dipole source oriented in the $\hat{x}$ direction, the E_z component is defined as

$$E_z = \frac{-jIl}{4\pi\omega\epsilon} \cdot \frac{\partial^2}{\partial z \partial x} \frac{e^{-jkr}}{r}. \tag{4.14}$$

116

Similarly, the TE modes are defined by the H_z component radiated by the dipole:

$$H_z = \frac{-Il}{4\pi} \cdot \frac{\partial}{\partial y} \frac{e^{-jkr}}{r}. \tag{4.15}$$

The next step is to consider the effects of the slab on these fields. These effects have been characterized in the previous section for plane waves, but Eqs. (4.14) and (4.15) are spherical waves. To address this issue, the Sommerfeld identity [67] can be used to represent the free-space Green's function as an integral of cylindrical waves

$$\frac{e^{-jkr}}{r} = -j \int_0^\infty \frac{k_\rho}{k_z} J_0\left(k_\rho \rho\right) e^{-jk_z|z|} dk_\rho. \tag{4.16}$$

Substituting Eq. (4.16) into Eqs. (4.14) and (4.15) yields:

$$E_z = \frac{-Il}{4\pi\omega\epsilon} \int_0^\infty \frac{k_\rho}{k_z} \frac{\partial}{\partial x} J_0\left(k_\rho \rho\right) \frac{\partial}{\partial z} e^{-jk_z|z|} dk_\rho \tag{4.17}$$

$$H_z = \frac{jIl}{4\pi} \int_0^\infty \frac{k_\rho}{k_z} \frac{\partial}{\partial y} J_0\left(k_\rho \rho\right) e^{-jk_z|z|} dk_\rho. \tag{4.18}$$

The chain rule can be used to take the Cartesian derivatives of the quantities in cylindrical coordinates:

$$\frac{\partial}{\partial x} = \frac{\partial \rho}{\partial x} \frac{\partial}{\partial \rho} \tag{4.19a}$$

$$\frac{\partial}{\partial y} = \frac{\partial \rho}{\partial y} \frac{\partial}{\partial \rho}. \tag{4.19b}$$

In Cartesian coordinates, ρ is written as

$$\rho = \sqrt{x^2 + y^2}, \tag{4.20}$$

so

$$\frac{\partial \rho}{\partial x} = \frac{x}{\sqrt{x^2 + y^2}} = \frac{x}{\rho} \tag{4.21a}$$

$$\frac{\partial \rho}{\partial y} = \frac{y}{\sqrt{x^2 + y^2}} = \frac{y}{\rho}. \tag{4.21b}$$

In cylindrical coordinates,

$$x = \rho \cos \phi \tag{4.22a}$$

$$y = \rho \sin \phi. \tag{4.22b}$$

Substituting Eq. (4.22) into Eq. (4.21) and simplifying yields

$$\frac{\partial \rho}{\partial x} = \cos \phi \tag{4.23a}$$

$$\frac{\partial \rho}{\partial y} = \sin \phi. \tag{4.23b}$$

After performing the derivatives, the TM and TE fields radiated by a $\hat{x}$-directed infinitesimal electric dipole in free space are completely defined by:

$$E_z = \begin{cases} -\frac{jIl\cos\phi}{4\pi\omega\epsilon} \int_0^\infty k_\rho^2 J_1\left(k_\rho\rho\right) e^{-jk_z z} dk_\rho & z > 0 \\ \frac{jIl\cos\phi}{4\pi\omega\epsilon} \int_0^\infty k_\rho^2 J_1\left(k_\rho\rho\right) e^{jk_z z} dk_\rho & z < 0 \end{cases} \tag{4.24}$$

$$H_z = \frac{-jIl\sin\phi}{4\pi} \int_0^\infty \frac{k_\rho^2}{k_z} J_1\left(k_\rho\rho\right) e^{-jk_z|z|} dk_\rho. \tag{4.25}$$

With the radiated fields in this form, accounting for the reflection from and transmission through the interfaces of the slab is straightforward. The reflection and transmission coefficients at these interfaces are the same as those derived for the plane waves in the previous section. The $\hat{z}$-directed electric fields are written as

follows:

$$E_{z0} = -\frac{jIl\cos\phi}{4\pi\omega\epsilon_0}\int_0^\infty k_\rho^2 \cdot (1 + R_{TM})\, e^{-jk_{z0}z} J_1\left(k_\rho\rho\right) dk_\rho \tag{4.26a}$$

$$E_{z1} = \frac{jIl\cos\phi}{4\pi\omega\epsilon_0}\int_0^\infty k_\rho^2 \left(e^{jk_{z0}z} - R_{TM}e^{-jk_{z0}z}\right) \cdot J_1\left(k_\rho\rho\right) dk_\rho \tag{4.26b}$$

$$E_{z2} = \frac{jIl\cos\phi}{4\pi\omega\epsilon_2}\int_0^\infty k_\rho^2 T_{TM} \left(e^{jk_{z2}(z+d_2)} + \Gamma_{TM}e^{-jk_{z2}(z+d_2)}\right) \cdot J_1\left(k_\rho\rho\right) dk_\rho \tag{4.26c}$$

$$E_{z3} = \frac{jIl\cos\phi}{4\pi\omega\epsilon_0}\int_0^\infty k_\rho^2 \frac{\eta_0}{\eta_2} \left(1 + \Gamma_{TM}\right) T_{TM}e^{jk_{z0}(z+d_2)} \cdot J_1\left(k_\rho\rho\right) dk_\rho, \tag{4.26d}$$

where E_{zi} is the E_z component in the ith region as depicted in Fig. 4.26. Note that a new region, "Region 0", has been defined in the case of the point source excitation. Region 0 is the region above the source plane $(z > 0)$ and was previously regarded as part of Region 1. However, since the source fields must propagate away from the dipole, Region 1 was split to allow the source fields to propagate in the $+\hat{z}$ direction for values of $z > 0$.

The $\hat{z}$-directed magnetic fields which describe the TE fields of the electric dipole are found in the same manner, except using the TE reflection and transmission coefficients. The H_z components in the different regions of Fig. 4.26 are:

$$H_{z1} = \frac{-jIl\sin\phi}{4\pi}\int_0^\infty \frac{k_\rho^2}{k_{z0}} \left(e^{-jk_{z0}|z|} - R_{TE}e^{-jk_{z0}z}\right) \cdot J_1\left(k_\rho\rho\right) dk_\rho \tag{4.27a}$$

$$H_{z2} = \frac{-jIl\sin\phi}{4\pi}\int_0^\infty \frac{k_\rho^2}{k_{z2}} T_{TE} \left(e^{jk_{z2}(z+d_2)} + \Gamma_{TE}e^{-jk_{z2}(z+d_2)}\right) \cdot J_1\left(k_\rho\rho\right) dk_\rho \tag{4.27b}$$

$$H_{z3} = \frac{-jIl\sin\phi}{4\pi}\int_0^\infty \frac{k_\rho^2}{k_{z0}} \frac{\eta_2}{\eta_0} \left(1 + \Gamma_{TE}\right) T_{TE}e^{jk_{z0}(z+d_2)} \cdot J_1\left(k_\rho\rho\right) dk_\rho. \tag{4.27c}$$

Eqs. (4.26) and (4.27) allow all the remaining field components to be derived, however at this point, attention will be given only to the field quantities that will be measured experimentally. As explained in section 4.3, the probe will scan only the fields on the opposite side of the lens from the probe (Region 3). Further, since the probe dipole will be oriented the same as the source dipole, only the $\hat{x}$-directed electric

119

fields will ultimately be measured. To find the E_{x3} field component, the electric fields parallel to the lens interface must be derived. These fields are given by the expression [67]

$$\mathbf{E}_{\parallel} = \int_0^{\infty} \frac{1}{k_\rho^2} \left(\nabla_{\parallel} \frac{\partial e_z}{\partial z} + j\omega\mu\hat{z} \times \nabla_{\parallel} h_z \right) dk_\rho \qquad (4.28)$$

where e_z and h_z are the integrands of Eqs. (4.26) and (4.27), respectively, and

$$\nabla_{\parallel} = \hat{x} \frac{\partial}{\partial x} + \hat{y} \frac{\partial}{\partial y} \qquad (4.29a)$$

$$= \hat{\rho} \frac{\partial}{\partial \rho} + \hat{\phi} \frac{1}{\rho} \frac{\partial}{\partial \phi}. \qquad (4.29b)$$

Since e_z and h_z are in cylindrical coordinates already, the cylindrical definition of $\nabla_{\parallel}$ will be used. In Region 3, the parallel electric fields are

$$\mathbf{E}_{\parallel 3} = \frac{jIl\omega\mu_0}{4\pi} \int_0^{\infty} \left(\frac{\eta_0}{\eta_2 k_0^2} (1 + \Gamma_{TM}) T_{TM} \cdot \frac{\partial e^{jk_{z0}(z+d_2)}}{\partial z} \nabla_{\parallel} \cos\phi J_1(k_\rho\rho) \right.$$
$$\left. - \frac{j\eta_2}{\eta_0 k_{z0}} (1 + \Gamma_{TE}) T_{TE} e^{jk_{z0}(z+d_2)} \cdot \hat{z} \times \nabla_{\parallel} \sin\phi J_1(k_\rho\rho) \right) dk_\rho. \qquad (4.30)$$

$$= \frac{-Il\omega\mu_0}{4\pi} \int_0^{\infty} e^{jk_{z0}(z+d_2)}$$
$$\cdot \left(\frac{k_{z0}\eta_0}{k_0^2\eta_2} (1 + \Gamma_{TM}) T_{TM} \cdot \left(\hat{\rho} \cos\phi \frac{\partial}{\partial\rho} J_1(k_\rho\rho) + \hat{\phi} \frac{J_1(k_\rho\rho)}{\rho} \frac{\partial \cos\phi}{\partial\phi} \right) \right.$$
$$\left. - \frac{\eta_2}{\eta_0 k_{z0}} (1 + \Gamma_{TE}) T_{TE} \cdot \left(\hat{\phi} \sin\phi \frac{\partial}{\partial\rho} J_1(k_\rho\rho) - \hat{\rho} \frac{J_1(k_\rho\rho)}{\rho} \frac{\partial \sin\phi}{\partial\phi} \right) \right) dk_\rho. \qquad (4.31)$$

The individual field components are given by:

$$E_{\rho 3} = \frac{-Il\omega\mu_0 \cos\phi}{4\pi} \int_0^{\infty} e^{jk_{z0}(z+d_2)}$$
$$\cdot \left(\frac{k_\rho k_{z0}\eta_0}{2k_0^2\eta_2} (1 + \Gamma_{TM}) T_{TM} \cdot (J_0(k_\rho\rho) - J_2(k_\rho\rho)) \right. \qquad (4.32a)$$
$$\left. + \frac{\eta_2}{\rho k_{z0}\eta_0} (1 + \Gamma_{TE}) T_{TE} \cdot J_1(k_\rho\rho) \right) dk_\rho$$

and

$$E_{\phi 3} = \frac{Il\omega\mu_0 \sin\phi}{4\pi} \int_0^\infty e^{jk_{z0}(z+d_2)}$$

$$\cdot \left(\frac{k_{z0}\eta_0}{\rho k_0^2 \eta_2} \left(1 + \Gamma_{TM}\right) T_{TM} \cdot J_1\left(k_\rho\rho\right) \right. \tag{4.32b}$$

$$\left. + \frac{k_\rho\eta_2}{2k_{z0}\eta_0} \left(1 + \Gamma_{TE}\right) T_{TE} \cdot \left(J_0\left(k_\rho\rho\right) - J_2\left(k_\rho\rho\right)\right) \right) dk_\rho.$$

Figure 4.27: Theoretical electric field at the image plane for a electric dipole source in front of a homogeneous slab with infinite transverse extent.

Ultimately, the field vectors will be most useful in the cartesian form. The conversion between the cylindrical and cartesian coordinates is given by

$$E_x = E_\rho \cos\phi - E_\phi \sin\phi \tag{4.33a}$$

$$E_y = E_\rho \sin\phi + E_\phi \cos\phi. \tag{4.33b}$$

The actual electric fields measured in Fig. 4.24(b) are oriented in the same direction as the source dipole. Since the source was assumed to be $\hat{x}$-polarized in this discussion, the desired component is E_x. The final expression for the $\hat{x}$-directed electric fields at

121

the image plane $(z = -d_3)$ are given by the expression

$$
\begin{aligned}
E_x|_{z=-d_3} = & \frac{-Il\omega\mu_0}{4\pi} \int_0^\infty e^{jk_{z0}(d_2-d_1-d_3)}e^{-jk_{z2}(d_2-d_1)} \\
& \cdot \left(\cos^2\phi \cdot \left(\frac{k_\rho k_{z0}\eta_0}{2k_0^2\eta_2} \cdot \frac{(1+\Gamma_{TM})\tau_{TM}}{1-\Gamma_{TM}^2 e^{-jk_{z2}\cdot 2(d_2-d_1)}} \cdot (J_0(k_\rho\rho) - J_2(k_\rho\rho)) \right. \right. \\
& \left. + \frac{\eta_2}{\rho k_{z0}\eta_0} \cdot \frac{(1+\Gamma_{TE})\tau_{TE}}{1-\Gamma_{TE}^2 e^{-jk_{z2}\cdot 2(d_2-d_1)}} \cdot J_1(k_\rho\rho) \right) \\
& + \sin^2\phi \cdot \left(\frac{k_{z0}\eta_0}{\rho k_0^2\eta_2} \cdot \frac{(1+\Gamma_{TM})\tau_{TM}}{1-\Gamma_{TM}^2 e^{-jk_{z2}\cdot 2(d_2-d_1)}} \cdot J_1(k_\rho\rho) \right. \\
& \left. \left. + \frac{k_\rho\eta_2}{2k_{z0}\eta_0} \cdot \frac{(1+\Gamma_{TE})\tau_{TE}}{1-\Gamma_{TE}^2 e^{-jk_{z2}\cdot 2(d_2-d_1)}} \cdot (J_0(k_\rho\rho) - J_2(k_\rho\rho)) \right) \right) dk_\rho.
\end{aligned}
$$

(4.34)

The electric field that should theoretically be measured at the image plane is shown in Fig. 4.27. Qualitatively, the measurements are very similar to the predicted fields. Both display an elliptical pattern with the major axis aligned with the electric dipole. Without the theoretical plot, one might think that such a pattern was a result of the finite size of the dipole probes. However, the predicted fields were produced by an infinitesimal dipole, and they still exhibit the same elliptical shape.

4.4.3 Magnetic Field Plots

For the scans conducted using the magnetic dipole probes, the magnetic dipole source was polarized perpendicular to the face of the lens ($\hat{z}$-polarized for the co-ordinate system describe in Fig. 4.26). This orientation of source excites the TE polarization exclusively. Since the probe in this measurement was also a magnetic dipole with the same orientation as the source, only the $\hat{z}$-component of the magnetic field (H_z) will be measured. These facts greatly simplify the analysis since only the TE polarized fields need to be calculated and the parallel components need not be found. For the magnetic dipole source described above, H_z is given by the equation

122

$$H_z = \frac{-\omega\epsilon I_m l}{4\pi k^2} \int_0^\infty \left(k^2 + \frac{\partial^2}{\partial z^2}\right)^2 \frac{k_\rho}{k_z} J_0\left(k_\rho\rho\right) e^{jk_z z} dk_\rho \tag{4.35}$$

Performing the derivatives and simplifying the equations yields

$$H_z = \frac{-I_m l}{4\pi\omega\mu} \int_0^\infty \frac{k_\rho^3}{k_z} J_0\left(k_\rho\rho\right) e^{jk_z z} dk_\rho. \tag{4.36}$$

The presence of the slab can then be accounted for by including the effects of the reflections from and transmission through the interfaces of the slab. As in Eq. (4.9), different regions are described by different formulae:

$$H_{z1} = \frac{-I_m l}{4\pi\omega\mu_0} \int_0^\infty \frac{k_\rho^3}{k_{z0}} \left(e^{-jk_{z0}|z|} - R_{TE}e^{-jk_{z0}z}\right) \cdot J_0\left(k_\rho\rho\right) dk_\rho \tag{4.37a}$$

$$H_{z2} = \frac{-I_m l}{4\pi\omega\mu_2} \int_0^\infty \frac{k_\rho^3}{k_{z2}} T_{TE} \left(e^{jk_{z2}(z+d_2)} + \Gamma_{TE}e^{-jk_{z2}(z+d_2)}\right) \cdot J_0\left(k_\rho\rho\right) dk_\rho \tag{4.37b}$$

$$H_{z3} = \frac{-I_m l}{4\pi\omega\mu_0} \int_0^\infty \frac{k_\rho^3}{k_{z0}} \frac{\eta_2}{\eta_0} \left(1 + \Gamma_{TE}\right) T_{TE} e^{jk_{z0}(z+d_2)} \cdot J_0\left(k_\rho\rho\right) dk_\rho. \tag{4.37c}$$
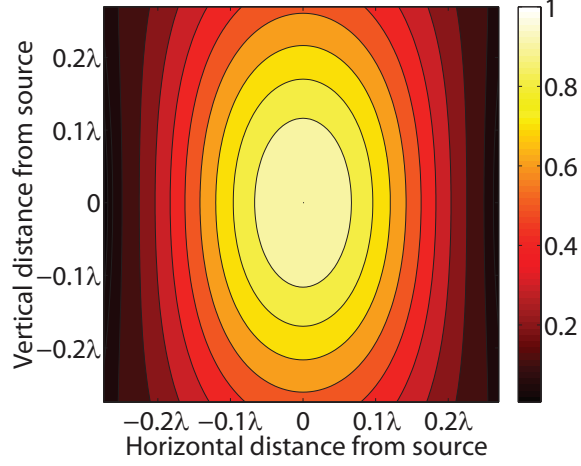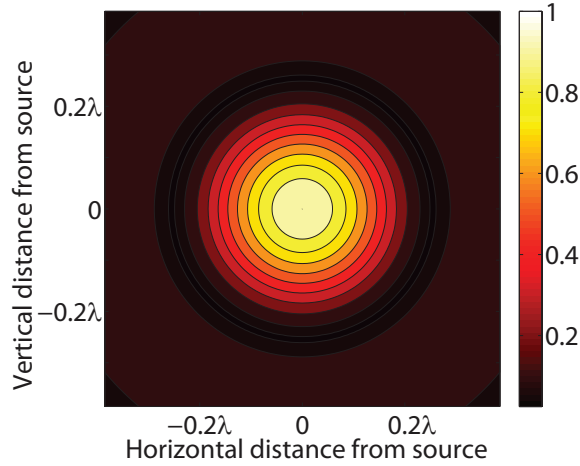

Figure 4.28: Theoretical magnetic field at the image plane for a magnetic dipole source in front of a homogeneous slab with infinite transverse extent.

Substituting in the expression for T_{TE}, the theoretical magnetic fields at the image

plane of the lens are given by

$$H_{z3}|_{z=-d_3} = \frac{-I_m l \eta_2}{4\pi\omega\mu_0\eta_0} \int_0^\infty e^{jk_{z0}(d_2-d_1-d_3)} e^{-jk_{z2}(d_2-d_1)} \frac{k_\rho^3}{k_{z0}} \left(1+\Gamma_{TE}\right)$$
$$\cdot \frac{\tau_{TE}}{1-\Gamma_{TE}^2 e^{-jk_{z2}\cdot 2(d_2-d_1)}} \cdot J_0\left(k_\rho\rho\right) dk_\rho. \quad (4.38)$$

Fig. 4.28 shows a plot of the theoretical magnetic field at the image plane of a NRI lens with the material parameters obtained through full-wave simulation. As can be seen from Eq. (4.38), the magnetic field is independent of ϕ, resulting in the circular pattern at the image plane seen in Fig. 4.28.

The measured plots displayed in Fig. 4.25(b) are not quite as radially symmetric, particularly around the edges of the lens. One explanation for this is the finite nature of the lens. At the boundaries of the lens, the material parameters will abruptly change from a negative refractive index to the index of air. Since the theoretical plots assume infinite transverse extent, the effects of the these boundaries are not accounted for in Fig. 4.28. A second explanation is the variation in the unit cell geometries throughout the lens. As mentioned above, the SCRs were over-plated and exhibited more loss than expected, but some SCRs were plated thicker than others. In constructing the NRI lens, the optimal SCRs were selected to be in the center of the lens, so the focus would be as consistent with simulation as possible. Those SCRs that had less consistent properties were relegated to the fringes of the lens. Particular evidence for this explanation can be seen in Fig. 4.25(b) by tracking the anomalous fields as the polarization is varied. In the vertical polarization, a region of higher-than-expected field magnitude can be seen at the bottom of the scan. For the horizontal polarization, this region moved to the right side of the scan: corresponding to the same rotation experienced by the lens. For the off-axis polarization, the same region of high field amplitude can be seen in the lower-left corner, again aligning with the rotation of the lens. Despite these anomalous fields at the edges of the lens, the

124

fields at the focus of the lens are almost perfectly circular, as predicted by Eq. (4.38).

4.5 Comparison of Experiment with Theory

To provide a more quantitative comparison between theory and experiment, it is useful to examine the half-power beamwidths, otherwise know as the full-widths at half-maximum (FWHM). However, before comparing theory and experiment, the measurements of the FWHM for different polarizations will also be compared. For the horizontal, vertical and off-axis polarizations, the electric field magnitude at the focal plane is plotted with respect to the horizontal distance from the source in Fig. 4.29. The half-power beamwidths were measured to be 0.238λ for the vertical polarization, 0.241λ for the horizontal polarization and 0.241λ for the off-axis polarization: all of which are significantly below the diffraction-limited half-power beamwidth of 0.40λ. These subwavelength focusing results demonstrate that the medium exhibits a negative index of refraction independent of the polarization of the source. Further, since the electric field patterns and the half-power beamwidths of all polarizations are nearly identical (differing by 1.2%), the medium is fully isotropic at the operating frequency.

To compare these experimental results with theoretical ones, Eq. (4.34) was evaluated along the same horizontal ($\hat{y}$-directed) line in the focal plane:

$$
\begin{aligned}
E_x|_{\phi=90^\circ,z=-d3} = &\frac{-Il\omega\mu_0}{4\pi} \int_0^\infty e^{jk_{z0}(d_2-d_1-d_3)} e^{-jk_{z2}(d_2-d_1)} \\
&\left(\frac{k_{z0}\eta_0}{\rho k_0^2 \eta_2} \cdot \frac{(1+\Gamma_{TM})\tau_{TM}}{1-\Gamma_{TM}^2 e^{-jk_{z2}\cdot 2(d_2-d_1)}} \cdot J_1(k_\rho\rho) \right. \\
&\left. + \frac{k_\rho\eta_2}{2k_{z0}\eta_0} \cdot \frac{(1+\Gamma_{TE})\tau_{TE}}{1-\Gamma_{TE}^2 e^{-jk_{z2}\cdot 2(d_2-d_1)}} \cdot (J_0(k_\rho\rho) - J_2(k_\rho\rho)) \right) dk_\rho.
\end{aligned}
\tag{4.39}
$$

The theoretically predicted electric field magnitudes given by Eq. (4.39) are overlaid with the experimental curves in Fig. 4.29 and show close agreement. The theoretical half-power beamwidth for the electric field measurements is 0.238λ. This is
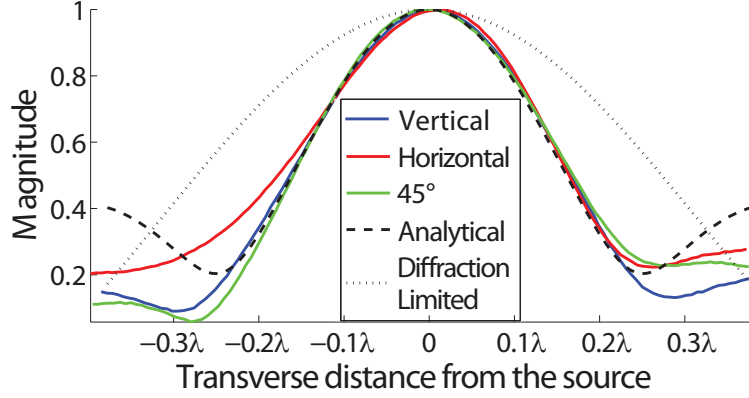
Figure 4.29: Normalized focal patterns for three different orientations of the NRI lens. These are compared with an analytical curve and a diffraction-limited curve which are predicted by the integration of the Green's functions of a dipole above a slab.

less than a 0.9% difference from the average measured beamwidth. The diffraction-limited curve can also be calculated theoretically. To do this, the integral in Eq. (4.39) is used with a few differences. The first change is that the material parameters are set to be those of an ideal NRI slab ($\mu_r = \epsilon_r = -1$) to ensure that the propagating waves are being correctly focused. The second change is to alter how the evanescent spatial frequencies are handled. All spatial frequencies greater than the free-space wave number ($k_\| > k_0$) were integrated such that these evanescent waves decayed exponentially away from the source, as in a conventional medium. The result of this modified integral produces the diffraction-limited curve, which is shown as the dotted line in Fig. 4.29. The wide beamwidth of this curve compared to the beamwidths of the experimental curves demonstrates that the evanescent fields are indeed recovered by the experimental NRI lens.

The same comparison was preformed using the magnetic dipole probes. The normalized magnetic field magnitudes are plotted along a horizontal line 3cm away from the lens (at the focal plane) in Fig. 4.30. The labels denoting the lens orientations are consistent with those used in Fig. 4.29. The half-power beamwidths of the three orientations are nearly identical: 0.204λ for the vertical orientation, 0.207λ for

126

the horizontal orientation and 0.204λ for the off-axis orientation. All of the measured beamwidths are significantly narrower than the diffraction-limited beamwidth of 0.4λ. This result verifies that the super-resolving capabilities of the lens are not only independent of polarization and direction but also the type of source.

To find the predicted magnetic field magnitudes, Eq. (4.38) could be used without modification due to its ϕ independence. Using the same material parameters as in the theoretical plots for the electric dipoles ($\mu_r = -0.994 - j0.027$ and $\epsilon_r = -0.179 - j0.016$), the expected magnetic field magnitude at the focal plane was plotted in Fig. 4.30, and it exhibits close agreement with the measured curves. The theoretical curve has a half-power beamwidth of 0.210λ and difference of 2.4% from the average value of the experimental curves. Using the same modifications used in the electric field case, the diffraction-limited curve for a magnetic dipole source perpendicular to the lens interface is calculated and plotted in Fig. 4.30. The theoretical diffraction-limited pattern for the magnetic field is 0.40λ, verifying that the lens provided super-resolved focusing at the operating point.
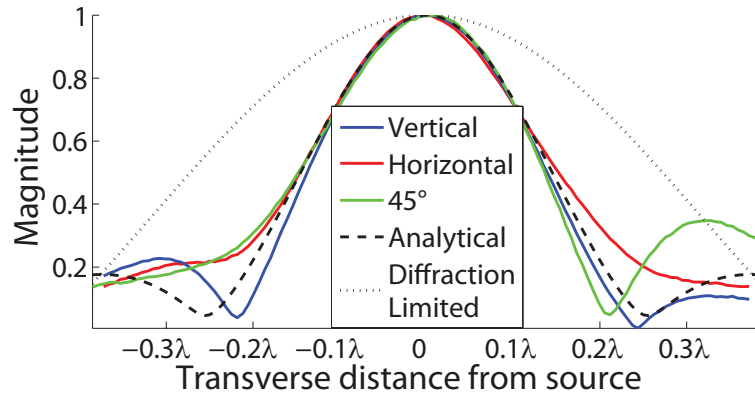
Figure 4.30: Solid lines show the normalized magnetic field magnitudes measured at the focal plane. The dashed black line represents the theoretical curve based on the integration of the Green's functions for an appropriately oriented magnetic dipole. The dotted black line indicates the diffraction-limited pattern.

127

4.5.1 The Optical Transfer Function of the Lens
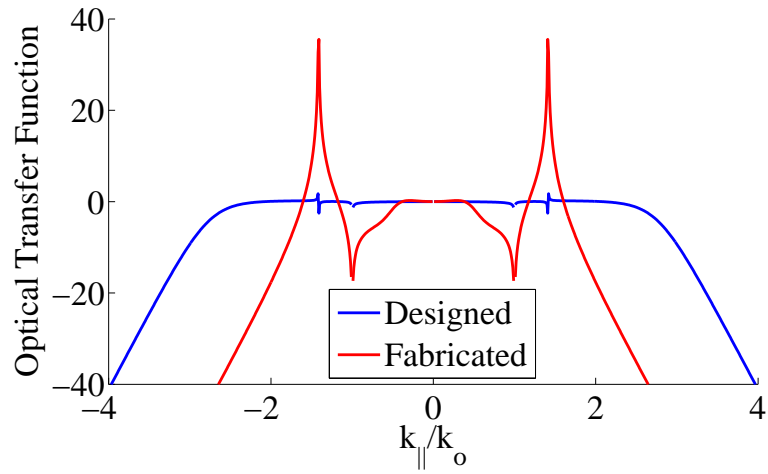
Figure 4.31: Optical transfer function of the NRI lens for the electric dipole source. The blue line represents the original design; the red line more accurately reflects the dimensions of the fabricated structure.
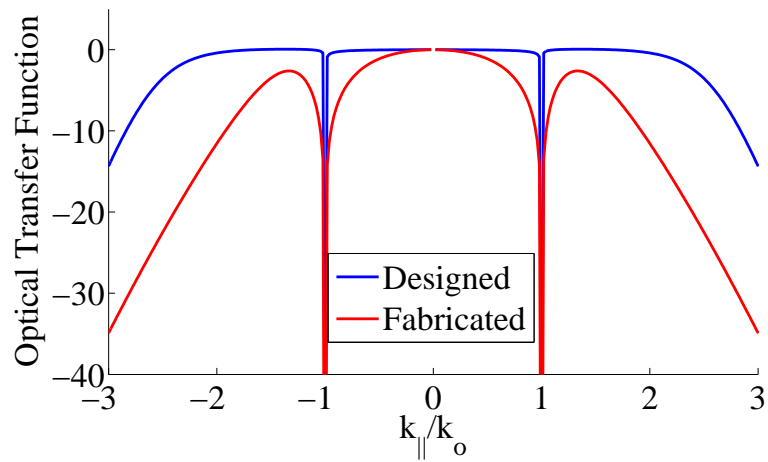
Figure 4.32: Optical transfer function of the NRI lens for the magnetic dipole source. The blue line represents the original design; the red line more accurately reflects the dimensions of the fabricated structure.

The claim of super resolution is further supported by the optical transfer function (OTF) of the NRI lens. To find the OTF, the spectrum at the focal plane is divided by the original spectrum of the source. The analytical OTFs are calculated for both the electric and magnetic dipole sources based on the simulated material parameters and are plotted in Figs. 4.31 and 4.32, respectively. Each graph shows the original

design in blue and as well as the fabricated design in red. The original design represents the optimal transfer function that could be realized using commercially-available components and reliable fabrication procedures.

The resolution enhancement is defined as the highest transverse wavenumber (k_ρ) recovered at the image, normalized by k_0. The transverse wavenumber is said to be recovered if its amplitude at the image is greater than half of its amplitude at the source. According to the material parameters obtained in simulation, the resolution enhancement of the fabricated NRI lens is 1.72 for the electric dipole source and 1.69 for the magnetic dipole source. However, as can be seen from Figs. 4.31 and 4.32, the resolution enhancement could optimally be much larger if the SCRs had been fabricated more accurately. The material parameters of the original design yield a resolution enhancement of 2.86 for the electric dipole source and 2.66 for the magnetic dipole.

Given that the OTF is calculated by dividing the spectrum at the focal plane by the one at the source, one might expect the OTF to be source independent. However, this is not the case. As shown in Eq. (4.34), the electric dipole excites both TE and TM waves. Eq. (4.38) shows that the magnetic dipole excites only TE waves. TE and TM waves have different reflection and transmission coefficients, the effects of which are observed at the focal plane, but not at the source. As a result, the reflection and transmission coefficients cause the differences observed between Figs. 4.31 and 4.32 as well as the variation in resolution enhancements for the different sources.

CHAPTER V

Conclusion

5.1   Summary of Achievements

The aim of this thesis has been to address the three most significant limitations of negative-refractive-index (NRI) metamaterials: narrow bandwidth, high loss and polarization dependence. By alleviating these three restrictions, the remarkable electrical properties of NRI media can be employed in practical applications.

This thesis places particular emphasis on improving the bandwidth of NRI metamaterials. To that end, a topology for the first broadband NRI medium was introduced. The design allowed for fractional NRI bandwidths up to 68%— nearly seven times the bandwidth of typical split-ring resonator (SRR)/wire NRI media. Using this topology, two NRI lenses were designed, fabricated and measured: one operating at 2.45GHz and another at 10.435GHz. The NRI bandwidths of these lenses were both over 40%, which were the widest NRI bandwidths exhibited by any structure fabricated to date.

Both of the NRI lenses were capable of focusing beyond the diffraction limit. This ability suggested that both lenses were low-loss, and this was directly verified through both simulations and transmission measurements of the free-space lens. The free-space lens, operating over X-band, exhibited the lowest loss (0.17dB/cell) and the highest figure of merit ($n'/n'' = 31.4$) of any NRI metamaterial measured to date.

To aid in the design of these broadband metamaterials, analytical circuit models were derived to accurately describe their behavior. The circuit models were based on multiconductor transmission-line (MTL) theory. They predicted the dispersion diagram of the infinite NRI medium and the S-parameters of finite slabs. By homogenizing the circuit model of the unit cell into a T-network, closed-form expressions were derived for the dispersion equation in one and two dimensions, the Bloch impedance along the principle axes, the permeability and permittivity, the low-frequency permeability resonance, and the magnetic and electric plasma frequencies.

The polarization dependence of NRI metamaterials was addressed through the development of a new magnetic element, the split-cube resonator, which exhibited full octahedral symmetry. This design incorporated the principles from the broadband NRI medium to achieve a NRI bandwidth of 24% when matched to free space. Still more impressive was the negative permeability bandwidth, which reached 44%. Both the NRI and negative permeability bandwidths are substantially wider than than those achievable using SRR-based metamaterials. Using this design, the first fully isotropic, polarization-independent NRI medium was fabricated using stereolithography and electroplating. More than 400 unit cells were fabricated and incorporated into a NRI lens. The lens experimentally demonstrated super-resolved focusing for both electric and magnetic sources, independent of their polarization. Additionally, the half-power beamwidths at the focal plane were nearly identical for all polarizations, verifying the isotropy of the NRI lens.

5.2 Future Work

Research often uncovers more challenges during the process of resolving others. Consequently, there are several issues pertaining to the research presented in the previous chapters that deserve further attention.

The experimental realization of a fully isotropic NRI medium presented in Chapter

IV represented an important step for NRI metamaterials, but there are several aspects of the work which can be improved. Currently, no analytical model exists for the split-cube resonator (SCR)/wire medium. Equations should be derived that predict the performance of the metamaterial and aid in its design. Since the structure is polarization independent, its analytical model should be as well. This precludes the application of the MTL analysis employed in Chapter II because the use of image theory requires a specific field orientation. Nevertheless, three-dimensional circuit models, such as the one presented in [18], offer promising clues as to how the behavior of SCR/wire arrays could be expressed analytically.
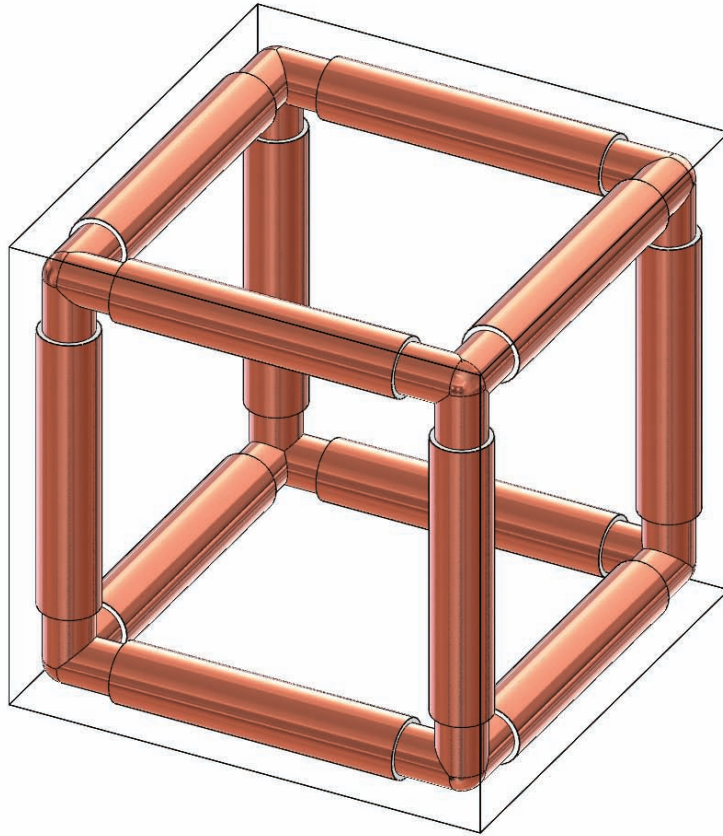
Figure 5.1: The alternative design for the SCR. The design eliminates the chip capacitors and the need for masks in the electroplating process.

Further attention should also be given to simplifying the fabrication process of polarization-independent metamaterials. The SCRs could be produced in large quan-

tities, but the overall process required a significant amount of manual labor. Most of the labor was due to the 12 chip capacitors required for each unit cell. Not only did the capacitors make the fabrication more complex, they also increased the cost of the structure significantly and limited the frequency of operation. Fig. 5.1 shows a design that completely eliminates the chip capacitors in favor of sheath capacitors. The design consists of three parts which are shown in Fig. 5.2. Part A is the sheath portion of the new SCR. Part B is one corner of the cubic frame. Part C is a spacer. To assemble the complete SCR, the sheaths (Part A) should be slid onto the legs of a cubic frame corner (Part B). Next, a spacer (Part C) should then be slid into each sheath before inserting the leg of the adjacent corner. In this way, the spacers separate the corners of the cubic frame, while the sheaths provide the capacitance to tune the resonance of the SCR. The design in Fig. 5.1 also has the advantage of not requiring any masks during the electroplating process. The corners of the cubic frame should be completely plated, while only the exteriors of sheaths should be plated and the spacers should remain unmetalized. Eliminating the need for masks and chip capacitors greatly simplifies the fabrication process of the SCR, allowing for the construction of larger slabs of the metamaterial and higher frequencies of operation.

Part A   Part B   Part C
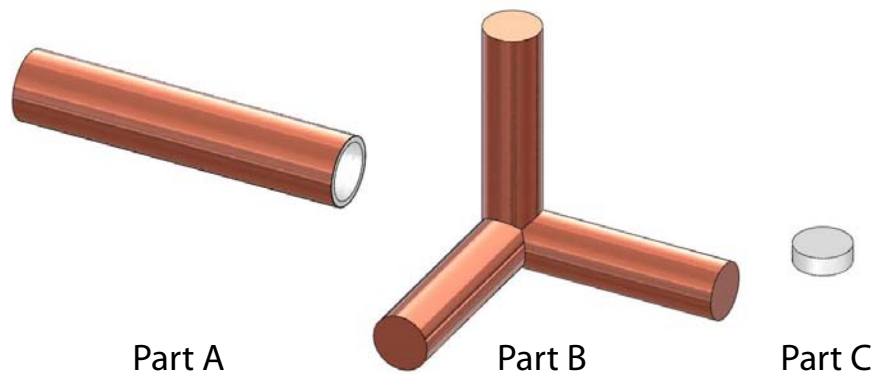
Figure 5.2: The three unique pieces required to fabricate the new design of the polarization independent NRI metamaterial shown in Fig. 5.1. Part A is the sheath used to capacitively load the SCR. Part B is one corner of the cubic frame. Part C is a dielectric spacer.

The work described in this thesis focused on making NRI metamaterials more practical by addressing their most significant challenges. To demonstrate that these media can now be considered viable solutions to practical electromagnetic problems, they should be used to improve current microwave devices. To this end, a leaky-wave antenna could be developed that radiates at broadside. To achieve broadside radiation, conventional leaky-wave antennas rely on resonant spacing of periodic elements, and partially-reflective-surface antennas use dielectric layers of resonant thickness [68]. Reliance on resonant spacing makes these antennas particularly susceptible to beam squint. To alleviate this issue, a metamaterial substrate designed to exhibit an effective refractive index of zero could be used to feed the radiating elements of the leaky-wave antenna, as shown in Fig. 5.3. By designing the metamaterial to have coincident electric and magnetic plasma frequencies, the substrate would exhibit a non-zero group velocity and close the stopband that is typically present between the NRI frequencies and the positive-refractive-index frequencies. Such a substrate would allow waves to propagate through the medium with constant phase, exciting all of the antenna elements in phase, producing a directive beam at broadside. Since the radiating elements would be spaced electrically close to each other, the medium could operate in the continuous limit. This would render the antenna less susceptible to beam squint, as was demonstrated in [69].

Modeling the leaky-wave antenna using MTL analysis is also an important task for future work. As can be seen in Fig. 5.3, the unit cell of the zero-index metamaterial substrate is similar to the broadband NRI medium discussed in Chapter II, making the design well suited for MTL modeling. The two differences that would need to be accounted for are the asymmetry of the unit cell and the effect of the radiating slots. In order to accurately model the asymmetrical unit cell, an arbitrary two-dimensional analysis is needed. The effect of the slot antennas can be modeled with appropriate radiation resistances, along with parallel capacitive and inductive elements to adjust

134
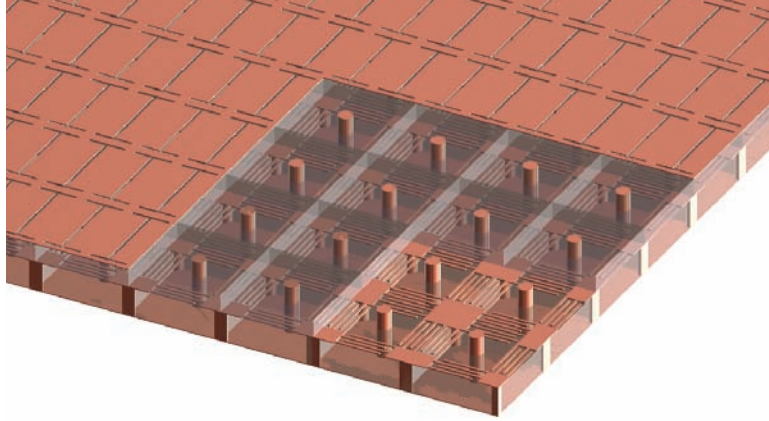
Figure 5.3: A look inside the parallel plate waveguide filled with zero-index metamaterial.

for current-flow perturbation on the top conductor.

Finally, improving the bandwidth of NRI metamaterials will always be a challenge since they are necessarily dispersive. The techniques in this thesis focus on improving the overall NRI bandwidth of the medium, but the most important metric is over what frequency range these metamaterials can exhibit specific material parameters with reasonable tolerances. Filter theory provides an excellent example for engineers to begin this pursuit. The most basic filters are periodic structures that consist of repeating component combinations. However, better performance can be achieved by varying the components according to established parameters as are given by the Chebyshev, Butterworth, elliptical or linear-phase coefficients [70]. By applying similar aperiodic analysis to NRI metamaterials, the overall structure may achieve levels of performance not possible using strictly periodic techniques. Further, by developing NRI-specific mathematical prototypes, the component values for these metamaterials could be known immediately from tables or simple formulae, reducing the amount of time spent simulating such numerically intensive structures. With these techniques, the performance of NRI metamaterials can be pushed to their true physical limits.

135

5.3   List of Publications

The work of this thesis has been published in the following peer-reviewed journals and conference proceedings.

Journal Papers

S. M. Rudolph, A. Grbic, "A broadband three-dimensionally isotropic negative-refractive-index medium," submitted to *IEEE Transactions on Antennas and Propagation* on April 20th, 2011.

S. M. Rudolph, C. Pfeiffer, A. Grbic, "Design and free-space measurements of broadband, low-loss negative-permeability and negative-index media," accepted to *IEEE Transactions on Antennas and Propagation*, scheduled to appear in vol. 59, no. 8, August 2011.

S. M. Rudolph, A. Grbic, "The design of broadband, volumetric NRI media using multiconductor transmission-line analysis," *IEEE Transactions on Antennas and Propagation*, vol. 58, no. 4, pp. 1144 – 1154, April 2010.

S. M. Rudolph, A. Grbic, "Super-resolution focusing using volumetric, broadband NRI media," *IEEE Transactions on Antennas and Propagation*, vol. 56, no. 9, pp. 2963 – 2969, September 2008.

S. M. Rudolph, A. Grbic, "Volumetric negative refractive index medium exhibiting broadband negative permeability," *Journal of Applied Physics*, vol. 102, 013904, July 2007.

Conference Proceedings

A. Grbic, G. Gok, S. M. Rudolph, "Advances in planar and volumetric metamaterials," *International Conference on Applied Electromagnetics and Communications*, 4 pages, Dubrovnik, Coatia, September 20 – 23 2010.

S. M. Rudolph, A. Grbic, "A broadband three-dimensional isotropic NRI medium," *IEEE International Symposium on Antennas and Propagation*, 4 pages, Toronto, CA, July 11–17 2010.

S. M. Rudolph, A. Grbic, "Broadband, low-loss negative-permeability and negative-index media for free-space applications," *IEEE MTT-S International Microwave Symposium*, 4 pages, Boston, MA, June 6-12 2009.

S. M. Rudolph, A. Grbic, "Design equations for broadband, volumetric NRI media," *Second International Conference on Advanced Electromagnetic Materials in Microwaves and Optics (Metamaterials '08)*, 3 pages, Pamplona, Spain, September 21–26 2008.

S. M. Rudolph, A. Grbic, "Modeling of volumetric negative-refractive-index media using multiconductor transmission-line analysis," *Applied Computational Electromagnetics Society (ACES) Conference*, 4 pages, Niagara Falls, Canada, March 30–April 4 2008.

S. M. Rudolph, A. Grbic, "A printed-circuit implementation of a broadband volumetric negative-refractive-index medium," *IEEE International Symposium on Antennas and Propagation*, Honolulu HI, pp. 2542–2545, June 9–15 2007.

Conference Summaries

S. M. Rudolph, A. Grbic, "Measurements of an isotropic, broadband negative-refractive-index medium," *USNC/URSI National Radio Science Meeting*, Spokane, WA, July 3–8, 2011.

S. M. Rudolph, C. Pfeiffer, A. Grbic, "Broadband negative-refractive-index media: analytical modeling and free space measurements," *XXIX General Assembly of the International Union of Radio Science (URSI)*, Chicago, IL, Aug 7–16, 2008.

APPENDICES

APPENDIX A

Dispersion Diagrams

Dispersion Diagrams for One-Dimensional Propagation

The dispersion diagram (or Brillouin diagram) [71] is a common method of showing how phase changes with frequency in a given medium. Fig. A.1(a) shows a dispersion diagram for propagation along the $\hat{x}$-axis of a region of free-space 1cm in length. The independent variable (plotted on the horizontal axis) is the phase delay across this region, kd, where k is the wavenumber in the medium and d is the length of the region (in this case, $d = 1$cm). Since the length of the region is fixed, a change in phase delay corresponds to a change in wavenumber within the medium. The dependent variable is the frequency (plotted on the vertical axis), which is related to the wavenumber by the following equation:

$$f = \frac{v_p k}{2\pi} = \frac{ck}{2\pi n_{eff}},\tag{A.1}$$

where v_p is the phase velocity, c is the speed of light in a vacuum and n_{eff} is the effective index of refraction. In the example of propagation through free space, the index of refraction and phase velocity of the medium are constant with frequency ($n_{eff} = 1$ and $v_p = c$), resulting in the linear dispersion curve shown in Fig. A.1(a).
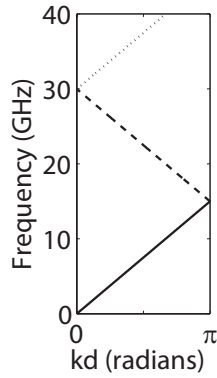
(a) Typical dispersion diagram for propagation in one dimension.
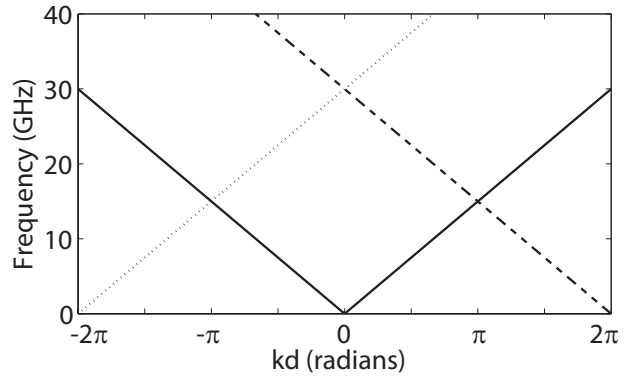
(b) Expanded dispersion diagram showing the periodicity of the phase delay.

Figure A.1: Two dispersion diagrams for propagation through a 1cm region of free space.

When kd reaches a value of π, the dispersion curve in Fig. A.1(a) changes direction and becomes a backward-wave mode, decreasing in phase as the frequency increases. The curve switches back to a forward wave when the backward-wave mode reaches a phase delay of zero. The alternating directionality of the modes is a consequence of the periodic nature of the phase delay. Fig. A.1(b) shows the same dispersion curve over a wider range of phase delays. Consider the two solid curves that start at the origin. The curve on the right represents propagation in the $\hat{x}$ direction, and the curve on the left represents propagation in the $-\hat{x}$ direction. Adding 2π to the phase delay of the backward-wave curve yields the dashed-line. Subtracting 2π from the phase delay of the forward-wave curve yields the dotted line. In the region of the dispersion diagram where $0 \leq kd \leq \pi$, these lines correspond exactly to the high-frequency modes shown in Fig. A.1(a), illustrating how the high-frequency modes arise from the periodicity of the phase delay.

It should be noted that only for completely homogeneous media are transitions between forward- and backward-wave modes continuous. Periodic media exhibit a Bragg resonance when the phase delay across their unit cells reaches π, which causes a stopband to form before the next highest mode begins [1].

140

Multi-Dimensional Dispersion Diagrams

For isotropic continuous media, such as the free-space region in the previous example, knowledge of the propagation characteristics along a single axis is sufficient to completely describe the dispersion of the medium in any direction. Since the medium appears the same regardless of orientation, the choice of a specific coordinate system is arbitrary. However, for periodic media (particularly those with cubic or rectangular prism lattices like the structures discussed in this thesis), spatial dispersion can cause significant differences between on- and off-axis propagation. To view how propagation within these periodic structures changes with direction, multi-dimensional dispersion diagrams can be calculated.

Two-dimensional dispersion diagrams consider propagation in the $\hat{x}$ and $\hat{y}$ directions. An example of a two-dimensional dispersion diagram is Fig. 2.20 (included for convenience in this appendix as Fig. A.2). The phase delay remains the independent variable in these graphs, however, the horizontal axis is no longer a line of linearly ascending values. Instead, the horizontal axis (and the dispersion diagram as a whole) is split into three regions, each separated by the critical points Γ, X and M. Each of these points corresponds to a specific phase delay enforced on the periodic boundaries. Γ corresponds to the minimum phase delay: $k_x d = 0$, $k_y d = 0$, while the M point refers to the maximum phase delay: $k_x d = \pi$, $k_y d = \pi$. X can refer to either $k_x d = \pi$, $k_y d = 0$ or $k_x d = 0$, $k_y d = \pi$. All structures discussed in this thesis are symmetric in with respect to their $\hat{x}$- and $\hat{y}$-axes, so it is unnecessary to specify which phase delay configuration is used. However, for asymmetric structures, this difference would be significant and require the X point to be clearly defined.

The first region of the two-dimensional dispersion diagram (Γ to X) represents propagation along the $\hat{x}$-axis (assuming X corresponds to $k_x d = \pi$, $k_y d = 0$). Therefore, it is the same as the dispersion diagram for one-dimensional propagation. The second region (X to M) plots the change in frequency as the direction of propagation

141
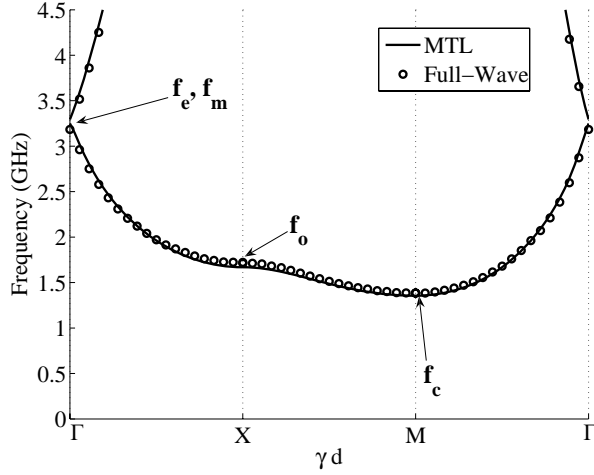
Figure A.2: Two-dimensional dispersion diagram for the broadband NRI medium discussed in Chapter II.

changes from on-axis at the X point to off-axis at the M point (where the propagation vector is 45° away from both the $\hat{x}$- and $\hat{y}$-axes). The third region (M to Γ) represents a one-dimensional dispersion diagram for off-axis propagation. The propagation vector never changes directions in this region because the phase delays are varied such that $k_x d = k_y d$. It should be noted that the one-dimensional dispersion diagram from M to Γ is backward compared to the standard one-dimensional diagram presented in the previous section.

Three-dimensional dispersion diagrams are similar to two-dimensional diagrams in that they share the critical points of Γ, X and M. These points are defined exactly as they are in the two-dimensional case, with the condition $k_z d = 0$ now added explicitly. The primary difference between the two- and three-dimensional dispersion diagrams is the R point: defined as $k_x d = \pi$, $k_y d = \pi$, $k_z d = \pi$. The addition of a third dimension also adds a fourth region to the dispersion diagram, which can be seen in Fig. 4.3 (reprinted in this appendix as Fig. A.3). The first two regions (Γ to X and X to M) are defined in exactly the same way as they are in the two-dimensional dispersion diagram. The third region (M to R) plots the change in frequency as the

direction of propagation changes from 45° off of the $\hat{x}$- and $\hat{y}$-axes in the $\hat{x} - \hat{y}$ plane at the M point to 45° off of the $\hat{x}$-, $\hat{y}$- and $\hat{z}$-axes at the R point. The fourth region (R to Γ)is a one-dimensional dispersion diagram for off-axis propagation, where the phase delays are varied such that $k_x d = k_y d = k_z d$. Similar to the third region of the two-dimensional dispersion diagram, the dispersion curve is backward compared to the standard one-dimensional diagram.
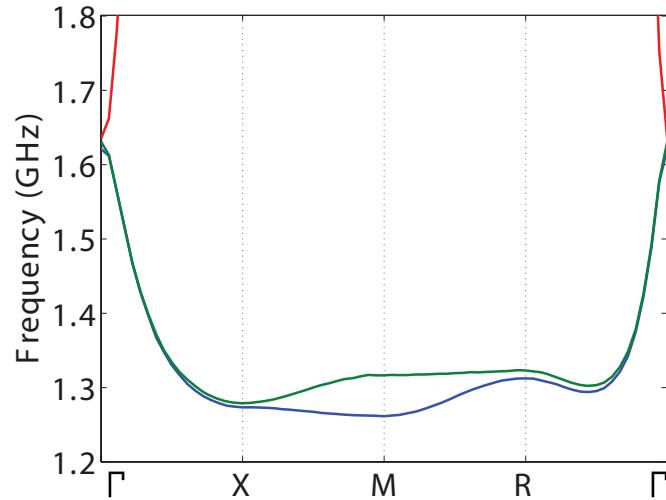
Figure A.3: Three-dimensional dispersion diagram for the isotropic NRI medium presented in Chapter IV.

APPENDIX B

The Application of the Propagation Matrix in MTL Analysis

The propagation in a multiconductor transmission-line (MTL) circuit is described by Eq. (2.11):

$$\mathbf{V}(x) = e^{-\sqrt{\mathbf{ZY}}x}\mathbf{V}^+ + e^{\sqrt{\mathbf{ZY}}x}\mathbf{V}^-. \tag{B.1}$$

The similar forms of this equation and its single-conductor counterpart (Eq. (2.3)) help define the propagation constant matrix as $\mathbf{\Gamma} = \sqrt{\mathbf{ZY}}$. However, it is not intuitive how the different elements of the propagation constant matrix relate the voltages traveling along individual transmission lines to one another.

The reason for this is that $\mathbf{\Gamma}$ does not actually relate the conductor voltages to each other, rather, this is done by the exponential propagation matrix $e^{-\mathbf{\Gamma}x}$. It is critical to observe that

$$e^{-\mathbf{\Gamma}x} \neq \begin{bmatrix} e^{-\Gamma_{11}x} & \cdots & e^{-\Gamma_{1n}x} \\ \vdots & \ddots & \vdots \\ e^{-\Gamma_{n1}x} & \cdots & e^{-\Gamma_{nn}x} \end{bmatrix}. \tag{B.2}$$

To actually find the matrix elements of $e^{-\mathbf{\Gamma}x}$, the propagation constant matrix $\mathbf{\Gamma}$ must

144

be diagonalized, such that

$$\mathbf{A}^{-1}\mathbf{\Gamma}\mathbf{A} = \begin{bmatrix} \gamma_1 & 0 & \cdots & 0 \\ 0 & \gamma_2 & \ddots & \vdots \\ \vdots & \ddots & \ddots & 0 \\ 0 & \cdots & 0 & \gamma_n \end{bmatrix}. \tag{B.3}$$

In Eq. (B.3), γ_i is a modal propagation constant. The modal propagation constants do not describe the propagation on any specific conductor, rather they describe the propagation of one mode which travels through the MTL circuit as a whole. For the MTL structure discussed in section 2.4.1, these modal propagation constants are referred to as γ_c and γ_π. $\mathbf{A}$ is the diagonalization matrix and consists of column vectors, $\vec{a_i}$, which are the eigenvectors associated with the modal propagation constants, γ_i. Therefore, $\mathbf{A}$ is defined as

$$\mathbf{A} = \begin{bmatrix} | & \cdots & | \\ \vec{a_1} & \cdots & \vec{a_n} \\ | & \cdots & | \end{bmatrix}. \tag{B.4}$$

Once diagonalized, the modal propagation constants can be used to form a diagonal exponential propagation matrix:

$$e^{-\boldsymbol{\gamma}x} = \begin{bmatrix} e^{-\gamma_1 x} & 0 & \cdots & 0 \\ 0 & e^{-\gamma_2 x} & \ddots & \vdots \\ \vdots & \ddots & \ddots & 0 \\ 0 & \cdots & 0 & e^{-\gamma_n x} \end{bmatrix}. \tag{B.5}$$

The diagonalization matrix $\mathbf{A}$ can then be used to transform the diagonal exponential propagation matrix to the natural exponential propagation matrix as follows:

$$e^{-\boldsymbol{\Gamma}x} = \mathbf{A}e^{-\boldsymbol{\gamma}x}\mathbf{A}^{-1}. \tag{B.6}$$

This same procedure must followed to perform the hyperbolic cosine and hyperbolic sine operations used in Eq. (2.15). These operations can be written in the same form as Eq. (B.6):

$$\cosh\left(\mathbf{\Gamma}l\right) = \mathbf{A}\cosh\left(\boldsymbol{\gamma}l\right)\mathbf{A}^{-1} \tag{B.7}$$

$$\sinh\left(\mathbf{\Gamma}l\right) = \mathbf{A}\sinh\left(\boldsymbol{\gamma}l\right)\mathbf{A}^{-1}. \tag{B.8}$$

BIBLIOGRAPHY

BIBLIOGRAPHY

[1] W. H. Bragg and W. L. Bragg, "The Reflection of X-rays by Crystals," *Proceedings of the Royal Society of London*, vol. 88, no. 605, pp. 428–438, 1913.

[2] D. A. G. Bruggeman, "Berechnung verschneidener physikalischer Konstanten von heterogenen Substanzen," *Annalen der Physik*, vol. 5, no. 24, pp. 636–664, 1935.

[3] W. E. Kock, "Metal-lens antennas," *Procedings of the Institue of Radio Engineers*, vol. 34, pp. 828–837, November 1946.

[4] ——, "Metallic delay lenses," *Bell System Technical Journal*, vol. 27, pp. 58–83, January 1948.

[5] ——, "Path-length microwave lenses," *Procedings of the Institue of Radio Engineers*, vol. 37, pp. 852–855, August 1949.

[6] J. Brown, "Artificial dielectrics having refractive indices less than unity," *Proceedings of the IEE*, vol. 100, no. 5, pp. 51–62, October 1953.

[7] W. Rotman, "Plasma Simulation by Artificial Dielectrics and Parallel-Plate Media," *IRE Transactions on Antennas and Propagation*, pp. 82–95, January 1962.

[8] J. B. Pendry, A. J. Holden, D. J. Robbins, and W. J. Stewart, "Magnetism from Conductors and Enhanced Nonlinear Phenomena," *IEEE Transactions on Microwave Theory and Techniques*, vol. 47, pp. 2075–2084, November 1999.

[9] A. Pimenov, A. Loidl, P. Przyslupski, and B. Dabrowski3, "Negative refraction in ferromagnet-superconductor superlattices," *Physical Review Letters*, vol. 95, p. 247009, December 2005.

[10] T. Kasagi, T. Tsutaoka, and K. Hatakeyama, "Negative permeability spectra in permalloy granular composite materials," *Applied Physics Letters*, vol. 88, p. 172502, December 2005.

[11] V.G. Veselago, "The Electrodynamics of Substances with Simultaneously Negative Values of ϵ and μ," *Sov. Phys. Usp.*, vol. 10, pp. 509–514, Jan-Feb 1968.

[12] J.B. Pendry, "Negative Refraction Makes a Perfect Lens," *Physical Review Letters*, vol. 85, pp. 3966–3969, October 2000.

[13] D.R. Smith, W.J. Padilla, D.C. Vier, S.C. Nemat-Nasser, and S. Schultz, "Composite Medium With Simultaneously Negative Permeability and Permittivity," *Physical Review Letters*, vol. 84, pp. 4184–4187, May 2000.

[14] J.B. Pendry, D. Schurig, and D. R. Smith, "Controlling Electromagnetic Fields," *Science*, vol. 312, pp. 1780–1782, June 2006.

[15] R.A. Shelby, D.R. Smith, and S. Schultz, "Experimental Verification of a Negative Index of Refraction," *Science*, vol. 292, pp. 77–79, April 2001.

[16] A. F. Starr, P. M. Rye, D. R. Smith, and S. Nemat-Nasser, "Fabrication and Characterization of a Negative-Refractive-Index Composite Metamaterial," *Physical Review B*, vol. 70, p. 113102, September 2004.

[17] M. J. Freire, R. Marques, and L. Jelinek, "Experimental demonstration of a $\mu = $ -1 metamaterial lens for magnetic resonance imaging," *Applied Physics Letters*, vol. 93, no. 23, p. 231108, December 2008.

[18] A. Grbic and G.V. Eleftheriades, "An isotropic three-dimensional negative-refractive-index transmission-line metamaterial," *Journal of Applied Physics*, vol. 98, p. 043106, August 2005.

[19] A.K. Iyer and G.V. Eleftheriades, "A three-dimensional isotropic transmission-line metamaterial topology for free-space excitation," *Applied Physics Letters*, vol. 92, p. 261106, July 2008.

[20] ——, "Negative Refractive Index Metamaterials Supporting 2-D Waves," in *IEEE International Microwave Symposium*, vol. 2, Seattle, WA, June 2-7 2002, pp. 1067–1070.

[21] G.V. Eleftheriades, A.K. Iyer, and P.C. Kremer, "Planar Negative Refractive Index Media Using Periodically L-C Loaded Transmission Lines," *IEEE Transactions on Microwave Theory and Techniques*, vol. 50, no. 12, pp. 2702–2712, December 2002.

[22] C. Caloz and T. Itoh, "Application of the transmission line theory of left-handed (LH) materials to the realization of a microstrip "LH line"," in *IEEE Antennas and Propagation Society International Symposium*, vol. 2, San Antonio, TX, June 16-21 2002, pp. 412–415.

[23] A. A. Oliner, "A Periodic-Structure Negative-Refractive-Index Medium Without Resonant Elements," in *USNC/URSI Radio Science Meeting*, San Antonio, TX, June 16-21 2002.

[24] A. Grbic and G.V. Eleftheriades, "Experimental Verification of Backward-Wave Radiation From a Negative Refractive Index Metamaterial," *Journal of Applied Physics*, vol. 92, pp. 5930–5935, November 2002.

[25] E. L. Gintzton, W. R. Hewlett, J. H. Jasberg, and J. D. Noe, "Distributed Amplification," *Procdings of the I.R.E.*, vol. 36, no. 8, pp. 956–969, August 1948.

[26] C. H. Walter, *Traveling Wave Antennas.* New York, NY: McGraw-Hill, Inc., 1965.

[27] R. R. A. Syms, E. Shamonina, V. Kalinin, and L. Solymar, "A Theory of Metamaterials Based on Periodically Loaded Transmission Lines: Interaction between Magnetoinductive and Electromagnetic Waves," *Journal of Applied Physics*, vol. 97, p. 064909, March 2005.

[28] A. Grbic, "A 2-D Composite Medium Exhibiting Broadband Negative Permittivity and Permeability," in *IEEE AP-S International Symposium*, Albuquerque, NM, July 9-14 2006, pp. 4133–4136.

[29] S. M. Rudolph and A. Grbic, "A Volumetric Negative-Refractive-Index Medium Exhibiting Broadband Negative Permeability," *Journal of Applied Physics*, vol. 102, p. 013904, July 2007.

[30] G. V. Eleftheriades and K. G. Balmain, *Negative-Refraction Metamaterials.* New York, NY: John Wiley & Sons, Inc., 2005.

[31] C. Caloz and T. Itoh, *Electromagnetic Metamaterials.* New York, NY: John Wiley & Sons, Inc., 2005.

[32] J. B. Pendry, A. J. Holden, D. J. Robbins, and W. J. Stewart, "Low frequency plasmons in thin-wire structures," *Journal of Physics: Condensed Matter*, vol. 10, no. 22, pp. 4785–4809, March 1998.

[33] F. Elek and G. V. Eleftheriades, "Dispersion Analysis of the Shielded Sievenpiper Structure Using Multiconductor Transmission-Line Theory," *IEEE Microwave and Wireless Components Letters*, vol. 14, no. 9, pp. 434–436, September 2004.

[34] ——, "Simple Analytical Dispersion Equations for the Shielded Sievenpiper Structure," in *IEEE MTT-S International Microwave Symposium*, San Fransisco, CA, June 11-16 2006, pp. 1651–1654.

[35] J. A. Brandão Faria, *Multiconductor Transmission-Line Structures: Modal Analysis Techniques.* New York, NY: John Wiley & Sons, Inc., 1993.

[36] Clayton R. Paul, *Analysis of Multiconductor Transmission Lines.* 605 Third Avenue, New York, NY 10158: John Wiley & Sons, Inc., 1994.

[37] K. C. Gupta, Ramesh Garg, and I. J. Bahl, *Microstrip Lines and Slotlines.* Dedham, MA: Artech House Inc., 1979.

[38] S. M. Rudolph and A. Grbic, "The Design of Broadband, Volumetric NRI Media Using Multiconductor Transmission-Line Analysis," *IEEE Transactions on Antennas and Propagation*, vol. 58, no. 4, April 2010.

[39] C. R. Brewitt-Taylor and P. B. Johns, "On the Construction and Numerical Solution of Transmission-Line and Lumped Network Models of Maxwell's Equations," *International Journal for Numerical Methods in Engineering*, vol. 15, no. 1, pp. 13–30, 1980.

[40] D.R. Smith, D. Schurig, R. Rosenbluth, S. Schultz, S.A. Ramakrishna, and J.B. Pendry, "Limitations on Subdiffraction Imaging with a Negative Refractive Index Slab," *Applied Physics Letters*, vol. 82, pp. 1506–1508, March 2003.

[41] A. Grbic and G. V. Eleftheriades, "Practical Limitations of Subwavelength Resolution Using Negative-Refractive-Index Transmission-Line Lenses," *IEEE Transactions on Antennas and Propagation*, vol. 53, no. 10, pp. 3201–3209, October 2005.

[42] R. Merlin, "Analytical Solution of the Almost-Perfect-Lens Problem," *Applied Physics Letters*, vol. 84, no. 8, pp. 1290–1292, February 2003.

[43] V. Podolskiy and E. Narimanov, "Near-sighted superlens," *Optics Letters*, vol. 30, no. 1, pp. 75–77, January 2005.

[44] S. M. Rudolph and A. Grbic, "Super-Resolution Focusing using Volumetric, Broadband NRI Media," *IEEE Transactions on Antennas and Propagation*, vol. 56, no. 9, pp. 2963–2969, September 2008.

[45] A. M. Nicolson and G. F. Ross, "Measurement of the intrinsic properties of materials by time-domain techniques," *IEEE Transactions on Instrumentation and Measurement*, vol. 19, no. 4, pp. 377–382, November 1970.

[46] J. Baker-Jarvis, M. D. Janezic, J. H. Grosvenor, and R. G. Geyer, "Transmission/Reflection and Short-Circuit Line Methods for Measuring Permittivity and Permeability," *National Institute of Standards and Technology Technical Note*, vol. Note 1355-R, pp. 6–19, Dec 1993.

[47] A. Alu, "Restoring the physical meaning of metamaterial constitutive parameters," *Physical Review B*, vol. 83, p. 081102, February 2011.

[48] C. M. Soukoulis, S. Linden, and M. Wegener, "Negative Refractive Index at Optical Wavelengths," *Science*, vol. 315, pp. 47–49, January 2007.

[49] V. M. Shalaev, "Optical Negative-Index Metamaterial," *Nature Photonics*, vol. 1, pp. 41–48, January 2007.

[50] A. Grbic and G.V. Eleftheriades, "Overcoming the Diffraction Limit with a Planar Left-Handed Transmission-Line Lens," *Physical Review Letters*, vol. 92, no. 11, p. 117403, March 2004.

[51] B. J. Justice, J.J. Mock, L. Guo, A. Degiron, D. Schurig, and D.R. Smith, "Spatial Mapping of the Internal and External Electromagnetic Fields of Negative Index Metamaterials," *Optics Epress*, vol. 14, no. 19, pp. 8694–8705, September 2006.

[52] J. Shin, J Shen, and S. Fan, "Three-Dimensional Metamaterials with an Ultrahigh Effective Refractive Index over a Broad Bandwidth," *Physical Review Letters*, vol. 102, p. 093903, March 2009.

[53] P. F. Goldsmith, "Quasi-Optical Techniques," *Proc. of the IEEE*, vol. 80, no. 11, pp. 1729–1747, November 1992.

[54] F. Biraud and G. Daigne, "Achromatic doublets for Gaussian beams," *IEEE Transactions on Antennas and Propagation*, vol. 39, no. 4, April.

[55] P. F. Goldsmith, *Quasioptical Systems: Gaussian Beam Quasioptical Propagation and Applications*. New York, NY: John Wiley & Sons, Inc., 1997.

[56] K. Li, S. J. McLean, R. B. Greegor, C. G. Parazzoli, and M. H. Tanielian, "Free-space focused-beam characterization of left-handed materials," *Applied Physics Letters*, vol. 82, no. 15, pp. 2535–2537, April 2003.

[57] K. Aydin and E. Ozbay, "Left-handed metamaterial based superlens for sub-wavelength imaging of electromagnetic waves," *Applied Physics A*, vol. 87, pp. 137–141, January 2007.

[58] A.K. Iyer and G.V. Eleftheriades, "A Multilayer Negative-Refractive-Index Transmission-Line (NRI-TL) Metamaterial Free-Space Lens at X-band," *IEEE Transactions on Antennas and Propagation*, vol. 55, no. 10, pp. 2746–2753, October 2007.

[59] ——, "Mechanisms of Subdiffraction Free-Space Imaging Using a Transmission-Line Metamaterial Superlens: An Experimental Verification," *Applied Physics Letters*, vol. 92, no. 13, p. 131105, March 2008.

[60] S. M. Rudolph and A. Grbic, "Broadband, Low-Loss Negative-Permeability and Negative-Index Media for Free-Space Applications," in *IEEE International Microwave Symposium*, Boston, MA, June 9-11 2009.

[61] N. Fang, H. Lee, C. Sun, and X. Zhang, "Sub-Diffraction Limited Optical Imaging with a Silver Superlens," *Science*, vol. 308, pp. 534–537, April 2005.

[62] I. Vendik, O. Vendik, and M. Odit, "Isotropic artificial media with simultaneously negative permittivity and permeability," *Microwave and Optical Technology Letters*, vol. 18, no. 12, pp. 2553–2556, December 2006.

[63] E. Lheurette, G. Houzet, J. Carbonell, F. Zhang, O. Vanbesien, and D. Lippens, "Omega-Type Balanced Composite Negative Refractive Index Materials," *IEEE Transactions on Antennas and Propagation*, vol. 56, no. 11, pp. 3462–3469, November 2008.

[64] S. M. Rudolph and A. Grbic, "A Broadband Three-Dimensional Isotropic NRI Medium," Toronto, ON, CA, July 11-17 2010.

[65] H. Burzlaff and H. Zimmerman, "Point group symbols," *International Tables for Crystallography*, vol. A, pp. 818–820, 2006.

[66] J. D. Joannopoulos, S. G. Johnson, J. N. Winn, and R. D. Meade, *Photonic Crystals: Molding the Flow of Light.* Princeton, NJ: Princeton University Press, 2008.

[67] W. C. Chew, *Waves and Fields in Inhomogeneous Media.* Piscataway, NJ: IEEE Press, 1995.

[68] A. A. Oliner and D. R. Jackson, "Leaky-Wave Antennas," *Antenna Engineering Handbook, Fourth Edition*, McGraw Hill, 2007.

[69] M. A. Antoniades and G. V. Eleftheriades, "A CPS Leaky-Wave antenna with Reduced Beam Squinting Using NRI-TL Metamaterials," *IEEE Transactions on Antennas and Propagation*, vol. 56, no. 3, pp. 708–721, March 2008.

[70] D. Pozar, *Microwave Engineering*, 2nd ed. Toronto: John Wiley and Sons, 1998.

[71] L. Brillouin, *Wave Propagation in Periodic Structures.* Mineola, NY: Dover Publications, Inc., 2003.